UNIVERSITY OF CALIFORNIA
SANTA CRUZ

DYNAMICS OF WEAKLY NON-BOUSSINESQ CONVECTION, CONVECTIVE OVERSHOOTING AND MAGNETIC FIELD CONFINEMENT IN A SPHERICAL SHELL

A dissertation submitted in partial satisfaction of the
requirements for the degree of

DOCTOR OF PHILOSOPHY

in

APPLIED MATHEMATICS AND STATISTICS

by

Lydia Korre

September 2018

The Dissertation of Lydia Korre
is approved:

Professor Nicholas Brummell, Chair

Professor Pascale Garaud

Professor Dongwook Lee

Lori Kletzer
Vice Provost and Dean of Graduate Studies

Table of Contents

List of Figures

List of Tables

Abstract

Dynamics of weakly non-Boussinesq convection, convective overshooting and magnetic field confinement in a spherical shell

by

Lydia Korre

This doctoral work is motivated by the Sun and solar-type stars, which consist of an unstable convection zone (CZ) that lies on top of a stably stratified radiative zone (RZ). The dynamics occurring at the CZ-RZ interface are not well-understood, and yet they are known to play a significant role in processes such as transport of chemical species, angular momentum and magnetic fields. To shed some new light on this complicated problem, we have compartmentalized this work into three main chapters. In the first part, in order to mimic stellar-like conditions, we study convection in a weakly non-Boussinesq gaseous spherical shell in the low-Prandtl number regime assuming a constant adiabatic temperature gradient and employing fixed flux at the inner boundary. We find the remarkable emergence of a subadiabatic layer within the domain for sufficiently turbulent flows enhanced by large variations in the superadiabaticity across the shell. However, convection remains vigorous everywhere across the shell thus indicating that it is a highly non-local process. In the second part, we further extend our study to include a stable region below the convective zone and we investigate the dynamics of overshooting/penetrative convection. We observe that the overshooting of the turbulent motions into the RZ depends on three different parameters: the relative stability of the stable zone, the transition width between the two, and the intensity of the turbulence. We find that, in the parameter regime studied, these overshooting motions manage to partially alter the thermal stratification, but not

so efficiently as to create a fully mixed adiabatic region. We have built a model of these processes that could be useful for stellar evolution codes. In the third and final part, we also add a poloidal dipole magnetic field initially contained in the stable zone and study its interaction with the turbulent motions. Our numerical results are categorized into non-dynamo and dynamo cases. In the non-dynamo cases, the field diffuses outward, and its field lines open up and penetrate in the CZ. At the same time, a large fraction of its energy is removed due to the turbulent diffusion by the convective motions. In the dynamo cases, the field starts diffusing outward but its interaction with the turbulent motions leads to a small-scale essentially kinematic dynamo within the CZ and the overshoot region. In both of these cases, we find that the dipole field cannot remain confined in the RZ by the turbulent motions.

Dedicated to $B\alpha\gamma\gamma\acute{\epsilon}\lambda\eta \heartsuit$

Acknowledgments

I would like to thank my advisers Prof. Nic Brummell and Prof. Pascale Garaud for their endless support and guidance throughout my PhD! In particular, I thank Prof. Pascale for always being so excited about science and so dedicated to our work, for pushing me to learn more and for always be willing to teach me new topics and help me out in whatever I needed. I thank Prof. Nic who was the first to introduce me to the vast world of fluid dynamics and whose enthusiasm and humor got me so excited about this subject. I thank him for always being available to help, for teaching me new things and for answering even my most trivial questions about MHD and other things. Thank you both for being great teachers in applied math and fluid courses, but also for being great mentors. I especially thank you for always trying to pronounce the Greek letters the correct way, and for mostly succeeding in it! I look forward to collaborating with both of you in the future!

Next, I would like to thank Prof. Dongwook Lee for serving as a committee member for my advancement to candidacy exam and my dissertation defense, for writing letters of recommendation, and for teaching his great CFD class. Thank you for always being happy to help with a big smile! I also thank Prof. Jonathan Fortney for serving as a committee member during my advancement to candidacy exam. I particularly thank Céline Guervilly for her invaluable help with the PARODY code and for always being available to answer any questions! Thanks to Bhishek for being supportive and helpful, and for believing that I could actually successfully make it to the end.

Finally, $\epsilon\upsilon\chi\alpha\rho\iota\sigma\tau\acute{\omega}$ my father Giorgos, my mother Giorgia, my little genius brother Christos (– the real doctor of the family) and the fifth member of our family, Arya for always being there for me, encouraging me to pursue my goals

with their love and their constant thoughts, even though we were thousands of miles away. Σας *ευχαριστώ για την ανιδιοτελή σας αγάπη, που πιστεύετε πάντα σε εμένα και που πάντα στηρίζετε τις επιλογές μου*. Also, I would like to thank my best friend Souzana for always being there for me, *ακόμα και μακρυά..εγώ και εσύ μαζί*.. Last but not least comes my Evan to whom I really ought to dedicate this thesis. Thank you for your love and support, for always making me feel like home, and trying to make me smile even in my darkest hours. *Χωρίς εσένα, μπορεί να μην είχα φτάσει ως εδώ.. και παραπέρα*..

This research would not be possible without the support of grants and fellowships. The author has received funding from the UCSC Regent's Fellowship as well as NASA's grant No NNX14AG08G. Simulations were run on the Hyades cluster at UCSC, purchased using the NSF grant No. AST-1229745, as well as on the XSEDE Stampede 2 Texas Advanced Computing Center (TACC) at The University of Texas at Austin.

Be realistic, demand the impossible..

Ernesto Che Guevara

Chapter 1

Introduction

Helioseismology, the study of the solar dynamics through observations of the Sun's oscillations (mainly caused by sound waves), has made remarkable progress over the last three decades and has revealed the structure of the solar interior, hence providing us with details on the Sun's internal structure and rotational profile. The solar interior consists of two distinct regions: the stably stratified radiative zone (RZ) where energy transport is mainly due to photon radiation, from the center to a radius of about $0.7R_\odot$ (where $R_\odot$ is the solar radius) and the convection zone (CZ), where energy transport is mainly due to advective fluid motions, from $0.7R_\odot$ to the surface. The Sun is the only star that we can observe in such great detail through solar telescopes distributed here on Earth (e.g. Global Oscillation Network Group (GONG), Birmingham Solar-Oscillations Network (BiSON)) or in space (e.g. ESA's/NASA's older Solar and Heliospheric Orbiter SOHO satellite or the newest Solar Dynamics Observatory (SDO)). Therefore, helioseismology is of paramount importance since it helps us better understand the Sun which is a typical star, and as a result apply what we learn about it to understand the structure and evolution of other stars, as well.

Similarly to the Sun, other solar-type stars also possess an outer convection

zone which lies on top of a stable radiative region. The interface between convectively unstable and stable stellar regions hosts what are arguably the most poorly understood dynamical processes in stellar evolution. In particular, the bottom of the convection zone is not impenetrable, thus, convective turbulent fluid motions generated in the unstable CZ are able to propagate downwards into the stable zone. These overshooting motions play a significant role in the transport of chemical species, angular momentum and magnetic fields. In the following sections, we discuss their implications in more detail.

1.1 Overshooting/penetrative convection

Convection is a physical process associated with the transport of energy due to the motion of fluid elements via advection. The condition for a system to be convectively stable is satisfied by the Schwarzschild criterion given by

$$\nabla_{\rm rad} < \nabla_{\rm ad}, \tag{1.1}$$

where $\nabla_{\rm rad} = \partial \ln T / \partial \ln p$ is the radiative temperature gradient related to energy transport due to photon radiation and $\nabla_{\rm ad} = (\partial \ln T / \partial \ln p)_{\rm ad}$ is the adiabatic temperature gradient, where T is the temperature and p is the pressure. Convection is ubiquitous in astrophysical settings and although convective transport can be very efficient in stellar interiors, rather little is known about it, since only a small amount of information can be obtained observationally. Furthermore, it cannot be studied experimentally, since stellar parameters, such as for instance the Prandlt number (which is the ratio of the viscosity ν to the thermal diffusivity κ) is many orders of magnitude smaller than unity. Thus, most stellar values are not obtainable with laboratory fluids. Three-dimensional hydrodynamic numerical

simulations of convection are able to provide great insight into this problem, but unfortunately, they cannot capture the enormous range of dynamical timescales and lengthscales known to exist at these extreme parameters due to computational constraints.

Nonetheless, stellar evolution models only require very simple mixing parametrizations in order to be implemented in stellar evolution codes, thus, the astrophysical community typically employs the so-called "mixing length theory", which is an approach that treats convection locally. This theory assumes a fluid element which rises adiabatically due to buoyancy forces over a distance l_m and expands to remain in pressure equilibrium. After having traveled over the distance l_m, it mixes with its surroundings. The length l_m is called the mixing length, and is assumed to be of the order of a pressure scaleheight H_p, such that $l_m = \alpha_{MLT} H_p$, where α_{MLT} is a free parameter. The velocity of the convective elements is also approximated using simple energetic arguments and can then be used to compute the convective heat flux. This local theory often works well in stellar evolution models, but does not, in its basic form, account for overshooting convection. Böhm-Vitense (1958) [11], who presented an in-depth study on mixing length theory, had already thought about the issue of overshoot and its effect on stellar evolution, however the problem re-surfaced much later. Variations on mixing length theory were proposed to model overshooting convection using different non-local formulations but resulted in vastly different answers, something that was explicitly criticized by Renzini (1987) [116]. Therefore, new formulations on the problem were needed.

Later hydrodynamic studies distinguished the dynamics associated with the propagation of the turbulent convective motions from a convectively unstable to a stable region into two regimes ([160]): the overshooting regime, and the penetrative regime (although in the astrophysical community these definitions are

often used interchangeably). In overshooting convection, there is some amount of mixing by the downwelling plumes which travel below the CZ-RZ interface due to inertia, leading to some level of thermal and chemical mixing. However, if this effect is so strong as to actually lead to a completely thermally mixed (adiabatic) region, then this is what is generally referred to as "penetration".

Penetrative/Overshooting convection is a physical process that plays a significant role in stellar evolution, since any kind of mixing beyond the classical boundary set by the Schwarzschild criterion has direct implications on the stars. Stellar surface element abundances and age estimates of stars and stellar clusters depend sensitively on the amount of overshooting in the stable region (e.g.[138, 135, 112, 74]). For instance, in A-type stars core-convective overshooting can change the amount of fuel in the core via the turbulent motions that carry fresh material into it, thus affecting the star's evolution. In the Sun and solar-type stars, deep overshooting could transport lithium into hotter regions somewhat below the base of the convection zone where it is burned, which has been proposed as a possible solution to the lithium depletion problem (e.g. [138, 112, 7]). Other examples where overshooting convection is a key component include deep mixing in massive stars, and abundance anomalies in low mass giants ([112]).

In this doctoral thesis, we are motivated by the dynamics associated with the CZ-RZ interface and we aim to gain a better understanding of the convective overshooting and penetrative processes and their interaction with stable zones, with particular emphasis on solar-type stars and the transport processes there.

1.2 Angular momentum transport near the CZ-RZ interface

In the previous section, we discussed the importance of convective overshoot in mixing through the transport of chemical species, however, overshooting motions can also help in the transport of angular momentum. In this section, we focus on angular momentum transport processes in the Sun for which we have the largest amount of data available.

Helioseismology has provided us with the solar rotational profile revealing that the convection zone rotates differentially, with the equator rotating faster (with a period of ≈ 25 days) than the poles (which rotate with a period of ≈ 35 days). On the other hand, the radiative zone rotates nearly uniformly with a rotation rate of approximately 93% of the equatorial angular velocity at the surface (Fig. 1.1). This sharp transition in the angular velocities occurs within a stably stratified shear layer, the so-called "*tachocline*" owing its name to Spiegel and Zahn (1992) [134], who named it after the combination of two Greek words: "$\tau\acute{\alpha}\chi o\varsigma$" (tacho) which means speed, and "$\kappa\lambda\acute{\iota}\nu\epsilon\iota\nu$" (cline), which means turn.

The overshoot layer in the Sun approximately coincides with the tachocline, hence our study, although not directly associated with the solar tachocline dynamics, is indeed a step towards gaining a better understanding of the dynamical processes within this region.

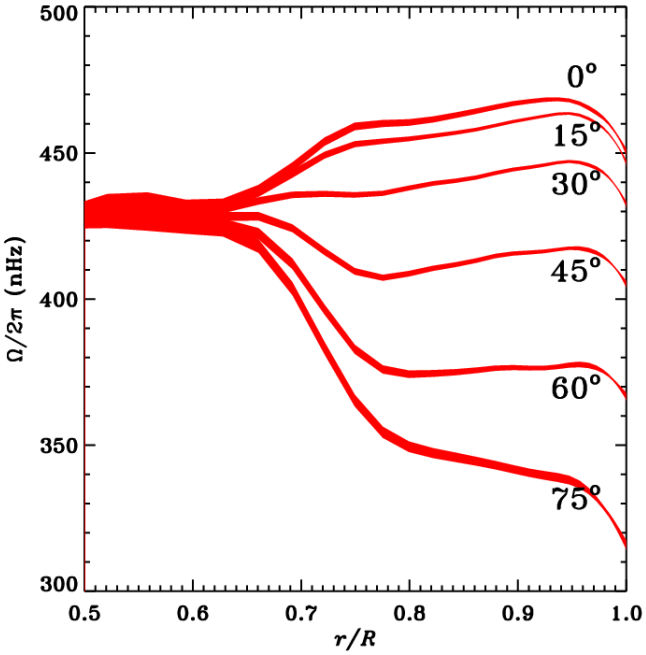

Figure 1.1: The Sun's rotation rate at specified longitudes plotted as a function of the fractional solar radius ([76]). The convection zone rotates diferentially and it transitions to uniform rotation at approximately $r_t = 0.7R_\odot$, i.e. where the tachocline is located.

The tachocline is found to be very thin, less that 5% of the solar radius (e.g. [32]). In fact, its thinness has been a subject of great debate, since the tachocline would be expected to have thickened with time due to the penetration of meridional circulation and the associated advection of the angular momentum. Indeed by assuming axisymmetry, the anelastic approximation, small Rossby numbers associated with rapid rotation, a thin tachocline and geostrophic balance along with the transport of angular momentum solely due to large scale meridional circulation (and viscous diffusion), Spiegel and Zahn (1992) SZ92 found that the tachocline should thicken with time. Given the angular velocity $\Omega(r,\theta,t) \simeq \Omega_o + \hat{\Omega}(r,t)f(\theta)$, where Ω_o is the rotation rate of the Sun's interior, r is the radius, θ is the co-latitude, and t is the time, then the radial function of the perturbations $\hat{\Omega}(r,t)$

satisfies

$$\frac{\partial \hat{\Omega}}{\partial t} + \kappa \left(\frac{r_o}{\lambda}\right)^2 \left(\frac{2\Omega_o}{N}\right)^2 \frac{\partial^4 \hat{\Omega}}{\partial r^4} = 0, \tag{1.2}$$

where κ is the thermal diffusivity, λ is the latitudinal wavenumber of the shear, r_o is the radius at the convective-radiative interface, and N is the buoyancy frequency. From Eq. (1.2), it is apparent that no steady-state can be achieved, thus, the differential rotation will spread into the stable radiative zone, leading to the thickening of the tachocline over time. More specifically, the second term of Eq. (1.2) is a "hyper-diffusion" term which acts on a local Eddington-Sweet timescale $t_{ES} = (N/(2\Omega_o))^2(r_o^2/\kappa)$. This "hyper-diffusive" regime is associated with the propagation of the differential rotation due to angular momentum transport by large-scale meridional circulation. Then, the thickness of the tachocline with respect to time is given by $h(t) = r_o(t/t_{ES})^{1/4}$. Spiegel and Zahn [134] showed that the tachocline should have spread at least half-way of the radius of the Sun. It was also shown that viscous spreading is indeed negligible in comparison to the thermal spreading, at least up to the Sun's present age (see Fig. 1.2).

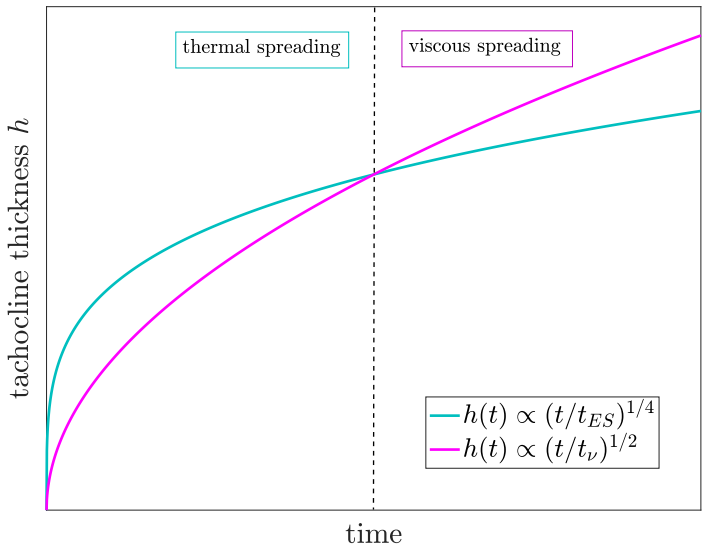

Figure 1.2: The thickness of the tachocline versus time distinguishing between the diffusive and viscous regimes.

Then the question still remained: Why is the tachocline so thin? There have been two major theoretical approaches in explaining its thinness: a hydrodynamic model by Spiegel and Zahn in 1992 [134] and a hydromagnetic model by Gough and McIntyre in 1998 [67] (see also [122, 89]).

1.2.1 The Spiegel and Zahn model

Spiegel and Zahn suggested that the anisotropic turbulent stresses due to horizontal shear instabilities at the base of the CZ might be modeled using an anisotropic turbulent viscosity whose horizontal component ν_H is much larger than the vertical one such that the vertical diffusion of angular momentum can be ignored. In that case, they demonstrated that the spread of the tachocline would

rapidly stop, after achieving a thickness

$$h = r_o \left(\frac{\Omega_o}{N}\right)^{1/2} \left(\frac{\kappa}{\nu_H}\right)^{1/4}. \tag{1.3}$$

1.2.2 The Gough and McIntyre model

Gough and McIntyre (1998)[67] (GM98 thereafter) however argued that the proposed anisotropic turbulence by Spiegel and Zahn cannot explain the almost solid-body rotation of the solar radiative zone, since horizontal turbulent motions mix potential vorticity (instead of angular momentum) which would drive the system away from uniform rotation in the RZ. For that reason, they concluded that other dynamics must be responsible for the thin tachocline and proposed that a magnetic field could actually be the missing key component.

GM98 argued that if there is a primordial dipolar magnetic field confined in the solar radiative zone, it could halt both the spread of the tachocline and enforce solid body rotation in the solar interior through the Ferraro's law of isorotation ([49]). Ferraro's law clearly states that under equilibrium, the angular velocity Ω of a rotating fluid is constant along the magnetic field lines of the axisymmetric poloidal magnetic field $\boldsymbol{B}$ that acts on it such that $\boldsymbol{B} \cdot \nabla\Omega = 0$. In order for his theory to succeed, however, the field needs to be confined in the stable RZ.

Other studies had also built on a confined magnetic field in the RZ to explain the thinness of the tachocline and the solid body rotation of the solar interior (e.g. [122, 89]), but none of them had at that point managed to self-consistently demonstrate how the field could be confined. GM98 were the first to provide a self-consistent model for the tachocline which involved a balance between large-scale meridional flows generated via gyroscopic pumping due to the differential rotation in the convection zone and a large-scale primordial dipolar magnetic field

confined in the radiative zone. They also required a well-mixed and magnetic-free tachocline located below the base of the convection zone, and a thin magnetic boundary layer below the tachocline which they called tachopause (Fig. 1.3). There, the downward advection of the meridional flows balances with the upward diffusion of the poloidal magnetic field. This dynamical interaction results in the halting of the meridional circulation from burrowing further down into the radiative interior and prevents the magnetic field from diffusing outward into the CZ. Below the tachopause, the radiative zone is in uniform rotation.

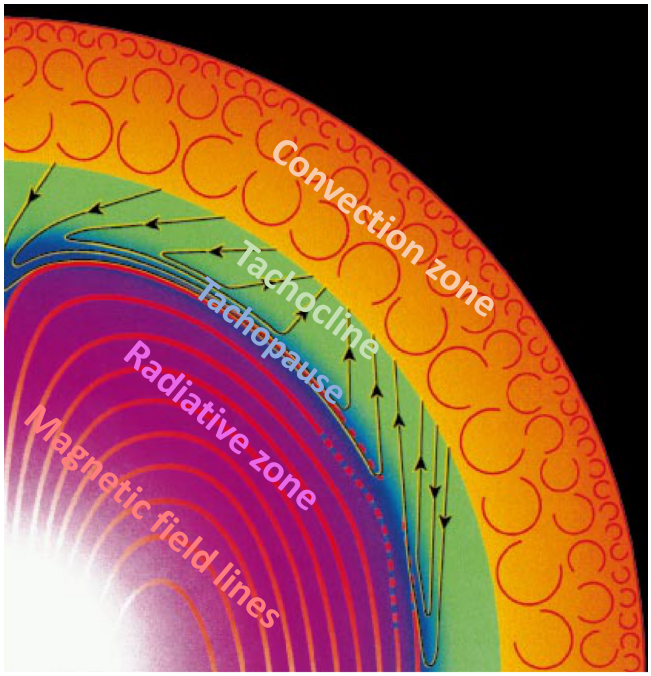

Figure 1.3: Picture of the GM98 model representing the convection zone in orange, the tachocline region in green (much larger than in reality for clarity) along with the meridional flows as black arrows. The tachopause is the blue layer below the tachocline, with the radiative zone in purple. The primordial magnetic field lines are shown in red in the radiative region.

Finally, GM98 used their linearized boundary-layer equations to derive scaling laws based on the balance of these different forces and they suggested relationships between the amplitude of the magnetic field and the thickness of both

the tachopause and the tachocline. In particular, the found the thickness of the tachocline to be $h \propto B_o^{-1/9}$, where B_o is the strength of their primordial magnetic field.

One of the main shortfalls of the GM98 model however was that it was laminar by construction, and ignored the turbulent motions propagating from the CZ down into the stable region. These overshooting motions could play a pivotal role in the tachocline and the tachopause dynamics since they could contribute to the transport of angular momentum and magnetic flux. Wood & McIntyre (2011) [158] suggested that the overshooting motions can "pump" the magnetic field into the overshoot region and this process could help in the confinement of the dipolar fossil magnetic field in the Sun's equatorial regions, which in turn could assist in the formation of the tachocline. GM98 also ignored the existence of the dynamo field in the CZ which could be transported into the tachocline region by the meridional downwelling flows and affect its dynamics. They claimed that the rapidly fluctuating dynamo field related to the solar cycle is rather unlikely to significantly affect the dynamics in the RZ. However, magnetic pumping could actually lead to a dynamical connection of the dipole primordial field with the dynamo one and this could have implications in the tachocline formation.

1.3 Interface dynamos

In the previous sections, we discussed the CZ-RZ interface dynamics in terms of chemical mixing and angular momentum transport. However, comprehending this very dynamically active CZ-RZ interface region is a very important step in also understanding the solar dynamo, the mechanism by which the solar magnetic field is believed to be generated. Indeed, in the standard solar dynamo paradigm, some of the main components are suggested to be located near the base of the CZ ([142]).

Understanding the solar dynamo can in turn lead to a better understanding of the solar magnetic activity cycle and as a result the magnetic stellar activity in general.

The solar cycle defines an almost periodic 11-year change in the Sun's magnetic activity (Fig. 1.4), characterized by the concentrations of magnetic field flux in the solar photosphere, namely the sunspots (Fig. 1.5). The solar magnetic activity has a direct impact on human life with examples including the terrestrial weather, the Earth's upper atmosphere, humans in space and in commercial aviation, as well as spacecraft electronics or ground electric power grids.

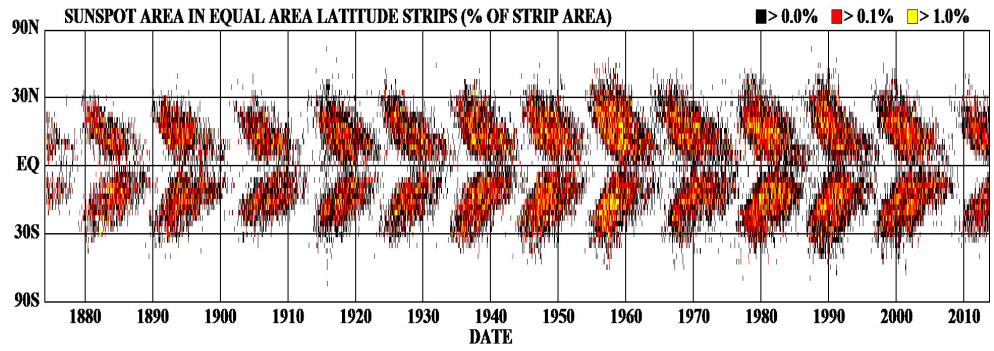

Figure 1.4: NASA's butterfly diagram illustrating the spatio-temporal histogram of the Sun's activity cycle and its 11-year periodicity.

One of the most fundamental existing dynamo theories is that the solar magnetic cycle is a result of a mean-field $\alpha\Omega-$dynamo process. The $\alpha-$effect refers to the generation of large-scale poloidal magnetic fields from toroidal fields due to small-scale turbulence (in the mean field parameterized sense), whereas the $\Omega-$effect is related to the generation of toroidal fields from poloidal fields due to differential rotation.

The tachocline is the best candidate region for the $\Omega-$effect, where the strongest toroidal fields can be locally generated and held down due to magnetic pumping

by overshooting convection. The location of the $\alpha-$effect is however less obvious.

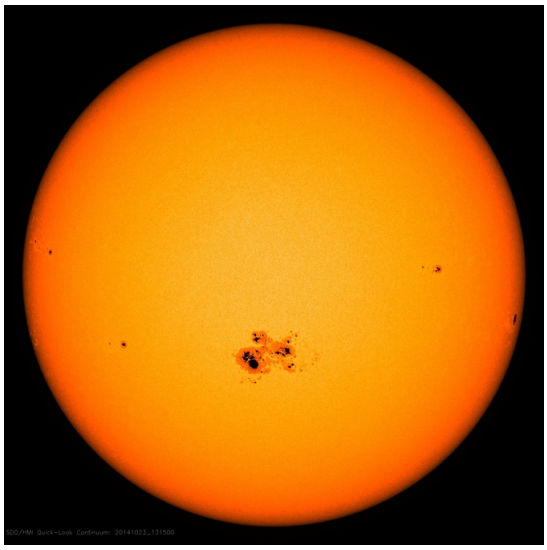

Figure 1.5: NASA/SDO picture of a huge sunspot (approximately spanning 80,000 miles) close to the lower center of the Sun.

Parker (1993) [109] (see also [33]) suggested the idea of an "interface dynamo", namely a two-layered configuration where the $\alpha-$effect (associated with the generation of weak poloidal magnetic fields) takes place in the CZ where the turbulent eddies reside, while the $\Omega-$effect (related to the generation of strong toroidal magnetic fields) occurs within the tachocline region. In his setup, Parker also assumed discontinuous magnetic diffusivities across the interface of the two layers, which ensures that the toroidal field will be much weaker in the lower part of the CZ (i.e. above the interface) due to the larger turbulent magnetic diffusivity there. As a result, the turbulence will not be suppressed within that region, thus allowing for the $\alpha-$effect to persist, i.e. avoiding $\alpha-$quenching. In that way, the poloidal field can indeed be generated in the CZ and get pumped downwards. The interface dynamo solutions then take the form of dynamo surface waves that can propagate along the interface between the α and Ω regions.

Concluding this section, we note that this interface region between the turbu-

lent CZ and the stable RZ plays a significant role in the generation, transport and interaction of magnetic fields between the two zones as we shall see in Chapter 4 of this thesis. Revisiting the GM98 model, one of its most important uncertainties was that it did not account for turbulence and the solar dynamo field and their possible interaction with the primordial dipole field in the RZ. This was initially studied by Garaud (1999) [53] who assumed the diffusion of random fluctuations of a poloidal magnetic field in the RZ and its dynamical interaction with the tachocline and the interior and later by e.g. Forgács-Dajka & Petrovay (2001) [51], who focused on the confinement of the tachocline via an oscillatory poloidal magnetic field close the CZ-RZ interface. However, the study of the interaction of a dynamo field with the primordial magnetic field in the RZ has not been studied with 3D direct numerical simulations yet.

1.4 Basic model setup

Motivated by the dynamics associated with different physical processes taking place in a solar-like CZ-RZ interface, where a convectively unstable region lies on top of a stably stratified zone, we are particularly interested in gaining a better understanding of processes such as overshooting convection, and the interaction of the overshooting flow motions with magnetic fields. For this purpose, we have divided this thesis into three distinct projects.

In the first one, we initially study convection in a spherical shell in a new formulation aimed at mimicking stellar-like conditions, and then in the second one we extend these dynamics to include a stable radiative zone and therefore allow for overshooting/penetrative convection. Finally, we incorporate magnetic fields and focus on the interaction of the convective turbulent motions with a poloidal dipole magnetic field initially confined in the stable region.

In Chapter 2, we begin by considering the convective zone only, and we investigate the effect of a non-zero adiabatic temperature gradient and mixed thermal boundary conditions on the convective dynamics, in a spherical shell geometry. We use a new formulation which accounts for more stellar-like conditions. Our model setup for that is shown in Figure 1.6. The inner boundary of the convection zone is located at $r_i = 0.7r_o$ while the outer radius is at r_o. We assume fixed flux boundary condition at r_i, since this is what is set by the luminosity of the star, due to the nuclear burning at the stellar core.

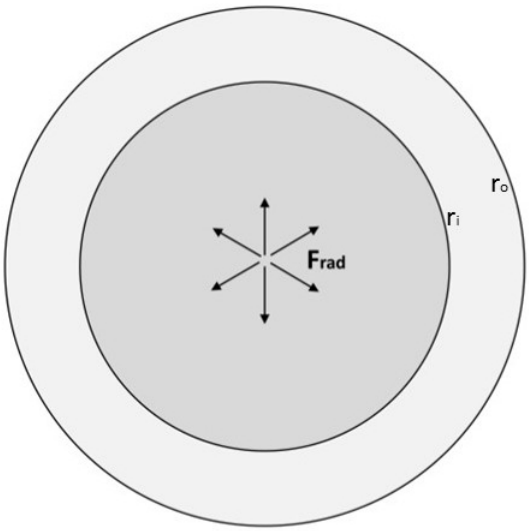

Figure 1.6: Model setup for our spherical shell with an inner radius at $r_i = 0.7r_o$ and an outer radius at r_o. The aspect ratio $r_i/r_o = 0.7$ is held fixed in all of the cases studied.

In Chapter 3, we extend the problem studied in Chapter 2 by adding a convectively stable region below the nominal convection zone. Now the inner boundary is located at $r_i = 0.2r_o$, the transition between the two regions is at $r_t = 0.7r_o$ and the outer boundary is again at r_o (Figure 1.7). In this chapter, we study the dynamics associated with the overshooting of the turbulent motions generated in the CZ into the stable region and the dependence of overshooting on different

input parameters.

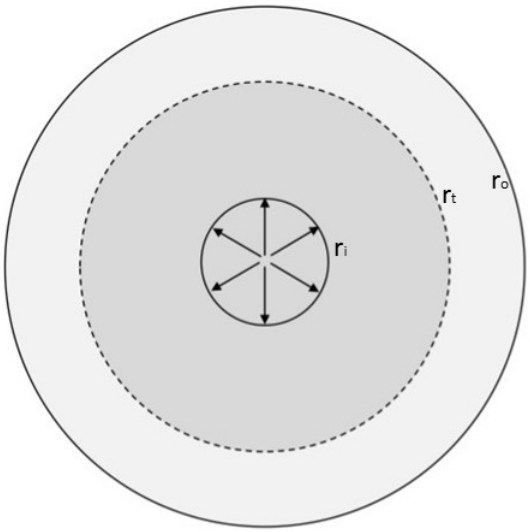

Figure 1.7: Model setup for our spherical shell with a stable region for $r \in [r_i, r_t)$, and a convective region for $r \in [r_t, r_o]$, where $r_i = 0.2r_o$ and $r_t = 0.7r_o$.

In Chapter 4, we adapt the equations to incorporate magnetic fields and we add a magnetic field in the radiative zone and study the effect of the overshooting motions on the field. We are particularly interested in investigating if overshooting motions alone can confine a primordial magnetic field in the interior, as suggested by Garaud & Rogers (2007) [56] and later shown by e.g. Kitchatinov & Rüdiger (2008) [83]. Hence, we add a dipole magnetic field in the stable region as shown in Figure 1.8, and we focus on the interaction of the turbulent convective motions with this weak fossil poloidal field, initially confined in the RZ.

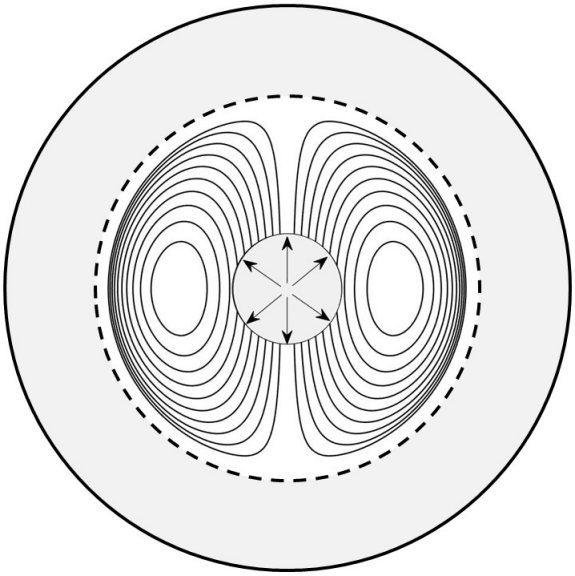

Figure 1.8: Model setup as in Fig. 1.7, with a dipole poloidal magnetic field initially confined in the radiative interior below $r = 0.65 r_o$.

Finally, in Chapter 5, we conclude this thesis with a brief summary of our work and some ideas of future goals in these subjects.

Chapter 2

Weakly non-Boussinesq convection in a gaseous spherical shell

The following chapter is composed of the main text of Korre et al. (2017) [84], published in Physical Review E in September 2017. The co-authors of this work are Nicholas Brummell and Pascale Garaud, both professors in the Department of Applied Mathematics at the University of California, Santa Cruz.

2.1 Introduction

Convection is a ubiquitous physical process in geophysical fluid dynamics, which has been extensively studied analytically, experimentally and numerically because of the vital role it plays in the global dynamics of the Earth's mantle (e.g. [9, 64, 15] and for a review see [125] and references therein), oceans [94] and atmosphere [48]. Convection is also important in astrophysical settings such as the gaseous interiors of stars and planets where the convective zones are usually

global, either spanning the entire object or at least a deep spherical shell. By contrast with geophysical convection, relatively little is known about convection in astrophysical objects. Observationally speaking, a limited amount of information can be obtained either through direct imaging of the surface (e.g. see [117] for a review), or indirectly using asteroseismology to infer, for instance, the mean temperature profile within the convection zone [66]. Meaningful physical experiments are almost impossible to design because the governing parameters appropriate to the interiors of stars and planets are vastly different from those achievable in a laboratory. In particular, the Prandtl number, which is the ratio of the kinematic viscosity to the thermal diffusivity, is much smaller than unity in astrophysical plasmas (e.g. $\sim 10^{-2}$ in giant planets, and $\sim 10^{-6}$ in stars) whereas it is usually of order unity or much larger in geophysical applications. Among other things, this implies that the ordering of the relevant dynamical timescales is different in the two regimes, and that the effects of the inertial terms in astrophysical convection are much larger than in geophysical convection.

In this paper, we attempt to shed new light on the subject by investigating the dynamics of convection in weakly compressible gaseous spherical shells in the low Prandtl number parameter regime using direct numerical simulations (DNSs) with mixed temperature boundary conditions (here meant to imply fixed flux at the inner boundary and fixed temperature at the outer boundary). This setup is designed to capture some of the most salient features of convection in stars and giant planets, and differs in significant ways from most studies of convection to date.

Arguably, the most commonly studied form of convection is thermal Rayleigh-Bénard convection (RBC thereafter) between two parallel plates where a Boussinesq liquid (in the original Boussinesq sense [12, 106]) is heated from below and

cooled from above, and the two rigid boundaries are held at constant temperatures. For sufficiently strong driving, as measured by the Rayleigh number, buoyancy forces overcome thermal and viscous damping and turbulent heat transport by convection dominates conduction. This highly symmetric idealized model setup has been studied extensively in both 2D and 3D [154, 102, 128, 81, 70] (also for a general review of RBC see [2] and references therein).

When studying geophysical problems, several extensions of this basic model are usually considered depending on the specific application. Studies of mantle convection usually adopt a spherical shell geometry and consider the limit of infinite Prandtl number [31, 26, 163, 126, 162, 90, 10, 150, 79, 34]. More generally, geophysically motivated studies of convection in spherical shells sometimes include the effect of rotation or allow for a finite Prandtl number [47, 141, 50, 58, 57] but have so far nearly always used fixed temperature boundary conditions. The majority of these investigations have focused on the derivation of scaling laws for global quantities such as the heat flux or the total kinetic energy as functions of input parameters, as well as developing models for the boundary layers (see [69] for a review).

In astrophysical applications, on the other hand, the fluid is generally compressible. Solving the compressible Navier-Stokes equations requires the resolution of timescales associated with fast sound waves, as well as the much slower timescales associated with global thermal or viscous adjustment. This stiffness is a severe impediment to simulation and filtering out the fast sonic dynamics is often desirable. One way of accounting for weak compressibility in astrophysical convection is through the anelastic approximation [8, 107, 65, 85, 63], which filters out sound waves while allowing for strong variations in the background density. This is the more commonly adopted formalism for the study of solar convection

([97] and references therein) and stellar convection (e.g. [19, 16, 5, 17]) but it has significant drawbacks. First of all, there are numerous formulations of the approximation and there is some debate about their relative validity [151, 152]. Secondly, the anelastic approximation is usually based on the assumption of small departures from adiabaticity which is not guaranteed in all reasonable problems.

Another commonly used approximation under which sound waves are filtered out is the Boussinesq approximation for gases [133]. It is important to note that the *standard* Boussinesq approximation [12, 106] should not be used in astrophysical applications because of the compressibility of the gas (although it is still sometimes used for simplicity [60, 61, 62, 35, 72, 71, 6]). However, Spiegel & Veronis (1960) [133] (SV thereafter) showed that it is possible to generalize the approximation to take into account some effects of compressibility, thereby allowing its use in modeling convection in gaseous systems, such as the Earth's atmosphere or the interiors of stars and planets. Assuming that the size of the convective region is much smaller than any scale height of the system (including the local radius, if the convection zone is a spherical shell), and that the fluid motions are much slower than the local speed of sound, they showed that the only effect of compressibility is to heat or cool a parcel of fluid as it shrinks or expands to adjust to the ambient hydrostatic pressure. As a result, their formulation contains an additional term in the temperature equation which is proportional to the local adiabatic temperature gradient (which is non-zero for gases) but is otherwise identical to the traditional Boussinesq approximation. Studies of astrophysical convection in Cartesian geometry or in a very thin spherical shell using the SV Boussinesq (SVB thereafter) approximation were presented for instance in [28] and [96].

In this work we propose to study 3D DNSs of low Prandtl number convection

in a spherical geometry using the SVB equations with particular applications to solar and stellar convection in mind. We therefore deviate from the usual assumption of fixed temperature boundary conditions and instead, consider a more astrophysically realistic setup with fixed flux at the inner boundary and fixed temperature at the outer boundary. Indeed, in stars like the Sun for instance, the flux through the base of an outer convection zone is fixed by the luminosity of the star, which in turn is set by the nuclear generation rate within the core.

These four elements (spherical geometry, weak compressibility, mixed temperature boundary conditions and low Prandtl number) have never, to the authors' knowledge, been used in conjunction and yet are all crucial elements of astrophysical convection.

The chapter is organized as follows: Sections 2.2 and 2.3 present two different model setups that both possess all four properties listed above, and report on the results of a suite of numerical simulations for varying Rayleigh number. Surprising new dynamics are observed, which are then analyzed and explained in detail in Section 2.4. In Section 2.5, we explore a third model setup which more closely resembles the Sun (although still simplistically), in order to test the robustness of our results and to assess the applicability of what we have found to the circumstances that most interest us. Finally, in Section 2.6, we summarize our results and discuss the possible limitations of the SVB approximation.

2.2 Boussinesq convection in a weakly compressible spherical shell

2.2.1 Mathematical formulation

We begin our systematic investigation of the effects of mixed temperature boundary conditions and weak compressibility on the dynamics of Rayleigh-Bénard convection in a spherical shell by constructing the simplest possible model with these properties. In this model, and in all of the ones that follow, we consider a spherical shell located between an inner sphere of radius r_i and an outer sphere of radius r_o. For simplicity, we assume constant thermal expansion coefficient α, viscosity ν, thermal diffusivity κ, adiabatic temperature gradient $dT_{\rm ad}/dr$ and gravity g. In the absence of fluid motion and when the system is in a steady state, the background radiative temperature gradient is obtained by solving

$$\kappa\nabla^2 T_{\rm rad}(r) = 0 \Rightarrow \kappa r^2 \frac{dT_{\rm rad}}{dr} = \text{const}, \tag{2.1}$$

where r is the local radius. The inner fixed flux boundary condition implies that

$$-\kappa \frac{dT_{\rm rad}}{dr}\bigg|_{r=r_i} = F_{\rm rad}, \tag{2.2}$$

where $F_{\rm rad}$ is the temperature flux per unit area through the inner boundary, whereas the outer fixed temperature boundary condition is $T(r_o) = T_o$. Then, solving Eq. (2.1) using the first boundary condition implies that

$$\frac{dT_{\rm rad}}{dr} = -\frac{F_{\rm rad}}{\kappa}\left(\frac{r_i}{r}\right)^2, \tag{2.3}$$

which, along with the second boundary condition, gives

$$T_{\rm rad}(r) = \frac{F_{\rm rad} r_i^2}{\kappa}\left(\frac{1}{r} - \frac{1}{r_o}\right) + T_o. \tag{2.4}$$

We clearly see that, in contrast to the Cartesian case, the radiative temperature gradient in a spherical geometry is not constant but depends on the radius. This implies in turn that $dT_{\rm rad}/dr - dT_{\rm ad}/dr$ also varies with depth. Note that for the SVB approximation to be valid, $\Delta T = T_{\rm rad}(r_i) - T_{\rm rad}(r_o)$ must be much smaller than, say, T_o. This is true either for small enough $r_o - r_i$ (thin layer) given $F_{\rm rad}$, or for small enough $F_{\rm rad}$ given $r_o - r_i$. We solve the equations (2.8)–(2.10) as described in Chapter 1.

We now let $T(r,\theta,\phi,t) = T_{\rm rad}(r) + \Theta(r,\theta,\phi,t)$ where Θ is the temperature perturbation to the radiative background. We also assume a linear relationship between the temperature and density perturbations consistent with the SVB approximation, $\rho/\rho_m = -\alpha\Theta$, where ρ_m is the mean density of the background fluid. With these assumptions, the governing SVB equations are:

$$\nabla \cdot \boldsymbol{u} = 0, \tag{2.5}$$

$$\frac{\partial \boldsymbol{u}}{\partial t} + \boldsymbol{u}\cdot\nabla\boldsymbol{u} = -\frac{1}{\rho_m}\nabla p + \alpha\Theta g \boldsymbol{e_r} + \nu\nabla^2\boldsymbol{u}, \tag{2.6}$$

and

$$\frac{\partial \Theta}{\partial t} + \boldsymbol{u}\cdot\nabla\Theta + u_r\left(\frac{dT_{\rm rad}}{dr} - \frac{dT_{\rm ad}}{dr}\right) = \kappa\nabla^2\Theta, \tag{2.7}$$

where $\boldsymbol{u} = (u_r, u_\theta, u_\phi)$ is the velocity field, and p is the pressure. We non-dimensionalize the problem by using [1] $[l] = r_o$, $[t] = r_o^2/\nu$, $[u] = \nu/r_o$ and

[1] We numerically solve the non-dimensional Boussinesq equations in which we have used the outer radius as the lengthscale. If we wanted to compare spherical numerical simulations with Cartesian ones, we would have to non-dimensionalize the problem using the thickness of the shell $[l] = r_o - r_i = L$ such that both the problems could have the same effective Rayleigh number

$[T] = |dT_o/dr - dT_{\rm ad}/dr|r_o$ as the unit length, time, velocity and temperature, where $dT_o/dr \equiv dT_{\rm rad}/dr|_{r=r_o}$. Then, we can write the non-dimensional equations as:

$$\nabla \cdot \boldsymbol{u} = 0, \tag{2.8}$$

$$\frac{\partial \boldsymbol{u}}{\partial t} + \boldsymbol{u} \cdot \nabla \boldsymbol{u} = -\nabla p + \frac{\mathrm{Ra}_o}{\mathrm{Pr}} \Theta \boldsymbol{e_r} + \nabla^2 \boldsymbol{u}, \tag{2.9}$$

and

$$\frac{\partial \Theta}{\partial t} + \boldsymbol{u} \cdot \nabla \Theta + \beta(r) u_r = \frac{1}{\mathrm{Pr}} \nabla^2 \Theta. \tag{2.10}$$

All the variables and parameters are now implicitly non-dimensional, which introduces the Prandtl number Pr and the Rayleigh Ra_o defined as

$$\mathrm{Pr} = \frac{\nu}{\kappa} \quad \text{and} \quad \mathrm{Ra}_o = \frac{\alpha g \left| \dfrac{dT_o}{dr} - \dfrac{dT_{\rm ad}}{dr} \right| r_o^4}{\kappa \nu}, \tag{2.11}$$

and the non-dimensional superadiabaticity. Here, we can rewrite the non-dimensional superadiabaticity as:

$$\beta(r) = \frac{\dfrac{dT_{\rm rad}}{dr} - \dfrac{dT_{\rm ad}}{dr}}{\left| \dfrac{dT_o}{dr} - \dfrac{dT_{\rm ad}}{dr} \right|} = \frac{\left(\dfrac{1}{r}\right)^2 \dfrac{dT_o}{dr} - \dfrac{dT_{\rm ad}}{dr}}{\left| \dfrac{dT_o}{dr} - \dfrac{dT_{\rm ad}}{dr} \right|}. \tag{2.12}$$

Another way to interpret β is to note that it is minus the ratio of the local Rayleigh number $\mathrm{Ra}(r)$ to Ra_o i.e.

$$\beta(r) = -\frac{\mathrm{Ra(r)}}{\mathrm{Ra_o}}, \tag{2.13}$$

for accurate comparison.

where

$$\mathrm{Ra}(r) = \frac{\alpha g \left| \frac{dT_{\mathrm{rad}}}{dr} - \frac{dT_{\mathrm{ad}}}{dr} \right| r_o^4}{\kappa\nu} = \frac{\alpha g \left| -\frac{F_{\mathrm{rad}}}{\kappa} \left(\frac{r_i}{r}\right)^2 - \frac{dT_{\mathrm{ad}}}{dr} \right| r_o^4}{\kappa\nu}. \tag{2.14}$$

Finally, note that while β seems to depend on two dimensional quantities dT_{rad}/dr and dT_{ad}/dr (see Equation (2.12)), it can be rewritten in this simple model just in terms of a single non-dimensional parameter χ, defined as

$$\chi = \left| \frac{\frac{dT_o}{dr} - \frac{dT_{\mathrm{ad}}}{dr}}{\frac{dT_o}{dr}} \right| = \left| 1 + \frac{\kappa \frac{dT_{\mathrm{ad}}}{dr} r_o^2}{F_{\mathrm{rad}} r_i^2} \right|, \tag{2.15}$$

so that

$$\beta(r) = \frac{1 - \chi - (1/r)^2}{\chi}. \tag{2.16}$$

Note that $\beta(1) = -1$ and $\beta(r_i/r_o) = (1 - \chi - (r_o/r_i)^2)/\chi$.

Figure 2.1 illustrates how β, and therefore the local Rayleigh ratio $\mathrm{Ra}(r)/\mathrm{Ra}_o$, depends on χ. Note that for $\chi = 0.5$ the local Rayleigh number at the inner boundary is about 3 times larger than Ra_o, whereas for $\chi = 0.1$, it is 11 times larger, illustrating that a small χ implies a stronger variation of the local Rayleigh number across the shell. In the limit of a very thin shell ($r_i/r_o \to 1$) on the other hand (which recovers the case of convection between infinite parallel plates), $\beta(r)$ tends to the constant -1 regardless of χ. The functional form of β therefore depends on our choice of boundary conditions and on the fact that we are operating in an appreciably deep spherical shell (see Equation (2.16)).

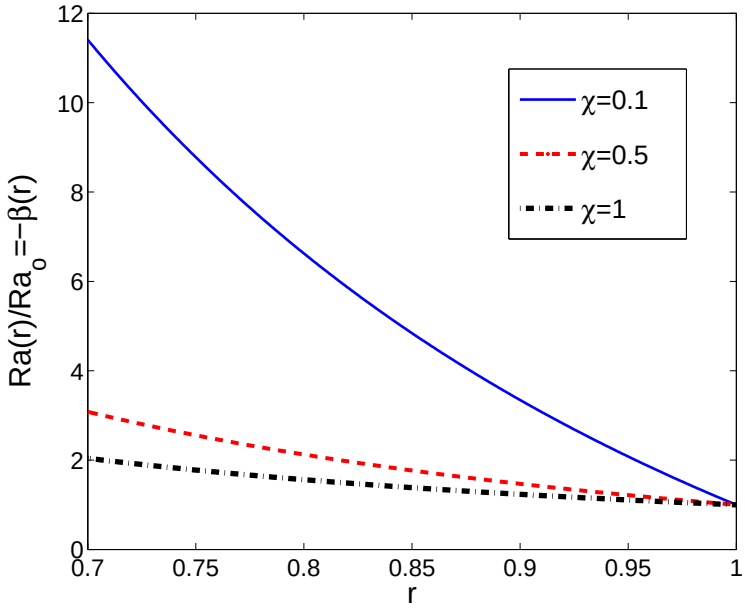

Figure 2.1: The dependence of $\beta(r)$ on χ.

2.2.2 Numerical simulations

In order to study the influence of weak compressibility and sphericity (which manifest themselves in a variable $\beta(r)$), and of mixed temperature boundary conditions on the model dynamics, we have run 3D DNSs solving Equations (2.8)-(2.10) in a spherical shell, exactly as outlined above, using the PARODY code [46, 4]. The boundary conditions for the temperature perturbations Θ are such that we have fixed flux at the inner boundary, $\partial\Theta/\partial r|_{r_i} = 0$ and fixed temperature at the outer boundary, $\Theta(r_o) = 0$. The velocity boundary conditions are stress-free at both the inner and outer boundaries. The simulations discussed in this section are referred to as "Model A" simulations. Table 2.1 summarizes our various runs in this setup, as well as those later discussed in Sections 2.3 and 2.5. Note that $r_i/r_o = 0.7$ and $\mathrm{Pr} = 0.1$ for all the simulations presented in this chapter.

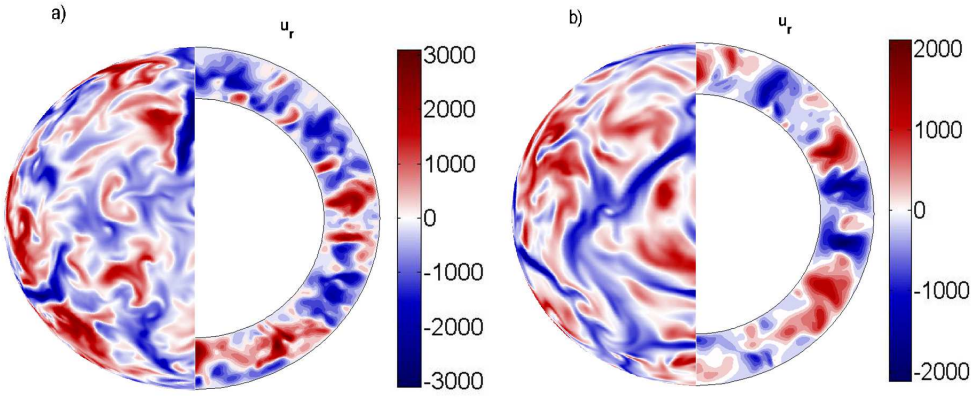

Figure 2.2: Snapshot of the radial velocity u_r for a) $\chi = 0.1$ and b) $\chi = 0.5$ and $\mathrm{Ra}_o = 10^7$. In each panel, the left part shows the u_r field close to the outer radius just below the boundary layer. The right part shows the same field u_r on a selected meridional plane.

We now examine the qualitative and quantitative properties of our simulations, focusing on three typical cases with varying χ ($\chi = 0.1$, $\chi = 0.5$ and $\chi = 1$) for fixed $\mathrm{Ra}_o = 10^7$. A simple way of visualizing the turbulent motions due to convection is to look at snapshots of the velocity components u_r, u_θ or u_ϕ at a typical time after saturation of the linear instability. Figure 2.2 shows snapshots of u_r. In each panel, the left hemisphere shows the velocity field on a spherical shell close to the upper boundary, illustrating the convective motions near the surface. The right hemisphere is a meridional slice showing the radial velocity as a function of depth and latitude, for a selected longitude. Figure 2.2(a) is for $\chi = 0.1$, while Figure 2.2(b) is for $\chi = 0.5$. We notice that the $\chi = 0.1$ case appears somewhat more turbulent than the $\chi = 0.5$ case, as visualized by stronger eddies with a wider range of scales.

To see more clearly any difference among the runs, we turn to more quantitative measures. Figure 2.3(a) shows the kinetic energy per unit volume E_k within the shell as a function of time for the Model A simulations (solid blue line with circles for $\chi = 0.1$, solid red line with diamonds for $\chi = 0.5$, and solid black line

with asterisks for $\chi = 1$). We clearly observe the initial development of the convective instability, visible as a large spike in the interval $t \in [0, 0.01]$, followed by its nonlinear saturation. Note that $E_k(t)$ reaches a stationary state very fast but reaching thermal equilibrium is a much slower process. We estimate that a simulation has reached thermal equilibrium when $\partial\Theta/\partial r|_{r=r_o}$ is statistically stationary and equal to zero. This happens around $t \approx 0.02$ for the $\chi = 1$, $\chi = 0.5$ and $\chi = 0.1$ simulations. In all that follows, we only present the results of simulations once they have achieved thermal equilibrium.

Figure 2.3(a) shows that $E_k(t)$ is much larger for the $\chi = 0.1$ run than for cases with larger χ, confirming our rapid visual inspection of Figure 2.2. To understand why this may be the case, recall that for smaller values of χ the local Rayleigh number $\mathrm{Ra}(r)$ increases more with depth than for larger χ (Fig. 1). A higher Rayleigh number near the lower boundary drives convection more vigorously, which increases the overall kinetic energy.

Throughout the chapter, we define the time- and spherical- average of a quantity as

$$\bar{q}(r) = \frac{1}{4\pi(t_2 - t_1)} \int_{t_1}^{t_2} \int_0^{2\pi} \int_0^{\pi} q(r, \theta, \phi, t) \sin\theta d\theta d\phi dt. \tag{2.17}$$

Figure 2.3(b) shows the non-dimensional kinetic energy profiles $\bar{E}_k(r)$ given by

$$\bar{E}_k(r) = \frac{1}{2}(\overline{u_r^2 + u_\theta^2 + u_\phi^2}). \tag{2.18}$$

The forms of these profiles look similar for $\chi = 0.1$, $\chi = 0.5$ and $\chi = 1$, taking their highest value at the top of the convection zone and then decreasing inward to a plateau from approximately $r = 0.95$ down to $r = 0.75$. Below $r = 0.75$, there is a small increase in the kinetic energy associated with the inner boundary layer. As we already saw in Figure 2.3(a), the $\chi = 0.1$ case has significantly higher

kinetic energy than the other runs. Somewhat surprisingly, however, the kinetic energy is larger everywhere even though $\mathrm{Ra}(r)/\mathrm{Ra}_o$ is only larger near the inner boundary. This could be explained by the fact that the convection in this model is a highly non-local process i.e. that stronger driving deeper down implies strong upflows and downflows throughout the domain.

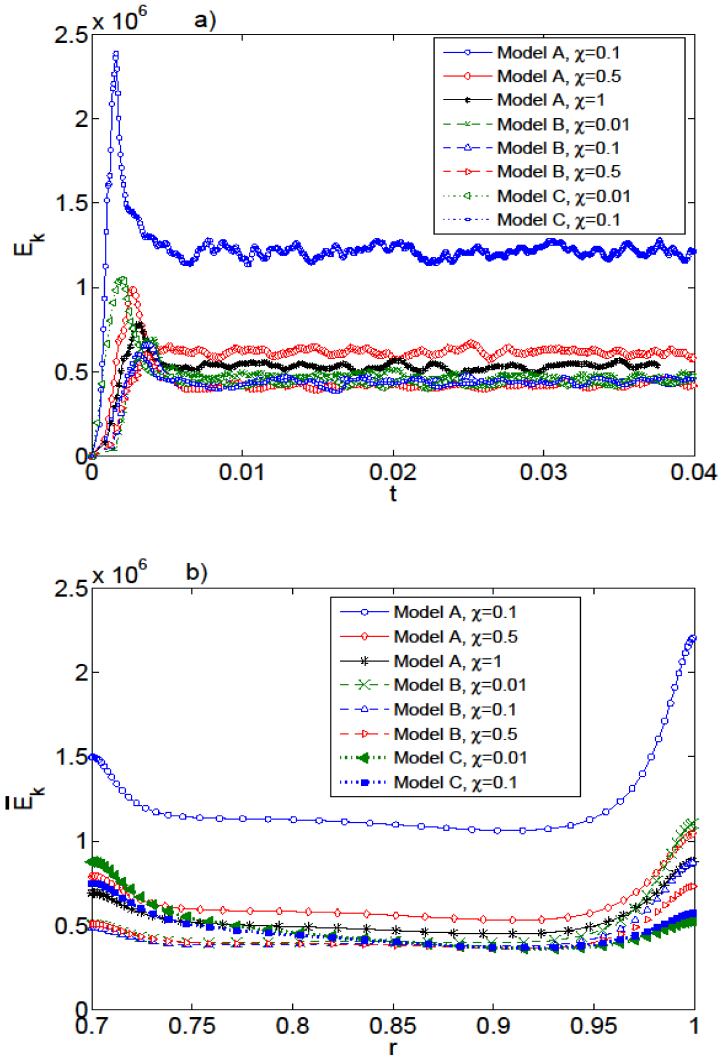

Figure 2.3: *a)* Non-dimensional kinetic energy per unit volume as a function of time for Model A (solid blue line with circles for $\chi = 0.1$, solid red line with diamonds for $\chi = 0.5$, and solid black line with asterisks for $\chi = 1$), Model B (dashed green line with crosses for $\chi = 0.01$, dashed blue line with upward-pointing triangles for $\chi = 0.1$, and dashed red line with right-pointing triangles for $\chi = 0.5$) and Model C (dotted green line with left-pointing triangles for $\chi = 0.01$, and dotted blue line with squares for $\chi = 0.1$) for $\mathrm{Ra}_o = 10^7$, and three different χ. *b)* Time-averaged kinetic energy profile as a function of radius, for the same simulations.

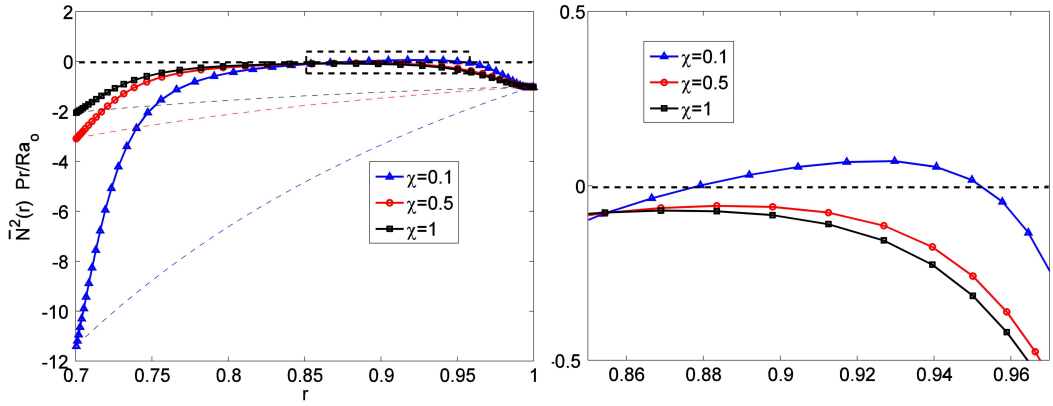

Figure 2.4: Profile of $\bar{N}^2\mathrm{Pr}/\mathrm{Ra}_o$ (solid line with markers) compared with $N^2_{\mathrm{rad}}\mathrm{Pr}/\mathrm{Ra}_o$ (thin dashed line) for $\chi = 0.1$, $\chi = 0.5$, $\chi = 1$ and for $\mathrm{Ra}_o = 10^7$. The right figure is a zoom-in of the dashed box in the left figure i.e. the range where the subadiabatic region emerges.

In Figure 2.4, we plot the square of the non-dimensional buoyancy frequency

$$\bar{N}^2(r) = \alpha g \left(\frac{d\bar{T}}{dr} - \frac{dT_{\mathrm{ad}}}{dr} \right) \frac{r_o^4}{\nu^2} = \left(\beta(r) + \frac{d\bar{\Theta}}{dr} \right) \frac{\mathrm{Ra}_o}{\mathrm{Pr}}, \tag{2.19}$$

(solid lines with markers) for $\chi = 0.1$, $\chi = 0.5$, $\chi = 1$ and $\mathrm{Ra}_o = 10^7$. We also show the square of the background buoyancy frequency $N^2_{\mathrm{rad}}(r) = \beta(r)\mathrm{Ra}_o/\mathrm{Pr}$ as a thin dashed line for reference. As expected, we find that convective motions outside the boundary layers generally mix potential temperature and drive the mean radial temperature gradient towards an adiabatic state where $\bar{N}^2 \approx 0$. However, subtle differences arise when χ decreases, which manifest themselves in two different ways. Firstly, note that for lower χ, $|N^2_{\mathrm{rad}}|$ is much larger, consistent with stronger convective driving. Nonetheless, even though the kinetic energy per unit volume is larger, we see that the interior is not mixed as well for $\chi = 0.1$ as for $\chi = 0.5$ and $\chi = 1$. Secondly, for $\chi = 0.1$, we observe the surprising emergence of a slightly subadiabatic region ($\bar{N}^2 > 0$) just below the upper boundary layer.

This remarkable behavior, namely the emergence of a layer in the flow that

is subadiabatic and therefore ostensibly convectively stable, only occurs for the lowest value of χ we were able to simulate. Proceeding to lower χ to test the robustness of this observation would be an obvious path, but one that is numerically difficult. For example, using $\chi = 0.01$ would require the Rayleigh function $\mathrm{Ra}(r)$ to reach values of approximately $100\mathrm{Ra}_o$ at the inner boundary. Such a range is hard to resolve. For this reason, and furthermore to elicit which of the physics elements are responsible for the unexpected emergence of a subadiabatic layer, we now switch to a different model setup (Model B).

2.3 Spherical shell with a constant Rayleigh function

In the Model A simulations discussed in the previous section, both $\beta(r)$ and the local Rayleigh number $\mathrm{Ra}(r)$ vary with depth proportionally to one another. As a result, it is difficult to determine what may be the direct cause of some of the interesting features we observe. Thus, we construct a second model (called "Model B") where $\beta(r)$ is the same as in Section 2.2, but where $\mathrm{Ra}(r)$ is constant across the convection zone. We can achieve this by varying the thermal expansion coefficient α with radius in order to compensate for the radial variation of $dT_{\mathrm{rad}}/dr - dT_{\mathrm{ad}}/dr$. Continuing to assume that κ, ν and g are constant, we now choose $\alpha(r)$ such that $\mathrm{Ra}(r)$=Ra_o. That is,

$$\mathrm{Ra}(r) = -\frac{\alpha(r) g \left(\dfrac{dT_{\mathrm{rad}}}{dr} - \dfrac{dT_{\mathrm{ad}}}{dr} \right) r_o^4}{\kappa\nu} = -\mathrm{Ra}_o \frac{\alpha(r)}{\alpha_o} \beta(r) \equiv \mathrm{Ra}_o \tag{2.20}$$

as long as $\alpha(r)/\alpha_o \equiv -1/\beta(r)$, where $\alpha_o = \alpha(r_o)$. In this new setup, the non-dimensional momentum equation is

$$\frac{\partial \boldsymbol{u}}{\partial t} + \boldsymbol{u}\cdot\nabla\boldsymbol{u} = -\nabla p + \frac{\alpha(r)}{\alpha_o}\frac{\mathrm{Ra}_o}{\mathrm{Pr}}\Theta\boldsymbol{e_r} + \nabla^2\boldsymbol{u}, \tag{2.21}$$

while the thermal energy equation remains unchanged, and is given by Eq. (2.10).

Figure 2.5 shows the variation of α needed to keep the Rayleigh function constant for our fiducial values of χ. In all cases, $\alpha(r)$ decreases with depth, and $\alpha(r_i)/\alpha_o$ is smaller for smaller χ. Physically speaking, this implies that the effective buoyancy of fluid elements with fixed temperature perturbation Θ decreases with depth. Note that, in contrast with Model A, Model B now explicitly violates the conditions of use of the SVB approximation when χ is small. This will be discussed in Section 2.6, but lends credence to our use of the paper title "weakly non-Boussinesq convection".

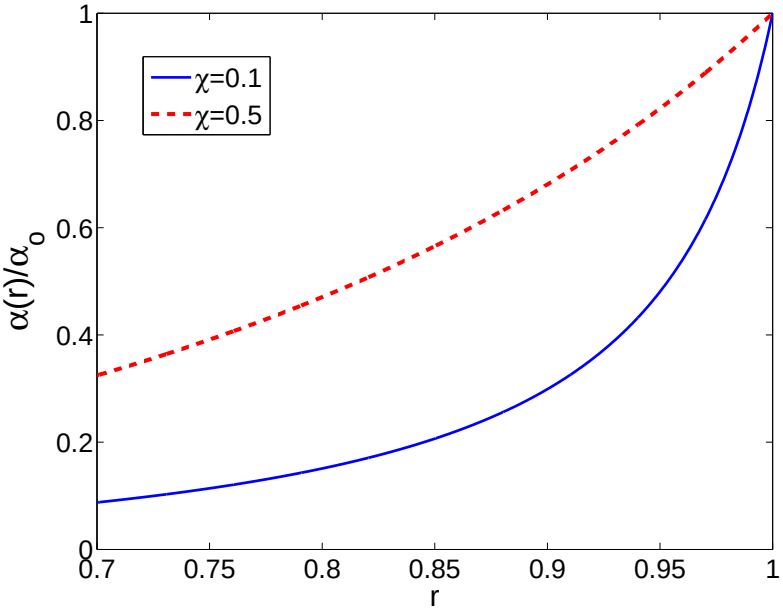

Figure 2.5: The dependence of $\alpha(r)$ on χ in Model B.

We now compare the convective dynamics of the Model A and B setups in order to try and understand the respective roles of $\mathrm{Ra}(r)$ and $\beta(r)$ in driving convection and mixing. To do so, we have run numerical simulations using Model B for three different values of χ, for a fixed $\mathrm{Ra}(r) = \mathrm{Ra}_o = 10^7$. In these constant Rayleigh function runs, we were able to achieve values of χ down to 0.001.

Figure 2.3 compares the energetics of Model A (solid lines with markers) and Model B (dashed lines with markers) runs. In Figure 2.3(a), we observe that the saturation level of the kinetic energy per unit volume E_k varies much less with χ in Model B than in Model A. This might be expected since both Ra and Pr are now constant at all radii and in all configurations of Model B presented. In Figure 2.3(b), we see that the kinetic energy profiles $\bar{E}_k(r)$ of the various Model B runs almost coincide in the bulk of the convection zone, showing that β alone does not influence this quantity much.

Figure 2.6 shows the mean kinetic energy E (i.e. the time average of E_k) against the bulk Rayleigh number defined as

$$\mathrm{Ra}_b = \frac{\int_{r_i}^{r_o} \mathrm{Ra}(r) r^2 dr}{\int_{r_i}^{r_o} r^2 dr}. \tag{2.22}$$

We see that the mean kinetic energy depends solely on the bulk Rayleigh number (for fixed Pr and $r_o - r_i$) and not on the setup used or on the value of χ. This is a very interesting finding, since it illustrates that the mean kinetic energy is model-independent and can be predicted as long as the bulk Rayleigh number Ra_b of the problem is known. Fitting the available data, we find that $E = (3.7 \pm 2.6)\mathrm{Ra}_b{}^{0.72\pm0.04}$. Note that we expect the exponent to be universal, but, the prefactor likely depends on Pr or on $(r_o - r_i)$.

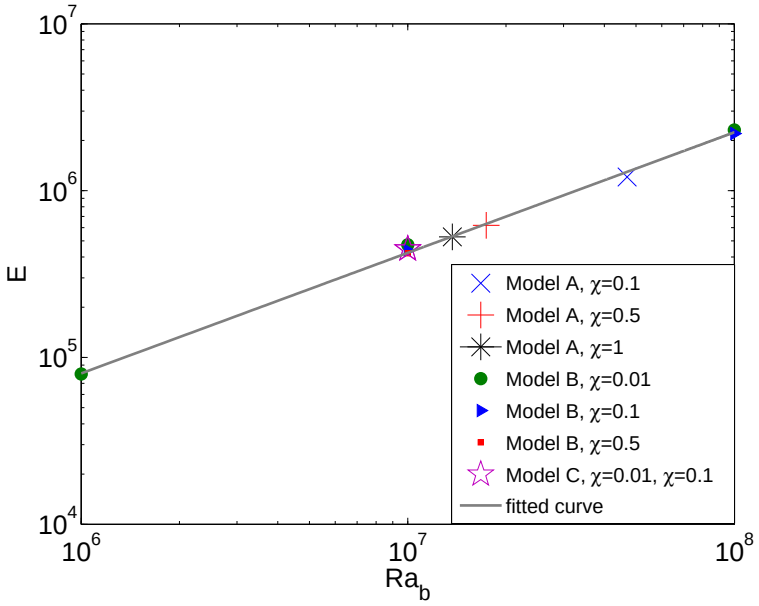

Figure 2.6: Mean kinetic energy E versus bulk Rayleigh number Ra_b for all the Models. Configurations with the same bulk Rayleigh number have approximately the same kinetic energy. The straight line is a fit to the data, with $E = (3.7 \pm 2.6)\mathrm{Ra}_b{}^{0.72\pm0.04}$.

In order to compare the efficiency of mixing in this new system, we again look at the square of the non-dimensional buoyancy frequency, defined for Model B as

$$\bar{N}^2(r) = \frac{\alpha(r)}{\alpha_o}\left(\beta(r) + \frac{d\bar{\Theta}}{dr}\right)\frac{\mathrm{Ra}_o}{\mathrm{Pr}}. \tag{2.23}$$

In Figure 2.7, we plot $\bar{N}^2(r)\mathrm{Pr}/\mathrm{Ra}_o$ compared with the background $N^2_{\mathrm{rad}}\mathrm{Pr}/\mathrm{Ra}_o = (\alpha(r)/\alpha_o)\beta(r)$ for Model B. Note that by construction in this setup $N^2_{\mathrm{rad}}\mathrm{Pr}/\mathrm{Ra}_o = -1$ regardless of χ. We see that as χ decreases, $\bar{N}^2$ increases and for $\chi \leq 0.1$ a subadiabatic region does indeed emerge as in Model A. This unusual effect is much more pronounced at $\chi = 0.01$. Overall, this conclusively shows that the appearance of the subadiabatic region is not model-dependent, but instead, a fairly generic property of simulations that combine mixed temperature boundary conditions with varying superadiabaticity.

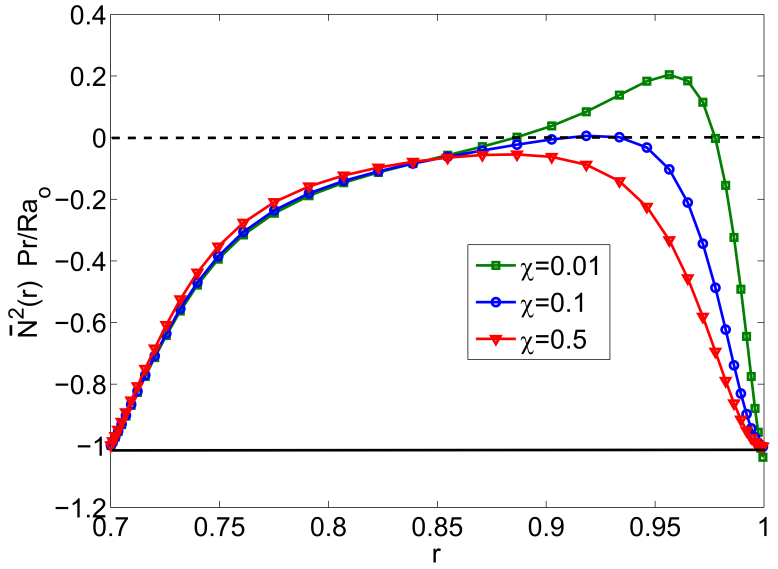

Figure 2.7: $\bar{N}^2(r)\mathrm{Pr}/\mathrm{Ra}_o$ profile compared with $N^2_{\mathrm{rad}}(r)\mathrm{Pr}/\mathrm{Ra}_o \equiv -1$ (solid black line) for different values of χ and $\mathrm{Ra}_o = 10^7$ (all runs are using Model B). Note how the subadiabatic region becomes much more pronounced for lower χ.

In order to determine more precisely how the emergence of a subadiabatic region depends on the model parameters, we ran additional simulations at $\mathrm{Ra}_o = 10^6$ and $\mathrm{Ra}_o = 10^8$ for $\chi = 0.01$, as well as a simulation with $\mathrm{Ra}_o = 10^8$ for $\chi = 0.1$. Figure 2.8 shows the square of the buoyancy frequency profiles for these comparative runs. We observe that, for a given value of χ, there is a threshold value of Ra_o above which the subadiabatic region appears, and that the size and subadiabaticity of that region increases with Ra_o beyond that threshold. For fixed Ra_o we see a similar behavior with decreasing χ. These considerations suggest that the subadiabatic layer appears only for sufficiently vigorous convection (high Rayleigh number) and/or in systems with sufficiently large radial variations in the background superadiabaticity (here generated by low χ).

Interestingly, convection appears unaffected by the emergence of the subadiabatic layer, and proceeds as if it did not exist. This can be seen both in snapshots

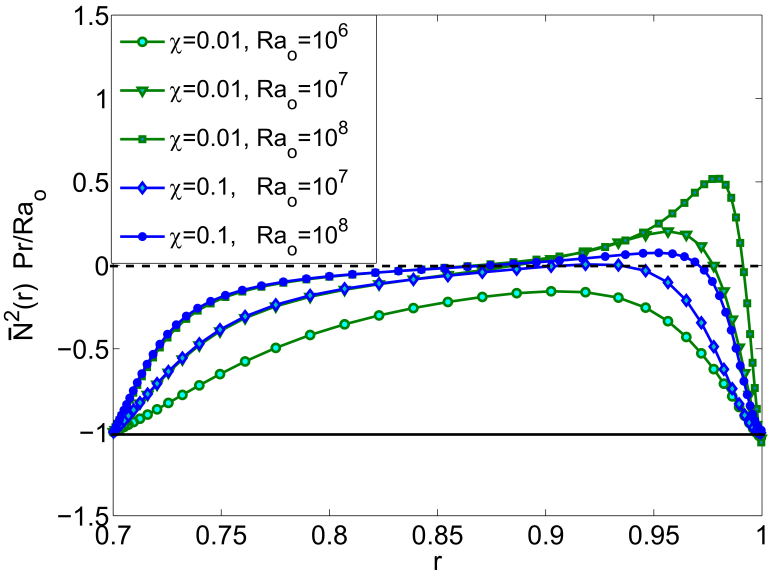

Figure 2.8: $\bar{N}^2(r)\mathrm{Pr}/\mathrm{Ra}_o$ profile for Model B for different values of χ and Ra_o. The solid black line indicates the background $N^2_{\mathrm{rad}}(r)\mathrm{Pr}/\mathrm{Ra}_o = -1$.

of the velocity field (Figure 2.9) and in the kinetic energy profiles as a function of radius (Figure 2.10). Figure 2.9 shows snapshots of u_ϕ as a function of radius and latitude, for a fixed longitude, for $\chi = 0.01$ and the three different Rayleigh numbers used in that case. As the Rayleigh number increases, the convective eddies are more pronounced and the turbulent motions are apparently stronger. However, none of the simulations show any obvious indication of a non-convective or "dead" zone due to the subadiabatic layer (which is present for the $\mathrm{Ra}_o = 10^7$ and $\mathrm{Ra}_o = 10^8$ cases). The same can be seen more quantitatively in Figure 2.10, which shows the kinetic energy profiles for the same three cases ($\mathrm{Ra}_o = 10^6$, 10^7 and 10^8, and $\chi = 0.01$). As in Model A, we find that they have roughly the same shape, but that the kinetic energy increases with Ra_o. Crucially, there is no sign of any dip in the kinetic energy profiles at the locations of the subadiabatic layers in the $\mathrm{Ra}_o = 10^7$ and $\mathrm{Ra}_o = 10^8$ runs, which proves that convection is efficient everywhere across the shell. All the above provide strong indications that

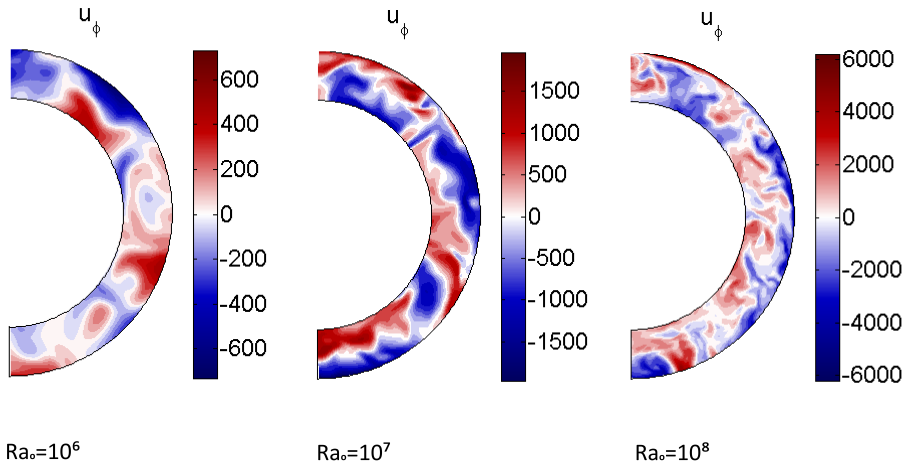

Figure 2.9: Snapshots of u_ϕ in a selected meridional slice for Model B when $\chi = 0.01$ and for three different Ra_o. As we increase the Rayleigh number, the convective eddies are more pronounced and the turbulent motions are more intense.

convection in these models is a very non-local process.

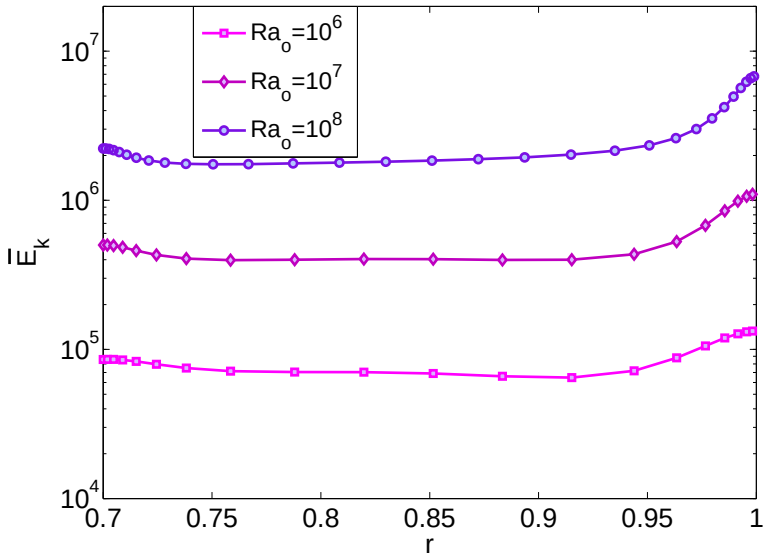

Figure 2.10: Time-averaged kinetic energy profile $\bar{E}_k(r)$ for Model B, $\chi = 0.01$, and for three different values of Ra_o.

2.4 Interpretation of the results

Having established that the emergence of a subadiabatic layer is a robust phenomenon in these models, we now proceed to explain the observed dynamics more quantitatively. As we shall demonstrate, the phenomenon is directly related to the use of mixed temperature boundary conditions, and is facilitated by the presence of a strongly-varying background superadiabaticity.

The above results are implicitly related to the choice of mixed boundary conditions for Θ. The fixed flux at the inner boundary is a source of strong asymmetry in the dynamics of the problem since it allows the temperature perturbations Θ to be negative there. In a system with fixed temperature conditions on the other hand, Θ and therefore $\bar{\Theta}$ would be forced to be zero at both bottom and top boundaries, and the system would be much more symmetric (though not perfectly because of the sphericity and the non-zero constant adiabatic temperature gradient which are additional sources of asymmetry).

The use of mixed boundary conditions has a second very important impact on the convective dynamics, namely that the total perturbed temperature flux through the system (turbulent + diffusive) must be equal to that at the inner boundary, and thus zero everywhere (Fig. 2.11). Non-dimensionally, this is expressed as

$$\bar{F}_h - \frac{1}{\mathrm{Pr}} \frac{d\bar{\Theta}}{dr} = 0. \tag{2.24}$$

In thermal equilibrium, the diffusive and non-diffusive contributions to the perturbed temperature flux must therefore cancel out exactly. The magnitude of the temperature perturbations depends on χ (through the increasingly negative values of Θ_{ad} as $\beta(r)$ decreases rapidly with r for low χ, where Θ_{ad} is the temperature that a downflow traveling adiabatically from the surface (where $\Theta = 0$)

would have as a function of r, i.e. $\Theta_{\rm ad}(r) = -\int_{r_o}^{r} \beta(r')dr'$). Furthermore, the rms velocity of the convective eddies increases substantially with Ra_o (see Figure 2.6). Thus for low χ and high Ra_o, the turbulent flux increases and the diffusive flux of the temperature perturbations must follow accordingly. This is crucial, and causes the emergence of the subadiabatic layer in our simulations as follows. Using Equation (2.24) we can re-write $\bar{N}^2$ as

$$\bar{N}^2(r) = \frac{\alpha(r)}{\alpha_o}(\beta(r) + \mathrm{Pr}\bar{F}_h)\frac{\mathrm{Ra_o}}{\mathrm{Pr}}, \tag{2.25}$$

where we carefully note that $\beta(r) < 0$ while $\bar{F}_h > 0$. Since $\bar{F}_h$ increases monotonically with increasing Ra_o (because of the increase in u_{rms}) or decreasing χ (because Θ_{rms} is larger), there exists a region of parameter space where $(\beta(r) + \mathrm{Pr}\bar{F}_h)$ becomes positive, at least somewhere within the shell, leading to a positive $\bar{N}^2(r)$.

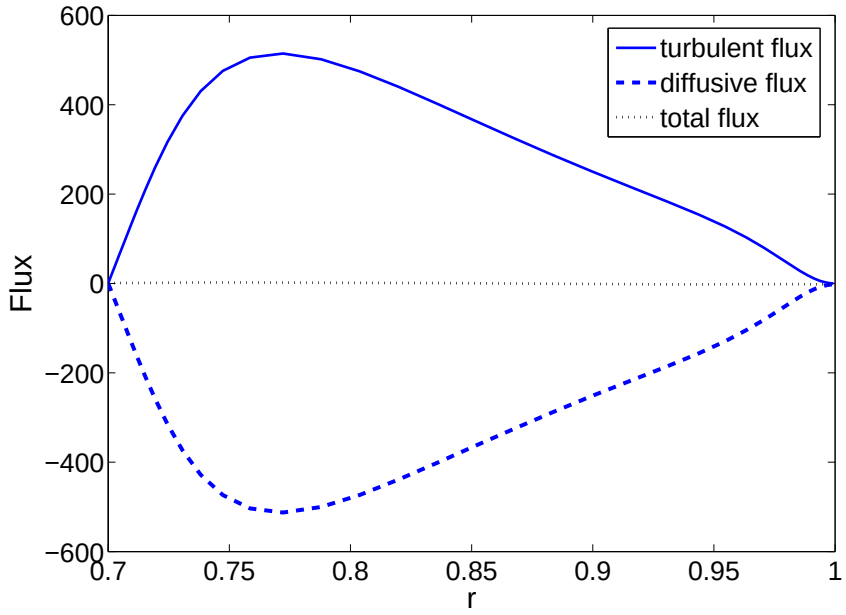

Figure 2.11: The time- and spherically- averaged turbulent and diffusive contributions to the perturbed temperature flux and their sum, for a Model B run with $\chi = 0.01$ and $\mathrm{Ra}_o = 10^7$.

Using the results we have obtained so far, we can in fact provide an order-of-magnitude estimate for $\bar{F}_h$ as a function of χ and of the bulk Rayleigh number Ra_b given in (2.22). The typical amplitude of the temperature perturbations Θ_{rms} can be estimated from Θ_{ad}, which is proportional to $1/\chi$ for low enough χ . The rms velocity of the flow u_{rms} can be estimated from Ra_b using $u_{rms} = \sqrt{2E}$. In Section 2.3, we found that $E = (3.7 \pm 2.6)\mathrm{Ra}_b{}^{0.72\pm0.04}$, so u_{rms} approximately scales as $\mathrm{Ra}_b{}^{0.36}$. Combining these two estimates suggests that the turbulent temperature flux should scale as $\mathrm{Ra}_b{}^{0.36}/\chi$ for low enough χ. In Figure 2.12, we plot $\bar{F}_h\chi/\mathrm{Ra}_b^{0.36}$ versus r for Model B runs at $\mathrm{Ra}_o = 10^7$ and for four different values of χ. The predicted scaling seems to work well for $\chi \leq 0.1$. We conclude that the emergence of a subadiabatic layer is a generic result which occurs for large bulk Rayleigh numbers and/or low values of χ, as we have found in our simulations. Note that the scaling $\bar{F}_h \sim \mathrm{Ra}_b{}^{0.36}/\chi$ suggests that the subadiabatic layer could in fact appear even when $\chi = 1$ provided Ra_b is large enough. In that sense, it might even be realized in the limit of a Cartesian RBC system as long as mixed thermal boundary conditions are used, though the Rayleigh number may need to be extremely large in that limit to exhibit the desired dynamics.

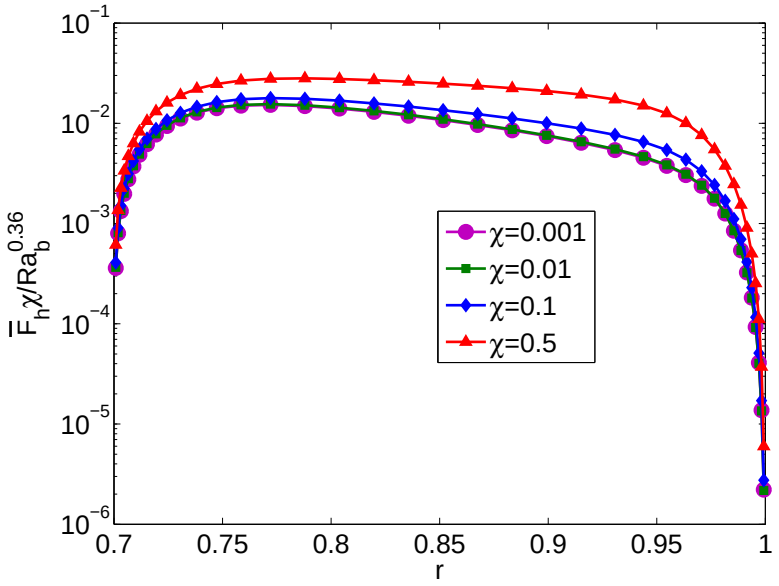

Figure 2.12: $\bar{F}_h\chi/\mathrm{Ra}_b^{0.36}$ for Model B, $\chi = 0.001$, $\chi = 0.01$, $\chi = 0.1$ and $\chi = 0.5$, and $\mathrm{Ra}_b = 10^7$.

2.5 A more solar $\beta(r)$ profile: Setup and numerical results

Until now we have used a profile for $\beta(r)$ dictated by the geometry and the boundary conditions of our model setup. To see whether our findings have any bearing on the dynamics of convection in stars, we now compute the equivalent $\beta(r)$ profile from a standard solar model (Model S, [36]). To do so, we evaluate the difference between $dT_{\mathrm{rad}}/dr = -3\kappa\rho L/(64\pi r^2\sigma T^3)$ (where the Model S is used to extract the density ρ, the luminosity L, the temperature T, and the opacity κ, and where σ is the Stefan-Boltzmann constant), and the adiabatic temperature gradient $dT_{\mathrm{ad}}/dr = -g/c_p$. The results are shown in Figure 2.13. We see that, by contrast with the models we have been using so far, $|\beta|$ *decreases* inwards instead of increasing inwards.

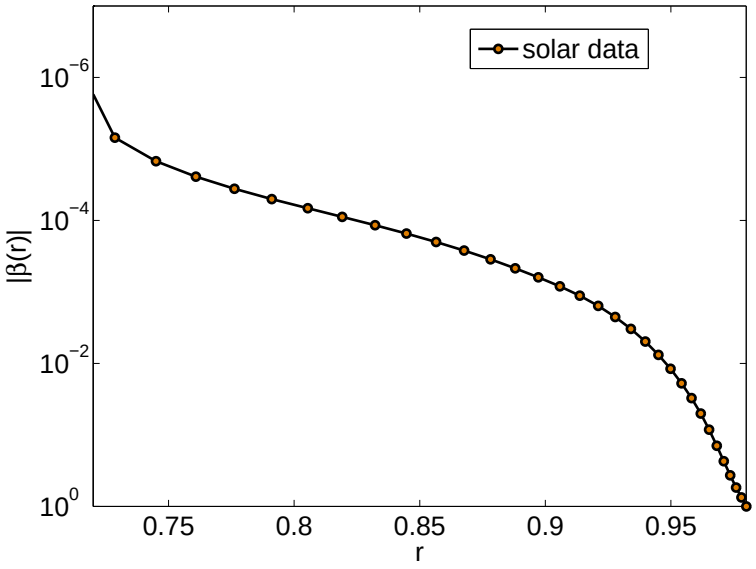

Figure 2.13: The function $|\beta(r)|$ according to Model S [36].

In the light of this information, we conduct a final set of numerical experiments where we construct a more solar-like profile for $\beta(r)$ choosing $\beta(r) = \chi/(1 - \chi - (1/r^2))$ in order to ensure that $|\beta(r)|$ decreases inward, and letting $\alpha(r)/\alpha_o = -1/\beta(r)$ as before to have $\mathrm{Ra}(r) = \mathrm{Ra}_o$. Note that in this model, χ does not have the same physical meaning as in Equation (2.15), but it is merely used as a parameter to describe a family of functions $\beta(r)$ with a "solar-like" profile. Figure 2.14 illustrates the $\beta(r)$ functions thus created for two different values of χ. Note that β lies in the range (0,1] but crucially the ratio of the inner to outer values is large and approximately equal to 11 for $\chi = 0.1$ and 105 for $\chi = 0.01$.

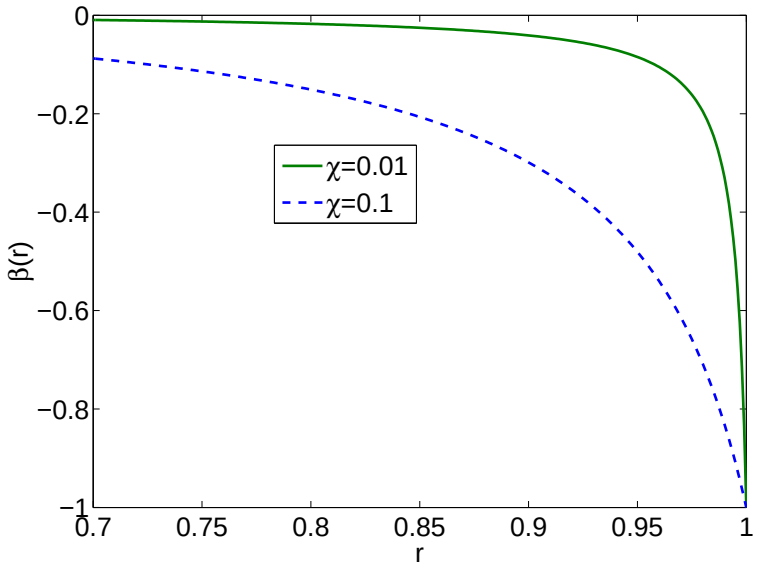

Figure 2.14: The different $\beta(r)$ profiles for $\chi = 0.01$ and $\chi = 0.1$ for Model C.

We have run two simulations, for two different values of χ ($\chi = 0.01$ and $\chi = 0.1$) at $\mathrm{Ra}_o = 10^7$. In the previous models, these cases led to the emergence of a subadiabatic region close to the outer boundary of the convection zone. Looking at the square of the non-dimensional buoyancy frequency profile for this model (Fig. 2.15), we observe that a slightly subadiabatic region does indeed appear, this time close to the inner boundary of the convection zone.

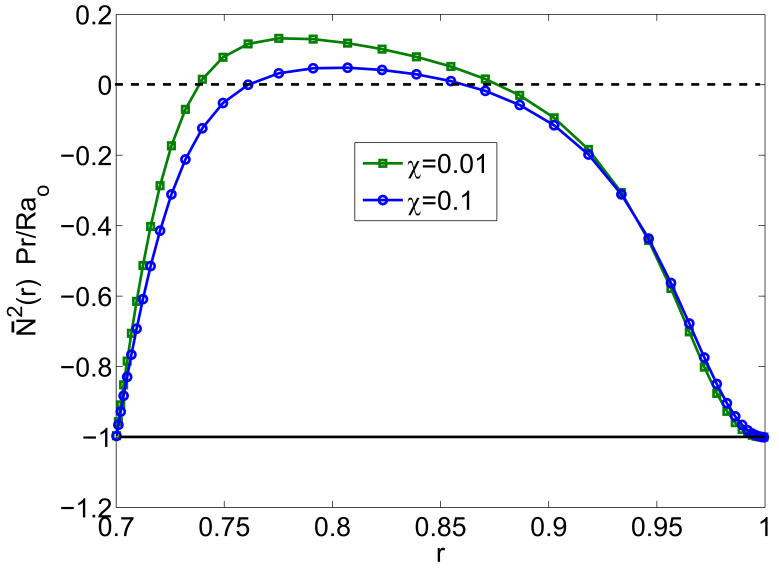

Figure 2.15: The square of the buoyancy frequency for Model C, for two different values of χ, and for $\mathrm{Ra}_o = 10^7$.

Note that the general mechanism for the appearance of this layer is the same as before, although the quantitative details differ. In this model setup, the mean kinetic energy is again controlled only by the bulk Rayleigh number (see Fig. 2.6), hence the velocity fluctuations remain large. However because $\beta(r)$ varies between 0 and 1 the typical amplitude of the temperature perturbations Θ_{rms} is much smaller (i.e. this time $\Theta_{rms} \propto \chi$). This results in a much smaller total turbulent temperature flux $\bar{F}_h$ compared with Models A and B. As shown in Equation (2.25), however, whether a subadiabatic layer appears or not depends on the *relative* amplitude of $\bar{F}_h$ compared to $\beta(r)$. Since $\beta(r)$ is close to 0 near the inner boundary, a small turbulent temperature flux is indeed sufficient to create a subadiabatic layer there according to Eq. (2.24).

Figure 2.16 shows a snapshot of u_r for the $\chi = 0.01$ case, in which the subadiabatic region is the deepest observed so far. Notice that convection is still vigorous throughout, again supporting our conclusions from previous models that this type

of convection is highly non-local.

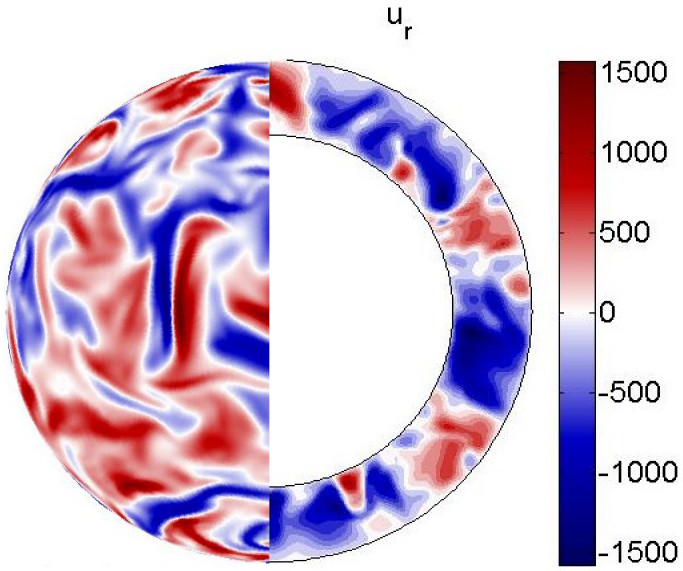

Figure 2.16: Snapshot of the radial velocity u_r for $\chi = 0.01$ and $\mathrm{Ra}_o = 10^7$ for Model C. The left part shows the u_r field close to the outer radius just below the boundary layer. The right part shows the same field u_r on a selected meridional plane.

2.6 Discussion

We have studied convection in a weakly compressible gaseous spherical shell, assuming a constant adiabatic temperature gradient as well as mixed temperature boundary conditions (fixed flux at the inner boundary and fixed temperature at the outer boundary). In Sections 2.2, 2.3 and 2.5, we presented results from three different model setups, that all have the same remarkable properties for sufficiently large Rayleigh number Ra, and sufficiently large variations in the superadiabaticity across the shell (measured by χ). All these simulations showed the emergence of a subadiabatic layer which is still fully mixed by non-local convection. In Section 2.4, we explained these findings as follows:

Emergence of a subadiabatic layer: The fixed flux boundary condition at the inner boundary has an important consequence, namely that of tying the turbulent temperature flux to the perturbed diffusive temperature flux. Hence, for sufficiently large turbulent temperature flux, the diffusive temperature flux must also become large and can cause the background temperature gradient to exceed the adiabatic one, which results in a subadiabatic stratification.

Two natural questions hence arise: What are the minimal necessary conditions for these dynamics to manifest themselves and why have these never been reported before in other Boussinesq studies? As an answer to the first question, we argue that the necessary conditions are (1) mixed temperature boundary conditions with fixed flux at one boundary and fixed temperature at the other, and (2) sufficiently turbulent flows. The importance of (1) should be clear from the description above. Condition (2) is necessary for the turbulent fluxes to be large enough and for inertia to be strong enough. These conditions are necessary, but do not have to be met necessarily in exactly the same way they are created as in Models A, B or C. For instance, we believe that with a sufficiently deep shell, it may be possible to achieve this dynamical regime even if χ were closer to one. Although not a strictly necessary condition, we have also found that having a radially-varying superadiabaticity $\beta(r)$ more easily creates a large enough contrast across the domain and therefore lowers the threshold in Ra for the emergence of the subadiabatic layer. As such, it might even be possible to be in this unusual regime in a strictly Boussinesq Cartesian RBC, though the Rayleigh number may need to be extremely high, or one may need to invoke additional non-Boussinesq effects to generate a rapidly-varying β and the therefore significant β contrast (such as varying gravity, for example, which causes a varying $dT_{\rm ad}/dz$, or by varying the diffusivities, or by adding internal heat sources within the fluid). By this

reasoning, we conjecture that these dynamics may be found in high Pr number convection for large enough Ra.

Given these necessary conditions, we can now easily answer the second question. This kind of convection has not been previously observed in other Boussinesq studies because the vast majority of investigations to date have used fixed temperature boundary conditions or fixed flux at both boundaries (e.g. [108, 80]). There are certain studies in which mixed temperature boundary conditions have been implemented, notably in [62]. There, low and intermediate Ra were investigated, with a Prandtl number equal to one and the flows were likely insufficiently turbulent (see condition 2) for the subadiabatic layer to appear. In Verzicco & Sreenivasan (2008) [155] (see also [137]), turbulent convection in the high Ra regime using fixed flux at the bottom and fixed temperature at the top was also studied but there was no report of any subadiabatic layer. They also noticed that the plumes were less buoyant and cooler and as a result carried less heat compared with cases where the temperature was fixed at both boundaries. In both cases however, the fluid was incompressible with $dT_{\rm ad}/dz = 0$ and $dT_{\rm rad}/dz$ constant, so that $\beta(z) = -1$ and there was much less imposed asymmetry in their system. Hence, although some prior studies have considered the effects of mixed temperature boundary conditions, ours appears to be the first to report the emergence of a subadiabatic layer. That implies that a combination of both conditions described above has to be satisfied.

Finally, it is important to recall that we have used the SVB approximation for weakly compressible gases even though our model setups do not necessarily satisfy all the requirements of this approximation. Indeed, the two fundamental assumptions entering the SVB approximation are: 1) that any perturbations of the thermodynamic quantities ρ and T about their domain mean ρ_m and T_m

should be small, and 2) that the flow velocities be much smaller than the sound speed. These approximations then justify the use of equations (5) to (7). Note that SV also used a Cartesian domain, and further assumed, for simplicity, that α, g, κ and ν, as well as the radiative and adiabatic temperature gradients were constant, but these are not necessary conditions for the applicability of their equations. However, in a spherical geometry, or if these quantities vary with depth (as in our own models), one should verify that both the background state and the perturbations continue to satisfy conditions (1) and (2) a posteriori. In Model A, as discussed in Section 2.2, the sphericity of the domain implies that $T_{\rm rad}$ must vary with depth, even if everything else is held constant. As such, the SVB approximation can only be used if $\Delta T \ll T_m$, or equivalently, if $F_{\rm rad}(r_i^2/\kappa)(\frac{1}{r_i} - \frac{1}{r_o}) \ll T_m$. To satisfy this condition and maintain a large Rayleigh number at the same time can be achieved by letting $\nu \to 0$ for instance. In Model B on the other hand, the validity of the SVB approximation is definitely violated, as $\alpha(r)$ varies quite significantly across the domain when χ is small. This invalidates the linearization of the equation of state used. A similar statement applies to Model C.

One may therefore rightfully question whether the new dynamics discovered here are artifacts associated with breaking the bounds of validity of the SVB equations, or whether they would indeed occur in a more realistic, fully compressible model setup as well. Based on published work and our own unpublished recent findings, the latter statement is likely true. Indeed, Chan & Gigas (1992) [29], reported the emergence of a subadiabatic layer close to the outer boundary of 3D, large-eddy simulations of compressible convection in an effectively plane parallel domain. However the resolution used was very low, shedding doubt at the time on the robustness of their results. Other studies have also noted the appearance

of a subadiabatic mixed region in compressible hydrodynamic simulations (e.g. [99, 75]) but the setup in these cases was not based purely on a convection zone, but rather, on a convection zone embedded in between two stable regions. Recently, Käpylä et al. (2017) [82] also reported a subadiabatic layer in their fully compressible 3D simulations of overshooting convection. Nevertheless, a complete and definitive answer to this question requires the solution of the fully compressible equations, which is the subject of a future publication. Preliminary results obtained by the authors with 3D fully compressible DNSs in a Cartesian box with mixed temperature boundary conditions do indeed show the appearance of a subadiabatic region, suggesting that the most salient feature of this kind of convection is robust (Brummell et al., in prep.). We, however, expect the details to differ substantially, since the SVB approximation inherently suppresses some essential compressible dynamics, in particular the dynamic role of pressure in compressional heating.

Model	χ	Ra_o	N_r	N_θ	N_ϕ	L_{max}	M_{max}
A	0.1	10^7	250	402	480	268	134
A	0.5	10^7	220	346	384	230	120
A	1	10^7	220	346	384	230	120
B	0.001	10^7	200	288	320	192	96
B	0.01	10^6	200	192	192	128	64
B	0.01	10^7	200	288	320	192	96
B	0.01	10^8	300	516	640	344	172
B	0.1	10^7	200	288	320	192	96
B	0.1	10^8	300	516	640	344	172
B	0.5	10^7	200	288	320	192	96
C	0.01	10^7	200	288	320	192	96
C	0.1	10^7	200	288	320	192	96

Table 2.1: Table with all the different model configurations and the input parameters used in each case. The resolution is provided both in number of equivalent meshpoints N_r, N_θ, N_ϕ, as well as in the number of spherical harmonics used in the horizontal directions, L_{max} and M_{max}.

Chapter 3

Convective overshooting and penetration in a Boussinesq spherical shell

The following chapter is composed of the work submitted to Monthly Notices of the Royal Astronomical Society in July 2018. The co-authors of this paper are Pascale Garaud and Nicholas Brummell, both professors in the Department of Applied Mathematics at the University of California, Santa Cruz.

3.1 Introduction

Understanding the dynamical interaction between an unstable turbulent convective region and an adjacent stable one remains a long-standing unsolved problem in fluid dynamics. This situation is nevertheless fairly ubiquitous in both geophysical and astrophysical settings. Here on Earth for example, it commonly occurs in the atmosphere, where re-radiance of solar surface warming creates a mixed layer below the very stable nocturnal inversion layer [44]. In stars, which

are the main topic of this chapter, the coexistence of convective and radiative layers is almost ubiquitous across masses and evolutionary stages. For example, A-type stars possess two convection zones, an upper one driven predominantly by the ionization of hydrogen and a lower one driven by the second ionization of helium, with a radiative zone in between. In the Sun, by contrast, an outer convection zone sits atop an inner radiative zone and below a stable atmosphere, and the transitions are due to changes in the heat capacity (caused by the partial ionization zones of hydrogen and helium) and opacity (due to the temperature dependence of heavier ions). Since there is no impermeable interface between the stable and unstable layers, fluid flows originating from one can continue into the other. Primary questions are then whether the convective region can be extended from its original size, and whether the stability characteristics of the system are altered significantly. In all that follows, we shall adopt the terminology introduced by Zahn (1991) [160]: if motions are found beyond the convective layer but do not extend its size then the dynamics are termed "overshooting"; if the convective region is extended, the dynamics are called "penetration".

Any form of mixing beyond the classical boundary set by the Schwarzschild criterion could have crucial impacts on stellar evolution and surface abundances through the transport of chemicals and angular momentum (e.g. [138, 135, 3, 112, 74, 7]). The transport of magnetic fields between the two regions has also been suggested as playing a major role in the dynamo process (e.g. [149, 109, 33]). Furthermore, thanks to the development of helio- and asteroseismology, we now have the opportunity to directly measure the extent of an adiabatically stratified zone (e.g. [38, 129]). This provides a direct test of stellar evolution, and can in particular reveal the presence of penetration beyond the expected edge of a convective region (e.g. [45, 37]). Because of its obvious importance, a great body

of work has already been generated on penetrative and overshooting convection, and yet some of the crucial questions remain poorly understood. In what follows, we summarize some of the salient modeling milestones of the field, review any outstanding questions and place our work in their context.

The answer to the most basic question of "does penetration or overshooting actually happen?" has been addressed using a classic example of such dynamics, the ice-water system. Adjacent convective and stable regions in this system can be created thanks to the unusual equation of state for water, which is quadratic with a density maximum at 4° C. When a layer of water sits on top of ice (at 0° C) with an upper boundary temperature of more than 4° C, a system is created where a convectively-unstable layer (between the ice and the location of the density maximum) sits below a convectively-stable layer (above the density maximum). A long history of exploration of this problem exists, from experiments (e.g. [92, 148]), through linear and weakly nonlinear analytic work (e.g. [153]), to numerical simulations both old (e.g. [104, 102]) and new (e.g. [41]). This simple toy model clearly demonstrates that the weak overshooting predicted by linear theory is replaced by deeper penetration when nonlinear feedback on the thermal stratification is allowed. This raises the crucial question of whether similarly large deviations from linear theory predictions (the Schwarzschild criterion) exist in stars.

Answering this question requires moving beyond the assumptions of the works cited above, which were almost all two-dimensional and (essentially) incompressible. A first attempt to understand three-dimensional and compressible effects numerically came from modeling via modal expansions, an approach that is motivated by the observable cellular nature of convection. The horizontal structure of the flow is expanded as a low-order discrete spectrum of horizontal planform

modes, allowing numerical resources to be devoted to solving the vertical and temporal problem. This approach, first introduced by Herring (1963) [73] and Roberts (1966) [118] but popularized in a series of papers by Gough, Spiegel and Toomre [68, 145, 146], was first applied to the Bénard convection problem, and commonly uses severe truncations of the modal expansion (1-3 modes) with planforms such as rolls, squares and hexagons.

The technique has been extended to penetrative and overshooting problems involving multiple layers in a number of ways. Using a complex equation of state to include the ionization regions, as well as the anelastic formalism, the papers by Latour et al. [86, 147, 87] study the convection zones of A-type stars, and find that they could interact despite the intervening radiative zone thanks to extended fluid motions. Somewhat later, Zahn et al. (1982) [161] and Massaguer et al. (1984) [95] simplified the model setup to address the question of penetration specifically. Using Boussinesq and anelastic equations respectively, they initiate layers by directly specifying a depth-dependent background adiabatic gradient, in order to study a single convection zone sandwiched between two stable layers. This compact series of papers has led to some important realizations. Firstly, a fairly deep penetration on the order of the depth of the unstable layer is found in all cases which agrees well with laboratory experiments (although it depends on the stability of the stable layer and on the aspect ratio of the cells). Secondly, flow asymmetries make substantial differences in the amount of overshoot or penetration. For instance, stratification combined with pressure effects (buoyancy braking in the upflows and enhanced driving in the downflows) in the anelastic case causes slower upflows and faster downflows compared to the Boussinesq case, which leads to enhanced downward penetration. Topological asymmetries (as induced by non-Cartesian effects or simply through a particular selection of

horizontal planform) have similarly important impact on the problem.

The discovery of the importance of flow asymmetries on the extent of overshooting and penetration has naturally prompted new investigations into the effect of compressibility. A big step forward was made by Hurlburt et al. [77, 78], with fully nonlinear, compressible, two-dimensional, Cartesian simulations of overshooting/penetrative convection. Note that these two papers also introduce yet another way of creating a radiative/convective system, by using a vertically-varying thermal conductivity profile. This creates a variation in the background radiative temperature gradient in the different layers which can be selected to achieve different stability properties, and the background model ultimately takes the form of stacked polytropes. This setup naturally introduces the concept of "stiffness" S as the ratio of the subadiabaticity of the stable region to the superadiabaticity of the unstable region. Most notably, these papers investigate the dependence of the depth δ of extended motions on the stiffness S, revealing two separate regimes: one associated with penetration ($\delta \propto S^{-1}$) and one with overshoot ($\delta \propto S^{-1/4}$) (more on this topic later). These studies also demonstrate the generation of gravity waves in the stable interior by the overshooting, both in fully compressible simulations (e.g. [77], see also [113]) and in anelastic ones (e.g. [120, 23]). Freytag et al. (1996) [52] performed fully compressible two-dimensional, radiation-hydrodynamics simulations of the narrow convection zones sandwiched between stable layers created by a complex equation of state including ionization found in A-type stars and cool DA white dwarfs. This paper notably finds deep overshooting, attributes the exponential drop off observed in the overshoot velocity to the stable "tail" of the convectively unstable modes excited in the convection zone, and derives a depth-dependent diffusion coefficient to describe the corresponding mixing. This exponential formulation for mixing

by overshooting convection is now commonly used in stellar evolution codes (e.g. [74, 110, 111, 140]).

Three-dimensional simulations of the Cartesian stacked polytropic model became possible in the latter part of the 1990s. Singh et al. (1995) [130], Singh et al. (1998) [131] and Saikia et al. (2000) [123] for instance present a series of low resolution large-eddy-simulations (LES) with sub-grid-scale (SGS) modelling while Muthsam et al. (1995) [105] present low resolution finite-difference models. All of these are fully compressible, and mostly appear to confirm the ideas of the two-dimensional simulations and analysis, including the various aforementioned scalings with the stiffness, S. Somewhat later, however, Brummell et al. (2002) [21] presented a more comprehensive parameter survey performed with high resolution, direct numerical simulations (DNS), including much more turbulent cases and a wider range of S. That work finds only overshooting and no true penetration, even in the parameter regimes where it would be most likely to occur, such as high Rayleigh number, low Prandtl number and low S. Instead, the transition from adiabatic to subadiabatic stratifications is seen to be rather smooth, and takes place across an extended partially mixed region. The authors attribute this mainly to the low filling factor of the downflowing convective plumes in the turbulent compressible case, arguing that the earlier low resolution 3D models only found penetration because they were far more laminar and almost two-dimensional.

In parallel with the predominantly numerical efforts described above, a variety of more phenomenological models have been proposed to date. Early works in stellar evolution typically use a non-local formulation of mixing-length theory (e.g. [132, 127, 40, 91]), with results that vary widely depending on specific assumptions associated with the nonlocal integration scale, as criticized by Renzini

(1987) [116]. As the aforementioned numerical simulations began to provide more insight into the dynamics of overshooting convection, phenomenological models have shifted towards a more realistic representations of the convective flows. In addition to the semi-analytical weakly nonlinear theories discussed earlier, van Ballegooijen (1982) [149] for instance includes the effect of the horizontal flows near the base of the convection zone via linear convective roll modes with an assumed nonlinear saturation amplitude, with similar results to those of the mixing length theory (that only includes vertical motions). Schmitt et al. (1984) [124] builds on the emerging idea that the convective motions are more plume-dominated than cellular by using a meteorological model for plumes in a stable stratification with entrainment [103]; the model formally reduces to the mixing length model of Shaviv & Salpeter (1973) [127] in the limit of zero entrainment. Schmitt et al. (1984) [124] find that shallow penetration is likely in the solar case, with the depth being dependent mainly on the velocity and filling factor of the plumes at the base of the convection zone (and insensitive to other parameters, such as the entrainment rate), and that the transition to radiative dynamics below likely takes place through a very thin thermal adjustment boundary layer.

The work of Zahn (1991) [160] simplifies these ideas by applying scaling arguments to the problem. He separates the dynamics below the convection zone into a true penetrative region (where the motions are vigorous enough to mix the background stratification to adiabatic) and a thermal boundary layer containing overshooting. His model recovers the dependence of the penetration depth on the typical convection zone velocity ($\propto w^{3/2}$) and on the assumed filling factor of the plumes ($\propto f^{1/2}$) found numerically by Schmitt et al. (1984) [124], which is interesting since both models make rather different assumptions on the nature of the plumes. Zahn (1991) [160] also finds that the depth of this layer depends

on the gradient of the conductivity profile, leading to a value of about 50% of a pressure scale height in the solar case. Finally, Zahn's thermal boundary layer is very thin as in Schmitt et al. (1984) [124]. A similar model is used in Hurlburt et al. (1994) [78], but with the smooth conductivity profile replaced by a more abrupt piecewise-constant one corresponding to their stacked polytrope numerical simulations. Writing their predictions for the depth δ of the mixed layers in terms of the stratification (stiffness) ratio, S, they can explain their aforementioned observed scaling laws, namely $\delta \propto S^{-1}$ for true penetration and $\delta \propto S^{-1/4}$ for the thermal boundary (overshoot) layer. They explain the transition in the scalings with increasing S as a tradeoff between the increase in buoyancy braking and the decrease in local Péclet number.

Rempel (2004)[115] builds upon these previous works with a semi-analytical model that follows a distribution of plumes throughout both the convection zone and overshoot region and includes their interaction with the upflows. This model thereby essentially incorporates nonlocality and entrainment, and further allows departures from the parameter regimes where mixing length theory is most likely to work (i.e. towards parameter regimes accessible by numerical simulations). Its predictions mirror the findings of Schmitt et al. (1984) [124] and Zahn (1991) [160] but also reveal the extra dependencies of the overshoot characteristics on the total energy flux (determining the vigor of the eddies in the convection zone) and the assumed degree of mixing by entrainment. In particular, the dependence on the nonlocal convective efficiency is postulated to explain the presence of true penetration in mixing length results (which are necessarily highly turbulent) by contrast with its absence in the three-dimensional simulations (where the degree of turbulence is limited due to numerical issues). Furthermore, this approach demonstrates that an ensemble of plumes with a distribution of velocities behaves

quite differently from one where all the plumes have the same assumed velocity. In particular, the former results in a much smoother thermal transition between the penetration layer and the deeper radiative stratification than the latter, which has important observational implications for helioseismology (e.g [100, 101]).

To summarize, the main robust conclusions of these numerical and phenomenological modeling efforts are that penetration and overshooting can take place down to some fraction of the pressure scale height that depends on the exit velocity and the filling factor (or scale) of the downflowing motions at the base of the convection zone. The velocity of dowflowing plumes depends on the strength of the convection itself in a non-local, bulk sense, requiring high Péclet number for any chance of penetration. Meanwhile the filling factor of these plumes depends on many factors such as geometry (2D vs 3D), compressibility, stratification, and on a turbulent entrainment efficiency that remains poorly constrained. These models also reveal dynamical differences between smooth and abrupt transitions in the background stratification associated with both radiative and adiabatic temperature gradients (e.g. [160, 120]).

Moving forward, the next natural step towards a better understanding of overshooting and penetration should involve three-dimensional simulations in a spherical geometry and some effects of compressibility – either using fully compressible equations or anelastic equations. Although quite a number of simulations of this variety have actually been performed, the vast majority of them have not explicitly examined the penetrative/overshooting question, since they were directed at the global dynamo problem or the solar tachocline problem (for recent efforts, see e.g. [22, 98, 20, 18, 59, 114, 23, 139]). Since such dynamo-directed models require significant turbulence, the considerable expense of these computational efforts has been dedicated to a small number of simulations that are the most

relevant, rather than an exhaustive study of parameter space. Notable exceptions are the work of Browning et al. (2004) [19] and Brun et al. (2017) [24], who look at differential rotation and overshoot in core-convective stars and solar-type stars respectively. In both cases, however, the set of simulations presented are far from actual stellar parameters in terms of actual diffusivities, and vary quantities such as the rotation rate and/or the stellar mass, rather than input parameters that more directly control the strength of the convection and the stratification of the nearby radiative zone. Because of this, the results cannot easily be used to form a prognostic model for overshoot and penetration in more stellar-like conditions.

This chapter therefore presents a parametric survey of stellar-like overshooting convection in a three-dimensional spherical geometry using direct numerical simulations. As a first step towards understanding the full problem, we consider Boussinesq dynamics [133] only, arguing that in many instances the interface between radiative and convective regions is located very deep in the interior of the star where this approximation is appropriate. We also ignore rotation in order to isolate the effects of geometry (asymmetry) and of the model parameters. Our goal is to quantitatively characterize various aspects of the dynamics of the overshoot/penetration zone, in particular, the relationship between the typical velocity of convective eddies and the amount of mixing induced beyond the edge of the original convection zone. Ultimately, we shall answer the question of when one should expect overshoot or true penetration in a star, and provide a usable prescription for mixing by overshooting convection that can easily be incorporated into one-dimensional stellar structure models.

The chapter is organized as follows. In Section 3.2, we describe the model configuration along with the initial conditions and the boundary conditions. In Section 3.3, we present some general characteristics of a canonical simulation and

we describe three characteristic lengthscales. In Section 3.4, we provide a model for the kinetic energy profile below the base of the convection zone. In Section 3.5, we focus on thermal mixing in the radiative zone due to the overshooting of the turbulent motions in the stable region. Finally, in Section 3.6, we summarize our results, provide comparisons with previous numerical work, and discuss the implications of these results in the solar and stellar overshooting dynamics.

3.2 Model setup

We are interested in studying a two-layered system, consisting of a convectively unstable zone (CZ) overlying a radiative zone (RZ) which is everywhere locally stable to convection according to the Schwarzschild criterion. The numerical model used builds upon the purely convective spherical shell setup described in [84], extended to include a convectively stable inner spherical shell beneath the unstable one. Our chosen shell has an outer radius r_o, and inner radius $r_i = 0.2r_o$, with the CZ-RZ interface located at $r_t = 0.7r_o$. This geometry was chosen to mimic that of the Sun, as an example of a fairly typical low-mass star. The position of the inner boundary does not affect any of our results, as long as $r_i \ll r_t$. The selection of the convection zone aspect ratio r_t/r_o is expected to affect the results, on the other hand. However, we have chosen to keep it fixed since there are already many other parameters that need to be varied in the simulations (see below).

In an attempt to be relevant for stellar contexts, we adopt a number of specific dynamical ingredients. We solve the three-dimensional (3D) Navier-Stokes equations under the [133] Boussinesq approximation, which takes into account a non-zero adiabatic temperature gradient to account for weak compressibility. We assume constant thermal expansion coefficient α, viscosity ν, thermal diffusivity

κ, adiabatic temperature gradient $dT_{\rm ad}/dr$ and gravity g. Note that these quantities would of course not be constant over the range $r = [0.2r_o, r_o]$ in a star – this assumption is made for simplicity. We fix the heat flux at the inner boundary, to account for the energy generated from nuclear burning in the stellar core, whereas at the outer boundary we fix the temperature. While the latter does not realistically capture the more complex radiative transfer processes that are known to control the photospheric boundary conditions in solar-type stars, we use this approximation because it is simple, with the expectation that it does not affect the convective dynamics near the bottom of the convection zone. Finally, we perform all of our simulations in a low Prandtl number regime (where the Prandtl number is the ratio of the viscosity to thermal diffusivity), which is again more relevant in the astrophysical context. To the authors' knowledge, this is the first time that penetrative convection is being studied in a Boussinesq spherical shell geometry with the temperature boundary conditions as described above, and in the low Prandtl number regime.

We let $T(r, \theta, \phi, t) = T_{\rm rad}(r) + \Theta(r, \theta, \phi, t)$ where $T_{\rm rad}$ is the temperature profile our system would have under pure radiative equilibrium, and where Θ describes temperature fluctuations away from that radiative equilibrium. As part of the Boussinesq approximation, a linear relationship is assumed between the temperature and density perturbations such that $\rho/\rho_m = -\alpha\Theta$, where ρ_m is the mean density of the background fluid. Then, the governing Boussinesq equations are [133]:

$$\nabla \cdot \boldsymbol{u} = 0, \tag{3.1}$$

$$\frac{\partial \boldsymbol{u}}{\partial t} + \boldsymbol{u} \cdot \nabla \boldsymbol{u} = -\frac{1}{\rho_m}\nabla p + \alpha\Theta g \boldsymbol{e_r} + \nu\nabla^2 \boldsymbol{u}, \tag{3.2}$$

and

$$\frac{\partial \Theta}{\partial t} + \boldsymbol{u} \cdot \nabla \Theta + u_r \left(\frac{dT_{\rm rad}}{dr} - \frac{dT_{\rm ad}}{dr} \right) = \kappa \nabla^2 \Theta, \tag{3.3}$$

where $\boldsymbol{u} = (u_r, u_\theta, u_\phi)$ is the velocity field and p is the pressure perturbation away from hydrostatic equilibrium.

One way to set up the desired two-layered system is by ensuring that $dT_{\rm rad}/dr - dT_{\rm ad}/dr$ is negative in the CZ, and positive in the RZ. Since $T_{\rm rad}$ is the temperature profile at radiative equilibrium, and since we considered that ν and κ are constant, the only way to ensure that its gradient changes significantly (aside from geometric effects) is to assume the existence of a heating source localized near r_t, such that

$$\kappa \nabla^2 T_{\rm rad} = -H_s(r). \tag{3.4}$$

The function $T_{\rm rad}(r)$ is the solution of this equation, with the boundary conditions

$$-\kappa \frac{dT_{\rm rad}}{dr}\bigg|_{r=r_i} = F_{\rm rad}, \tag{3.5}$$

where $F_{\rm rad}$ is the temperature flux per unit area through the inner boundary, and

$$T(r_o) = T_o. \tag{3.6}$$

Integrating Equation (3.4) once yields

$$\kappa \frac{dT_{\rm rad}}{dr} + \left(\frac{r_i}{r} \right)^2 F_{\rm rad} = -\frac{1}{r^2} \int_{r_i}^{r} H_s(r') r'^2 dr', \tag{3.7}$$

showing that we can generate any functional form we desire for $dT_{\rm rad}/dr$ with a suitable choice of $H_s(r)$. Note that in practice (see below), the exact expressions for $H_s(r)$ and $T_{\rm rad}(r)$ are not needed.

We non-dimensionalize the problem by using $[l] = r_o$, $[t] = r_o^2/\nu$, $[u] = \nu/r_o$

and $[T] = |dT_o/dr - dT_{\rm ad}/dr|r_o$ as the unit length, time, velocity and temperature respectively, where $dT_o/dr \equiv dT_{\rm rad}/dr|_{r=r_o}$ is the radiative temperature gradient at the outer boundary. Then, we can write the non-dimensional equations as:

$$\nabla \cdot \boldsymbol{u} = 0, \tag{3.8}$$

$$\frac{\partial \boldsymbol{u}}{\partial t} + \boldsymbol{u} \cdot \nabla \boldsymbol{u} = -\nabla p + \frac{\mathrm{Ra}_o}{\mathrm{Pr}} \Theta \boldsymbol{e_r} + \nabla^2 \boldsymbol{u}, \tag{3.9}$$

and

$$\frac{\partial \Theta}{\partial t} + \boldsymbol{u} \cdot \nabla \Theta + \beta(r) u_r = \frac{1}{\mathrm{Pr}} \nabla^2 \Theta. \tag{3.10}$$

In all that follows, all the variables and parameters are now implicitly non-dimensional. This introduces the Prandtl number Pr and the global Rayleigh Ra_o defined as

$$\mathrm{Pr} = \frac{\nu}{\kappa} \quad \text{and} \quad \mathrm{Ra}_o = \frac{\alpha g \left| \dfrac{dT_o}{dr} - \dfrac{dT_{\rm ad}}{dr} \right| r_o^4}{\kappa \nu}, \tag{3.11}$$

as well as the function $\beta(r)$ which is given by

$$\beta(r) = \frac{\dfrac{dT_{\rm rad}}{dr} - \dfrac{dT_{\rm ad}}{dr}}{\left| \dfrac{dT_o}{dr} - \dfrac{dT_{\rm ad}}{dr} \right|}. \tag{3.12}$$

By suitably selecting $H_s(r)$, and therefore $T_{\rm rad}(r)$, we can create a profile for $\beta(r)$ that results in a convectively stable region for $r_i \leq r < r_t$ and an unstable region for $r_t \leq r \leq r_o$. Here, we choose to impose a function $\beta(r)$ of the form

$$\beta(r) = \begin{cases} -S \tanh\left(\dfrac{r - r_t}{d_{in}}\right) & \text{when } r < r_t, \\ -\tanh\left(\dfrac{r - r_t}{d_{out}}\right) & \text{when } r \geq r_t, \end{cases} \tag{3.13}$$

where d_{in} and d_{out} constrain the width of the imposed radiative-convective bound-

ary, while S is the stiffness parameter which measures the relative stability of the radiative and the convective zones. Note that d_{in} is chosen such that the derivative of $\beta(r)$ is continuous at $r_t = 0.7$, which implies that $d_{in} = Sd_{out}$. The quantity d_{out}^{-1} is the derivative of the function β at $r = r_t$, and therefore describes the steepness of its profile. In this model $\beta(r)$ tends to -1 in the bulk of the convection zone, and to S in the bulk of the radiative zone thereby representing a piecewise constant profile with an adjustable transition. In stars, this is of course not the case, and $\beta(r)$ can vary very significantly within both convective and radiative zones, so this model is chosen for simplicity but with the ability to explore certain questions raised in the introduction related to the effect of the stiffness and the abruptness of the transition. Note that in the Sun, $|\beta(r)|$ decreases substantially from the top to the base of the convection zone (see [84]), the slope of the transition into the radiation zone is rather smooth, and $|\beta(r)|$ in the radiative zone is of the same order as $|\beta|$ in the bulk of the convection zone (which implies that S would be of order unity). The function β can also be expressed as minus the ratio of the local Rayleigh number $\mathrm{Ra}(r)$ to Ra_o, namely

$$\beta(r) = -\frac{\mathrm{Ra(r)}}{\mathrm{Ra}_o}, \tag{3.14}$$

where

$$\mathrm{Ra}(r) = -\frac{\alpha g \left(\frac{dT_{\mathrm{rad}}}{dr} - \frac{dT_{\mathrm{ad}}}{dr} \right) r_o^4}{\kappa\nu}, \tag{3.15}$$

and where the minus sign in Equation (3.15) ensures that $\mathrm{Ra}(r)$ is positive in convective regions. In Figure 3.1, we show representative profiles of $\beta(r)$ in order to demonstrate their dependence on the two parameters S and d_{out}. Higher values of S result in a larger jump in $\beta(r)$ from the base of the CZ inward, while lower values of d_{out} at fixed S lead to a steeper and more sudden transition.

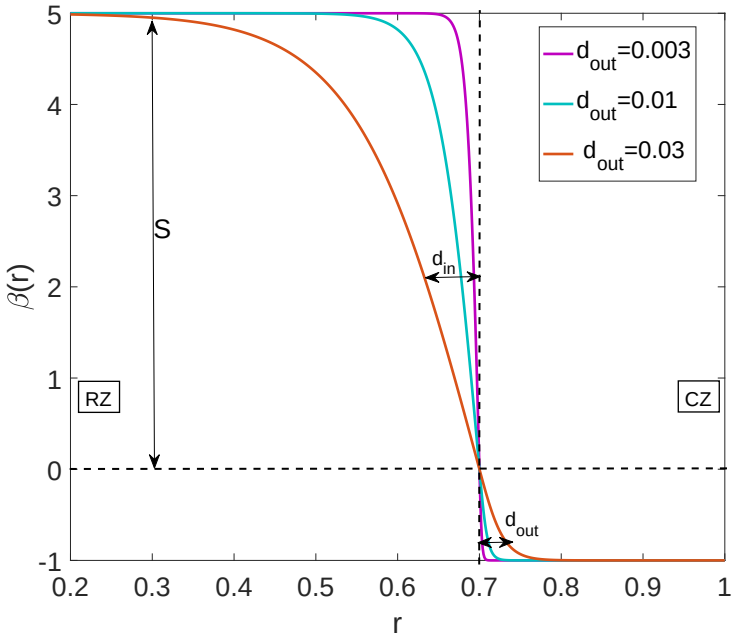

Figure 3.1: The profile of $\beta(r)$ versus the radius r, for $S = 5$ and three different d_{out} values.

In order to study the dynamics of our two-layered system and understand the mixing processes that occur due to the propagation of the convective motions into the stable layer, we have run 3D direct numerical simulations (DNS) solving the Boussinesq equations in a spherical shell, exactly as outlined above, using the PARODY code [46, 4]. In all of our simulations, the Prandtl number is fixed and equal to Pr= 0.1. The boundary conditions for the temperature are such that we have fixed flux at the inner boundary which translates into a no-flux boundary condition for the perturbations Θ, $\partial\Theta/\partial r|_{r_i} = 0$, and fixed temperature at the outer boundary which translates into a zero temperature boundary condition for Θ, $\Theta(r_o) = 0$. For the velocity, we employ stress-free boundary conditions. Each simulation is evolved from a zero initial velocity and small-amplitude perturbations in the temperature field until a statistically stationary and thermally-relaxed state is achieved. To determine when this is the case, we look both at the total

kinetic energy per unit volume in the domain, $E(t) = \frac{1}{2}(u_r^2 + u_\theta^2 + u_\phi^2)$, and at the temperature perturbation gradient at the surface.

We have run a large number of simulations, whose input parameters are summarized in Table 3.1. In Section 3.3, we present an in-depth study of a typical simulation, focusing on identifying measures of the dynamics of overshooting and/or penetrative convection in the vicinity of the CZ-RZ interface. In Sections 3.4 and 3.5 we then look in turn at selected properties of our results across all available simulations.

3.3 General characteristis of a typical simulation

Throughout the chapter, we define the time- and spherical- average of a quantity as

$$\bar{q}(r) = \frac{1}{4\pi(t_2 - t_1)} \int_{t_1}^{t_2} \int_0^{2\pi} \int_0^{\pi} q(r, \theta, \phi, t) \sin\theta d\theta d\phi dt, \tag{3.16}$$

where t_1 and t_2 are an initial and a final time, taken once the system has reached a statistically stationary state. We sometimes choose to present properties of the downflows and upflows separately. Therefore, we also define the average over downflows and upflows only as

$$\bar{q}_{down} = \frac{1}{A_{down}(t_2 - t_1)} \int_{t_1}^{t_2} \int_0^{2\pi} \int_0^{\pi} q(r, \theta, \phi, t) H(-u_r) \sin\theta d\theta d\phi dt, \tag{3.17}$$

$$\bar{q}_{up} = \frac{1}{A_{up}(t_2 - t_1)} \int_{t_1}^{t_2} \int_0^{2\pi} \int_0^{\pi} q(r, \theta, \phi, t) H(u_r) \sin\theta d\theta d\phi dt, \tag{3.18}$$

where H is the Heaviside function, A_{down} is the area covered by the downflows, namely

$$A_{down} = \frac{1}{t_2 - t_1} \int_{t_1}^{t_2} \int_0^{2\pi} \int_0^{\pi} H(-u_r) \sin\theta d\theta d\phi dt, \tag{3.19}$$

and A_{up} is the area of the upflows such that

$$A_{up} = \frac{1}{t_2 - t_1} \int_{t_1}^{t_2} \int_0^{2\pi} \int_0^{\pi} H(u_r) \sin\theta d\theta d\phi dt. \tag{3.20}$$

We begin by presenting the results of a typical run where $S = 5$, $d_{out} = 0.003$, and $\mathrm{Ra}_o = 10^7$ (Case 11 in Table 3.1), which illustrates some of the most basic characteristics observed in almost all of our simulations. Table 3.1 summarizes its input parameters, resolution, and some of the quantities of interest discussed below. The profile of $\beta(r)$ corresponding to these parameters is shown as the purple line in Figure 3.1.

Figure 3.2(a) shows the evolution of the total kinetic energy per unit volume E as a function of time t in the simulation. We observe the initial development of the convective instability in the interval $t \in [0, 0.01]$ as a large spike, followed by its nonlinear saturation. The system reaches a statistically steady state in this global quantity very fast because the energy is dominated by the dynamics of the CZ which rapidly equilibrates. However, we must also make sure that the system reaches global thermal equilibrium. This occurs on a much slower timescale, which depends on the radiative diffusion through the RZ. In our simulations, we estimate that this has occurred when $\partial\Theta/\partial r|_{r=r_o}$ is statistically stationary and close to zero. This happens around $t = 0.02$ in this case.

In Figure 3.3, we present snapshots of meridional slices of the velocity components as a function of depth and latitude, for a selected longitude, all taken at the same time t during the statistically stationary state. They clearly show that

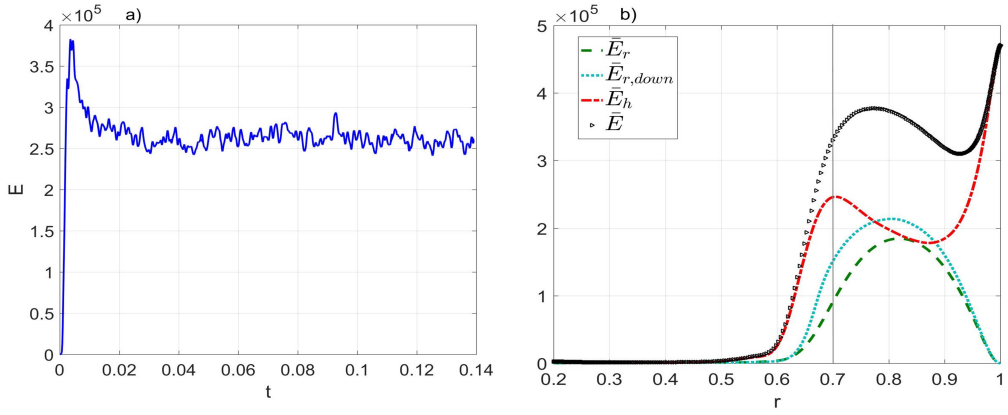

Figure 3.2: *a)* Non-dimensional kinetic energy per unit volume as a function of time for a typical simulation with $S = 5$, $d_{out} = 0.003$ and $\mathrm{Ra}_o = 10^7$. *b)* Time-averaged kinetic energy profiles as a function of radius, for the same simulation.

the convective motions driven within the CZ are not confined to that region, but instead, travel some distance beyond the CZ-RZ interface (marked by the inner black line at $r_t = 0.7$).

As we shall demonstrate, there are many ways in which one can quantitatively study the effect of convective motions which overshoot below the base of the CZ, such as through their kinetic energy, through their effect on the mean temperature profile, as well as through their vertical coherence. Each of these diagnostics presents a different facet of the problem, that we will try to reconcile through modeling in the following Sections.

We begin with Figure 3.2(b) which shows the non-dimensional kinetic energy profile $\bar{E}(r)$ given by

$$\bar{E}(r) = \frac{1}{2}\overline{(u_r^2 + u_\theta^2 + u_\phi^2)}, \tag{3.21}$$

as black triangles. On the same figure, we plot the radial component of the kinetic energy (dashed green line), the vertical kinetic energy of the downflows (dotted cyan line), as well as the horizontal component of the kinetic energy (red line)

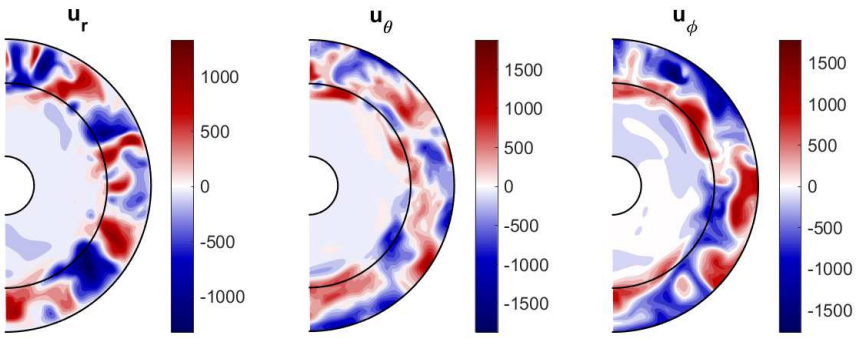

Figure 3.3: Snapshot slice showing the velocities u_r, u_θ and u_ϕ on a selected meridional plane for a typical simulation of $S = 5$, $d_{out} = 0.003$ and $\mathrm{Ra}_o = 10^7$. The inner black line represents the base of the convection zone at r_t.

given respectively by

$$\bar{E}_r(r) = \frac{1}{2}\overline{u_r^2}, \quad \bar{E}_{r,down}(r) = \frac{1}{2}\overline{u_{r,down}^2}, \quad \text{and}$$
$$\bar{E}_h(r) = \frac{1}{2}\overline{(u_\theta^2 + u_\phi^2)}. \tag{3.22}$$

There is clearly significant kinetic energy below the CZ corresponding to overshooting. Below the CZ, the motions are no longer convectively driven and must decelerate. This causes $\bar{E}(r)$ to decrease sharply inward from the base of the convection zone. Furthermore, we see that the contributions to $\bar{E}(r)$ coming from radial and horizontal motions behave very differently from one another. The vertical kinetic energy $\bar{E}_r$ peaks in the middle of the CZ, and then decreases inward, a result we attribute to a deceleration of the downflows as they approach the CZ-RZ interface at $r_t = 0.7$ from above. This can indeed be verified in the profile of $\bar{E}_{r,down}$ which has the same properties, although we also see that it is a lit-

tle larger, indicating that downflows must be on average stronger (but narrower) than the upflows (this can be verified by a direct inspection of A_{up} and A_{down}, not shown). Meanwhile, the horizontal kinetic energy increases substantially near the bottom of the convection zone. Thus, there is an exchange of kinetic energy between the vertical and the horizontal flows, which we interpret as the result of a deflection of the vertical plumes towards the horizontal. While this may seem somewhat expected, it is interesting to see that this occurs in the bulk of the CZ and not only near or below the CZ-RZ interface, implying that the presence of this interface is felt in a highly non-local way throughout the entire convection zone. This result is not an artifact of the Boussinesq approximation, since it is also seen in anelastic and fully compressible 2D simulations (e.g. [120, 113]) and in 3D fully compressible simulations (e.g. [130, 21]).

From the CZ-RZ interface downward, we observe a rapid decrease in $\bar{E}(r)$, which is expected from the stabilizing effect of the stratification. Note that that since the energy in the vertical motions has already decreased significantly even before reaching the CZ-RZ interface, most of the remaining energy below the base of the CZ comes from horizontal motions only. This leads to the conclusion that horizontal motions are dominant in the average sense below the CZ and therefore have to be considered in the study of convective overshooting dynamics, as in the models of e.g. van Ballegooijen (1982) [149] and Rempel (2004) [115].

In Figure 3.4, we plot the total kinetic energy $\bar{E}(r)$ on a log scale to clarify its features below r_t. We see that $\bar{E}(r)$ drops significantly faster than exponentially with depth below the CZ in contrast with the model proposed by Freytag et al. (1996) [52] (also see [74]). In fact, we find that a Gaussian function of the kind

$$f(r) = A \exp\left(-\frac{(r - r_t)^2}{2\delta_G^2}\right) \tag{3.23}$$

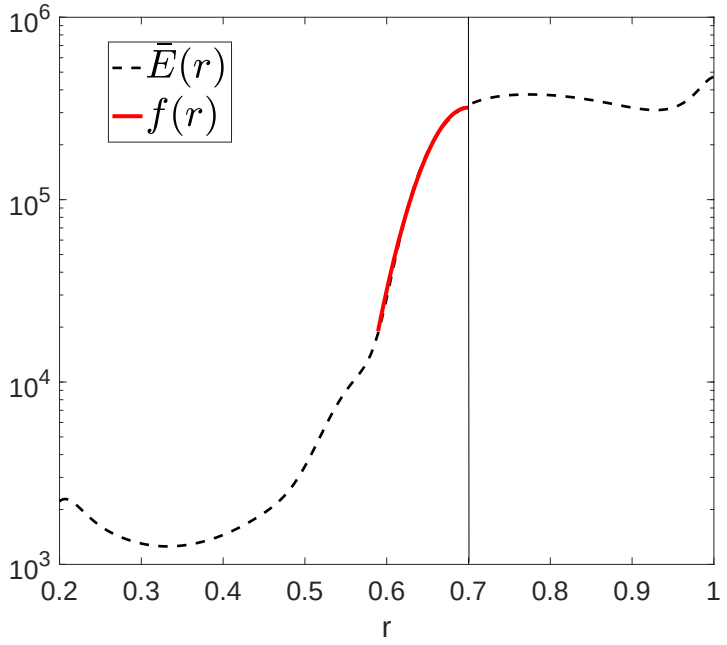

Figure 3.4: Kinetic energy profile $\bar{E}(r)$ for $S = 5$, $d_{out} = 0.003$ and $\mathrm{Ra}_o = 10^7$ against the radius r. The red solid line is the fitted curve of the kinetic energy profile on this interval.

with $\delta_G = 0.047$ would be a much better fit to the profile of $\bar{E}(r)$, at least down to $r = 0.58$, as shown by the red solid line in Fig. 3.4. Below that point, the decay of the kinetic energy is closer to being exponential in the interval $[0.47, 0.58]$. Even deeper down, $\bar{E}(r)$ flattens out, presumably as a result of the presence of the inner boundary. The Gaussian function $f(r)$ can be used to characterize the spherically-averaged kinetic energy profile of overshooting motions below the CZ, and is parametrized by its amplitude A, and by its width δ_G. Therefore δ_G can be used to characterize the region of influence of convective motions in the stable RZ, at least energetically speaking and in an average sense.

An alternative measure is the distance that the strongest of the downflow motions travel into the stable region, therefore, we introduce the radial correlation

function of the vertical velocity field in the downflows

$$C(\delta) = \frac{1}{4\pi(t_2 - t_1)} \int_{t_1}^{t_2} \int_0^{2\pi} \int_0^{\pi} u_r(r_t, \theta, \phi) H(-u_r(r_t, \theta, \phi)) u_r(r_t - \delta, \theta, \phi) \sin\theta d\theta d\phi dt. \tag{3.24}$$

This definition clearly favors the strongest downflows. Figure 3.5 shows $C(\delta)$ for our reference simulation. As expected, C decreases with depth δ below the base of the CZ. Interestingly, we see that instead of merely approaching zero (which would indicate a gradual loss of correlation), $C(\delta)$ actually changes sign (here at $\delta = 0.094$). This implies that (1) the strongest downflows stop, on average, at a well-defined depth below the base of the CZ and that (2) there must be an upflow below each of these downflows. This can only occur if the downflow spreads laterally upon entering the RZ, and the lateral divergence of the fluid acts as a pump for the deeper upflow. This was in fact seen in all of our simulations. We therefore define a second measure of overshooting, the correlation depth δ_u as the first zero of $C(\delta)$. This depth measures the average stopping distance of the strongest downflows. By comparison with Figure 3.4, we see that $r_t - \delta_u$ corresponds to the radius where the kinetic energy switches from the Gaussian to the exponential profile below the CZ as might be expected since a radical change in the dynamics of the fluid is taking place at $r_t - \delta_u$.

By focusing on the fluid motions until this point, we were only able to address the questions pertaining to overshooting rather than penetration. In order to see whether penetration occurs, we must see if substantial thermal (entropy) mixing is occurring. We therefore examine the non-dimensional spherically-averaged buoyancy frequency $\bar{N}$ whose square is given by

$$\bar{N}^2(r) = \alpha g \left(\frac{d\bar{T}}{dr} - \frac{dT_{\rm ad}}{dr} \right) \frac{r_o^4}{\nu^2} = \left(\beta(r) + \frac{d\bar{\Theta}}{dr} \right) \frac{\mathrm{Ra}_o}{\mathrm{Pr}}. \tag{3.25}$$

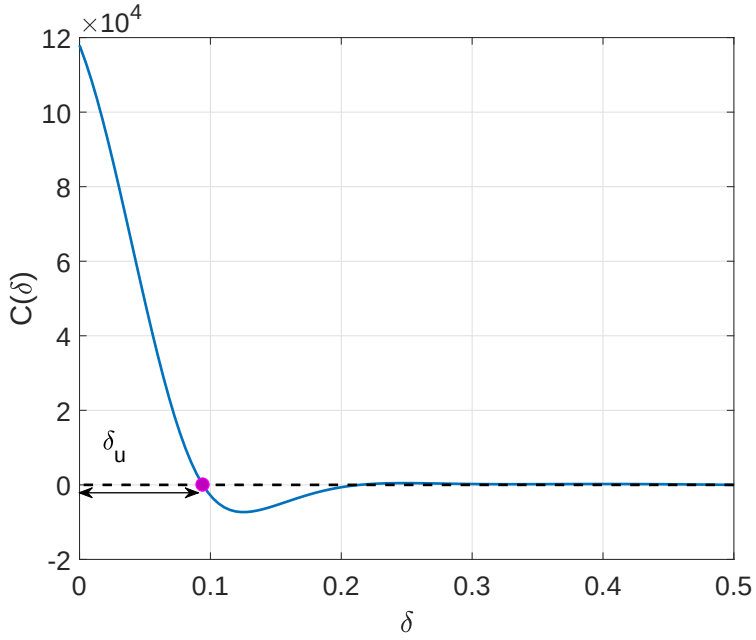

Figure 3.5: Profile of $C(\delta)$ against δ for $S = 5$, $d_{out} = 0.003$, and for $\mathrm{Ra}_o = 10^7$.

Figure 3.6 shows the profile of $\bar{N}^2\mathrm{Pr}/\mathrm{Ra}_o$ measured in our simulations along with the original imposed background profile $N^2_{\mathrm{rad}}(r)\mathrm{Pr}/\mathrm{Ra}_o = \beta(r)$ as a solid line for reference. As expected, the convective motions in the bulk of the CZ (away from both the top boundary and the CZ-RZ interface) mix potential temperature and drive the mean radial temperature gradient towards an adiabatic state where $\bar{N}^2 \approx 0$. Below the CZ, we notice that the fluid motions do affect the thermal stratification, but not strongly enough to effectively extend the region where $\bar{N}^2 \approx 0$. This indicates that there is no penetration (in the strict definition of the term), but also shows that the resultant profile of $\bar{N}^2$ below r_t is much smoother than the originally imposed one. This partially mixed region, which defines an intermediate state that is neither pure penetrative convection nor pure overshooting, was found in nearly all of our simulations and this is investigated in detail in Section 3.5. This result is not entirely surprising. Indeed, the possibility of such an intermediate state was already discussed by Zahn (1991) [160] and Schmitt

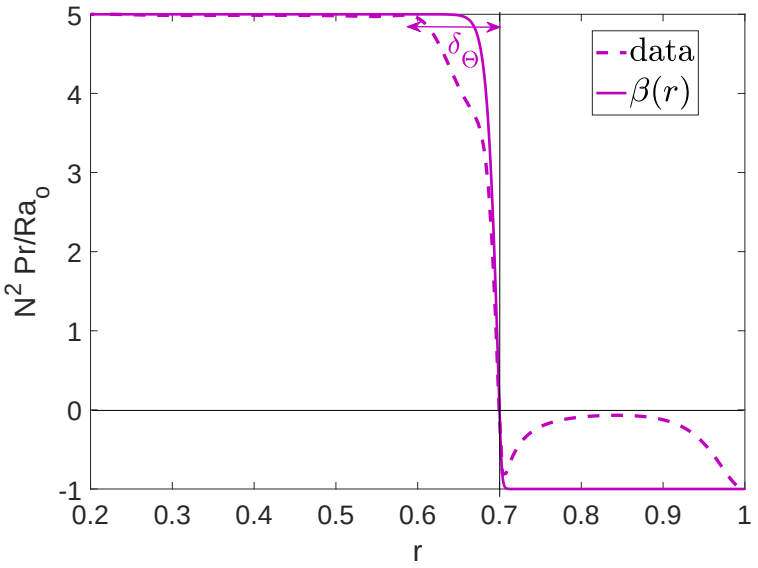

Figure 3.6: Non-dimensional square of the buoyancy frequency $\bar{N}^2\mathrm{Pr}/\mathrm{Ra}_o$ (dashed line) compared with the background $N^2_{\mathrm{rad}}\mathrm{Pr}/\mathrm{Ra}_o$ (solid line) for $S = 5$, $d_{out} = 0.003$, and for $\mathrm{Ra}_o = 10^7$.

et al. (1984) [124] (albeit briefly), and 3D fully compressible simulations to date have reported similar findings (e.g. [21, 82]).

To better understand what might be the cause of this partial mixing, we now look at the details of the thermal transport. Figure 3.7 shows the time- and spherically-averaged temperature perturbations $\bar{\Theta}$ along with the mean temperature perturbation in the upflows ($\bar{\Theta}_{up}$) and downflows ($\bar{\Theta}_{down}$). We also show the temperature that a downflow traveling adiabatically from the surface (where $\Theta = 0$) would have as a function of r, namely $\Theta_{\mathrm{ad}}(r) = -\int_{r_o}^{r} \beta(r')dr'$. We observe that the mean temperature gradient follows the adiabatic one quite closely in the CZ, but that $\bar{\Theta}$ is systematically larger than Θ_{ad} due to the existence of the outer thermal boundary layer. Moreover, we see that $\bar{\Theta}_{down}$ is lower than $\bar{\Theta}$ in the CZ, which is expected since cooler fluid parcels are accelerated downward. Downflowing fluid parcels crossing the base of the CZ into the RZ begin to heat up through adiabatic compression, and become significantly warmer than the mean.

This provides them with an upward acceleration that gradually slows them down. Upflows follow a reverse pattern, where they are warmer than $\bar{\Theta}$ in the CZ, and cooler than $\bar{\Theta}$ in the RZ. Interestingly, we find that $\bar{\Theta}_{down}$ increases by a little just above the base of the CZ, a result that could either be due to nonlinear mixing with the warmer upflows, or, to a diffusive heat flux coming from the much warmer perturbations below the base of the CZ.

We note that there is a point lower in the RZ (here, around $r = 0.6$), at which $\bar{\Theta}$, $\bar{\Theta}_{down}$ and $\bar{\Theta}_{up}$ approximately coincide. We therefore define a new lengthscale δ_Θ which corresponds to the distance of this point from the CZ-RZ interface. Upflows and downflows are neutrally buoyant at $r = r_t - \delta_\Theta$. Below that level, we see that the correlation between the temperature and the direction of the flow becomes much weaker. This then implies that motion must no longer be of convective type and therefore this lengthscale is another measure of where the dynamics change character. We find that $\delta_\Theta \simeq \delta_u$, and as mentioned before, $r_t - \delta_u$ also appears to coincide with the radius where the kinetic energy profile $\bar{E}(r)$ transitions from a Gaussian to an exponential (see Figure 3.4). Finally, we also overlay the lengthscale δ_Θ on Figure 3.6 for comparison. Not surprisingly perhaps, we observe that δ_Θ coincides with the depth of the region in the RZ where $\bar{N}^2$ deviates most strongly from the radiative equilibrium profile. Therefore, δ_Θ provides a lengthscale that is associated with the depth of (partial) thermal mixing in the stable region.

To summarize our results so far, our inspection of the dynamics observed in this simulation has suggested the definition of three distinct lengthscales that each provides a different measure of the impact of convective motions on the underlying radiative zone. The first is the width δ_G of the Gaussian function fitted to the total kinetic energy profile below the base of the CZ. This parameterizes the profile

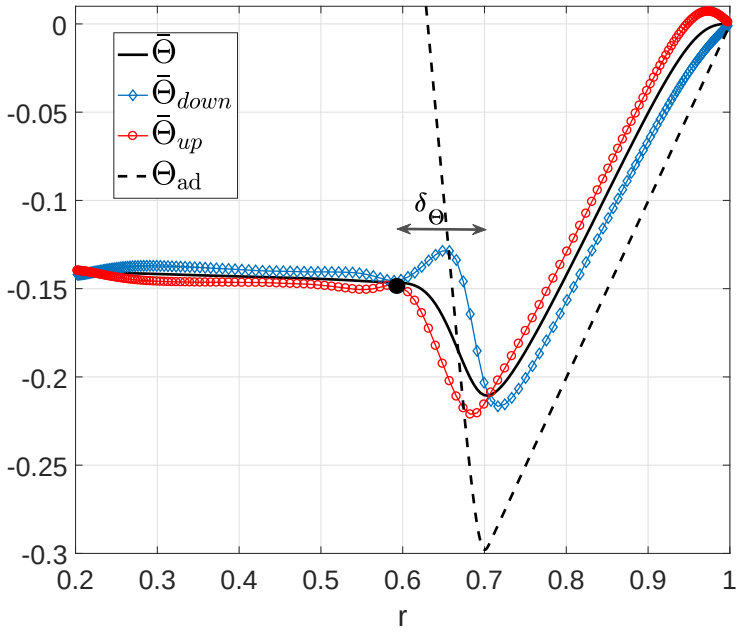

Figure 3.7: Temperature perturbations for $S = 5$, $d_{out} = 0.003$, and for $\mathrm{Ra}_o = 10^7$ plotted along with the adiabatic temperature $\Theta_{\rm ad}$.

of the decay of the turbulent kinetic energy with distance away from the CZ-RZ interface. The second is δ_u, given by the first zero of the radial correlation function of the downflows, $C(\delta)$. This can be interpreted as the lengthscale down to which the strongest downflows travel before stopping. The third is the distance δ_Θ from the base of the CZ down to the point of neutral buoyancy where $\bar{\Theta} = \bar{\Theta}_{down} = \bar{\Theta}_{up}$ which is both a good estimate of the stopping of motions and of the vertical extent of the partially thermally mixed region in the stable RZ. We have found that $\delta_G < \delta_u \simeq \delta_\Theta$ for this simulation, a result which actually holds for all of our simulations (see Table 3.1). This suggests that while δ_G may provide an average view of the kinetic energy available for mixing below the base of the convection zone, much of that mixing is actually controlled by the strongest downflows, which overshoot much more deeply. These results are qualitatively consistent with the findings of Brummell et al. (2002) [21] and Pratt et al. (2017) [113] in fully

compressible simulations, suggesting that the use of the Boussinesq approximation does not dramatically alter the dynamics of overshooting convection (at least near the base of a convective region deep within a star). In the following sections, we now look more broadly at how δ_G, δ_u and δ_Θ vary with input parameters.

3.4 Modeling the kinetic energy profile below the base of the CZ

In Section 3.3, we argued that the kinetic energy profile just below the base of the CZ resembles the Gaussian function $f(r)$ given in (3.23). Figure 3.8 shows this is the case in all of our simulations, which span a fairly wide range of values of the stiffness S, transition width d_{out}, and Rayleigh number Ra_o. Comparing Figures 3.8a, 3.8b and 3.8c, we clearly see that increasing the input Ra_o increases the overall kinetic energy in the system (and accordingly, the amplitude of the Gaussian), which is expected since Ra_o controls the strength of the convection. Interestingly, varying S and d_{out} (at fixed Ra_o) has very little effect on the kinetic energy within the CZ. This result is consistent with the notion that the turbulent intensity within the CZ only depends on its bulk Rayleigh number [84]

$$\mathrm{Ra}_b = \frac{\int_{r_t}^{r_o} \mathrm{Ra}(r) r^2 dr}{\int_{r_t}^{r_o} r^2 dr}, \tag{3.26}$$

which is roughly equal to Ra_o here since $\beta(r) \simeq -1$ for $r > r_t$ (see Equation (3.13)).

Korre et al. (2017) [84] showed further that in spherical Rayleigh-Bénard convection bounded by impermeable walls, the mean kinetic energy of the convection zone E_{CZ} scales as

$$E_{\mathrm{CZ}} = 3.7 \mathrm{Ra}_b^{0.72}, \tag{3.27}$$

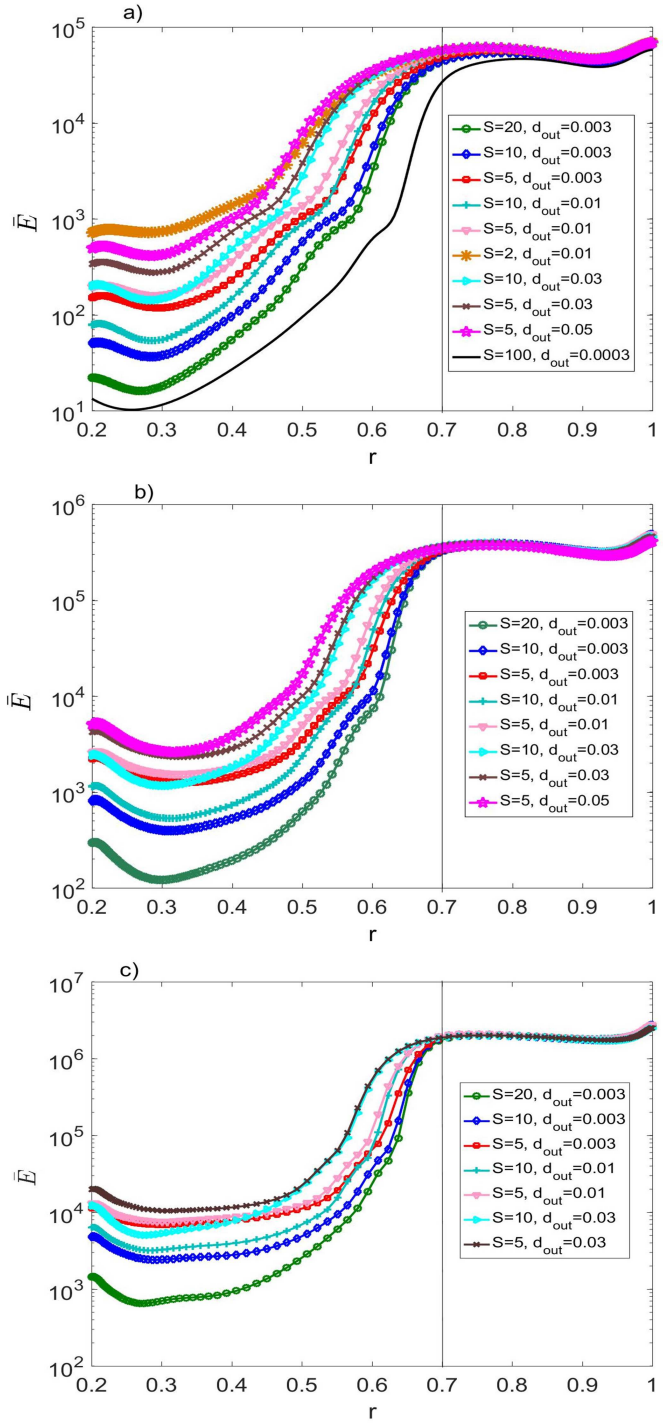

Figure 3.8: Kinetic energy profiles on a log scale for all the different S, d_{out} and for (a) $\mathrm{Ra}_o = 10^6$, b) $\mathrm{Ra}_o = 10^6$, and (c) $\mathrm{Ra}_o = 10^8$.

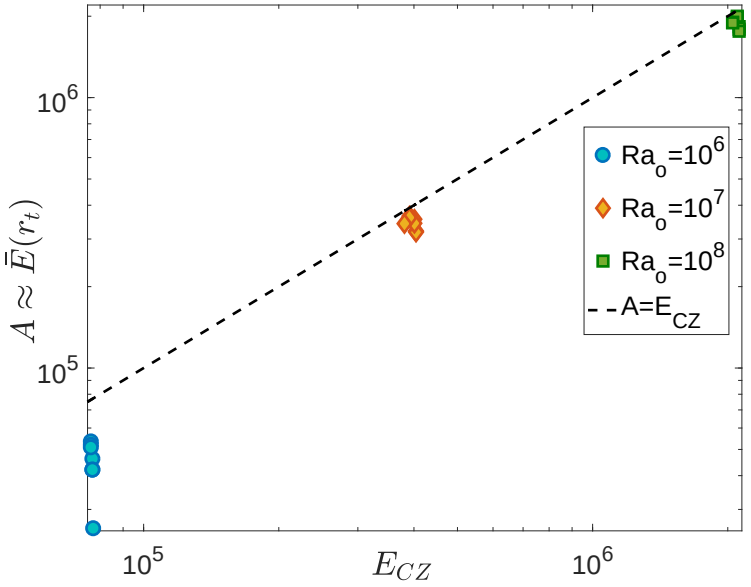

Figure 3.9: Plot of the extracted value of the amplitude of the Gaussian A, against our model for the mean kinetic energy in the CZ (see Equation (3.27)).

when its base is at $r_t = 0.7r_o$ and $\mathrm{Pr} = 0.1$, which is also the case for the CZ in this chapter. To verify whether this scaling also applies in a penetrative setup and therefore could be used in a predictive model, we compare the total kinetic energy at r_t to the predicted value of E_{CZ} in Figure 3.9. The quantity $\bar{E}(r_t)$ is extracted from the simulations by fitting $f(r)$ to the data, and assuming $\bar{E}(r_t) \simeq A$. We see that the predicted scaling works remarkably well for the more turbulent cases ($\mathrm{Ra}_o = 10^7$ and 10^8), and can therefore be used to obtain a good order-of-magnitude estimate of the amplitude of the turbulence present both within the CZ, as well as below the CZ-RZ interface through (3.23) provided a model for δ_G is also available.

To construct such a model, we use a simple energetic argument. Assuming that a parcel travels a distance δ_{en} from the base of the CZ adiabatically down to the point where its potential energy is equal to its initial kinetic energy, we can

write

$$E_{\rm CZ} = \delta_{en} \frac{\mathrm{Ra}_o}{\mathrm{Pr}} \int_{0.7-\delta_{en}}^{0.7} \beta(r) dr, \tag{3.28}$$

for the profile of $\beta(r)$ given in Equation (3.13). Note that this assumes that the background temperature profile has not been modified too much by the overshooting motions; we could in principle obtain a more accurate estimate for δ_G by using the actual stratification profile $\bar{N}^2 \mathrm{Pr}/\mathrm{Ra}_o$ computed from the simulations instead of the function $\beta(r)$ in the integrand. In practice, however, we verified that this does not make a substantial difference to the computed value of δ_{en} in any of our simulations, where thermal mixing is always weak. Using $\beta(r)$ in the integrand on the other hand has definite advantages: the integral can be evaluated analytically so Equation (3.28) becomes:

$$E_{\rm CZ} = \delta_{en} \frac{\mathrm{Ra}_o}{\mathrm{Pr}} S d_{in} \ln \left[\cosh \left(\frac{\delta_{en}}{d_{in}} \right) \right]. \tag{3.29}$$

Equation (3.29) can easily be solved numerically for δ_{en}, for any input S, Ra_o, and d_{in}.

In Figure 3.10, we plot δ_G against the energy-based theoretical prediction δ_{en} for all available simulations. The quantity δ_G was measured from the DNS simulations by fitting the Gaussian profile (3.23) to the total kinetic energy profile $\bar{E}(r)$ from r_t down to $r_t - \delta_\Theta$ (see Section 3.3), and all the results are reported in Table 3.1. We observe that all the points lie close to the straight line $\delta_G = 1.2\delta_{en}$ (dashed black line). This result is rather remarkable given that our input parameters span a fairly large region of parameter space, with a resulting δ_G ranging from 0.01 to 0.12. The result suggests that the physics of the energetic argument put forward is mostly correct. Note that the downflows originating from the convection zone obviously do not all have the same kinetic energy, so $E_{\rm CZ}$ is

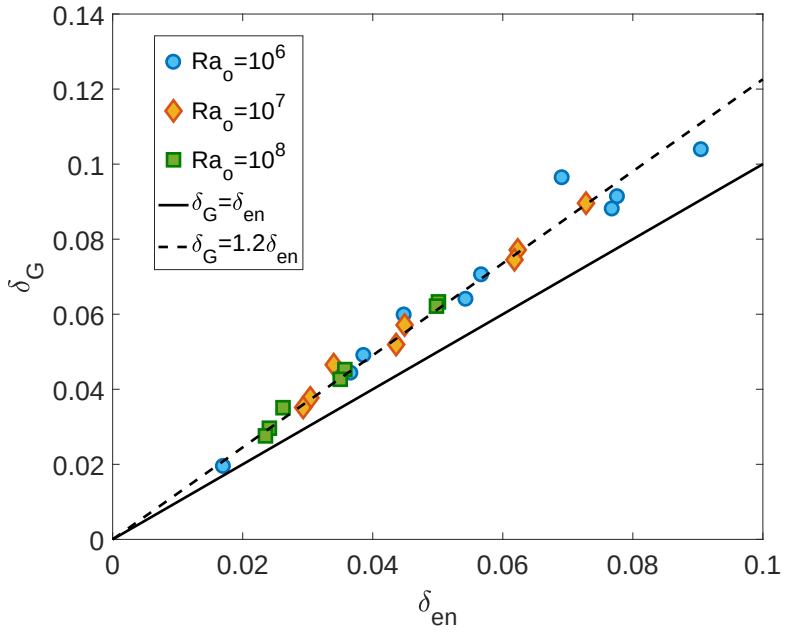

Figure 3.10: Plot of δ_{en} versus δ_G for all the cases where Ra_o has been used as reference.

merely an estimate of their mean, and δ_{en} is correspondingly merely an estimate of how far a typical eddy could overshoot. As a result, the prefactor relating δ_G to δ_{en} could have been any factor of order unity, but just happens to be 1.2 in this particular set of simulations. We expect this prefactor to vary somewhat if the Prandtl number varies dramatically, or if compressibility is taken into account.

While Equation (3.29) does not have any analytical solutions in general, it has two limits of interest. When $\delta_{en} \ll d_{in}$, Equation (3.29) becomes

$$E_{\mathrm{CZ}} \simeq \delta_{en} \frac{\mathrm{Ra}_o}{\mathrm{Pr}} S d_{in} \left(\frac{1}{2} \left(\frac{\delta_{en}}{d_{in}} \right)^2 \right), \tag{3.30}$$

leading to

$$\delta_{en} \simeq \left(\frac{2E_{\rm CZ}d_{out}{\rm Pr}}{{\rm Ra}_o}\right)^{1/3} \Rightarrow \delta_G \approx 1.2\left(\frac{2E_{\rm CZ}d_{out}{\rm Pr}}{{\rm Ra}_o}\right)^{1/3} = 1.2\left(\frac{2E_{\rm CZ}d_{in}{\rm Pr}}{S{\rm Ra}_o}\right)^{1/3}. \tag{3.31}$$

Physically speaking, this limit corresponds to the case where the downflows only sample the transition region below the CZ where $\beta(r)$ varies linearly with distance to r_t. As such, it is not surprising to find that δ_G in this case does not directly know about S, but only knows about the slope of $\beta(r)$. In Figure 3.11(a), we plot the measured δ_G versus the transition width d_{out} along with the predicted line for δ_G as expressed in Equation (3.31). We clearly see that our prediction works remarkably well for the cases where $\delta_G < d_{in}$.

In the opposite limit, when $\delta_{en} \gg d_{in}$,

$$E_{\rm CZ} \simeq \delta_{en}\frac{{\rm Ra}_o}{\rm Pr}Sd_{in}\left(\frac{\delta_{en}}{d_{in}}\right), \tag{3.32}$$

leading to

$$\delta_{en} \simeq \left(\frac{E_{\rm CZ}{\rm Pr}}{S{\rm Ra}_o}\right)^{1/2} \Rightarrow \delta_G \approx 1.2\left(\frac{E_{\rm CZ}{\rm Pr}}{S{\rm Ra}_o}\right)^{1/2}. \tag{3.33}$$

In this limit the downflows penetrate down to the region where $\beta(r) \simeq S$, so it is not surprising to see that δ_G depends on S, but is independent of d_{out}. Figure 3.11(b) shows the measured δ_G against the stiffness parameter S along with the scaling given in Equation (3.33). We find that the scaling law $S^{-1/2}$ works for the simulations in which $\delta_G > d_{in}$, but is off by a constant factor. This is not too surprising since the expansion used to obtain Equation (3.33) is technically valid only in the limit $(\delta_{en}/d_{in}) \to \infty$, which does not hold true for any of our simulations where δ_G is fairly close to d_{in}.

Ultimately, we see that δ_G is either proportional to $S^{-1/3}$ or to $S^{-1/2}$, implying that it decreases with increasing S in both limits. This is in agreement with the

naive expectation that turbulent fluid motions generated in the CZ have a harder time penetrating deeply into a more strongly stratified RZ. These scalings are quite different from the ones proposed by Zahn (1991) [160] and Hurlburt et al. (1994) [78], which both argue for a penetration depth (i.e. the depth of the adiabatically stratified layer) scaling as S^{-1}, and an overshoot depth (the depth of their thermal adjustment layer) scaling as $S^{-1/4}$. The difference between their theory and our results is relatively easy to understand, however. To start with, their model setup is quite different from ours, relying on changes in the thermal conductivity to drive the transition from a radiative to a convective environment whereas we produce this transition by effectively adding a heating source (see Section 3.2). Since their theoretical predictions fundamentally rely on the changes in thermal conductivity, it is not surprising that they would be at odds with our own scalings. Furthermore, their S^{-1} scaling relies on the existence of an adiabatic penetrative layer, and their $S^{-1/4}$ scaling relies on an exponentially damped overshoot. Neither of these dynamics are seen here. Note also that Rogers & Glatzmaier (2005) [120] presented the results of 2D anelastic simulations of penetrative and overshooting convection, where they confirmed the S^{-1} scaling in the penetrative limit, but report on a much shallower scaling law $\sim S^{-0.04}$ in the moderate- and high-S non-penetrative limit. While their definition of S differs somewhat from that of Hurlburt et al. (1994) [78], that difference cannot fully explain the rather large discrepancy in observed scaling with S. Instead, clues to the possible origin of this discrepancy might lie in the applied thermal boundary conditions: Rogers & Glatzmaier (2005) [120] use isothermal boundary conditions, and state that *"In simulations in which a constant heat flux boundary condition is used at the top, the scaling relation at moderate S values is not as shallow"*. Our findings then do not contradict any of these results.

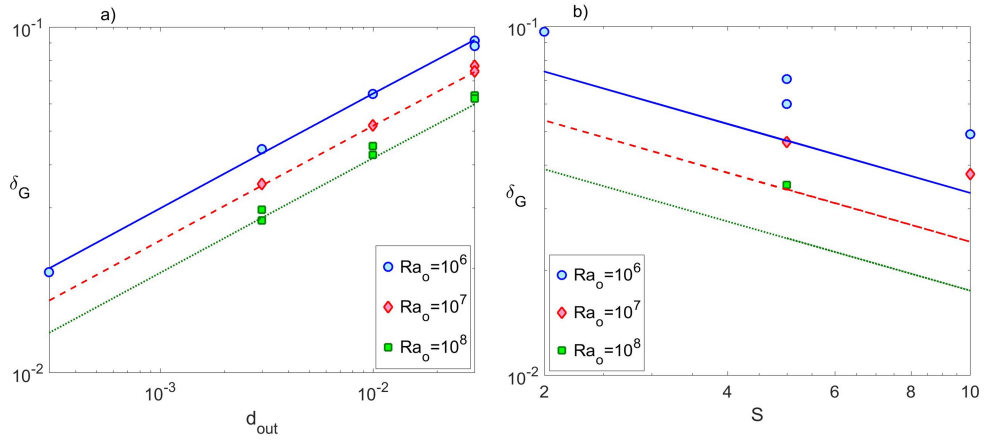

Figure 3.11: Plot of the measured δ_G against (a) the transition width d_{out}, and (b) the stiffness parameter S. In (a), only those simulations for which $\delta_G < \delta_{in}$ are shown. Also shown is the predicted scaling law for δ_{en} given in Equation (3.31). In (b), only those simulations for which $\delta_G > \delta_{in}$ are shown. Also shown is the predicted scaling law for δ_{en} given in Equation (3.33).

Finally, we note that δ_G counter-intuitively decreases with increasing Ra_o in both of these limits. Indeed, one would expect that the increase in the turbulent convective velocities associated with a higher Ra_o would lead to deeper overshooting into the RZ. However, the background stratification of the deep RZ in our model setup scales like $\bar{N}^2 \simeq S\mathrm{Ra}_o/\mathrm{Pr}$ which increases with increasing Ra_o for fixed values of S. We therefore see that this second effect dominates the system dynamics, leading to a shallower – not deeper – δ_G as Ra_o increases.

3.5 Thermal mixing in the RZ

In this Section, we focus on quantifying the properties and dependence on input parameters of the regime of partial thermal mixing in the RZ. Figure 3.12a shows $\bar{\Theta}_{down}$, $\bar{\Theta}_{up}$ and $\bar{\Theta}$, as defined earlier, for the simulation with $S = 5$, $d_{out} = 0.003$ and $\mathrm{Ra}_o = 10^7$ (Case 11, Table 3.1) analyzed in Section 3.3, along with a more laminar case of $\mathrm{Ra}_o = 10^6$ (Case 2, Table 3.1) and a more turbulent case of

$\mathrm{Ra}_o = 10^8$ (Case 19, Table 3.1). Figure 3.12b shows the corresponding buoyancy frequency profiles, and Figure 3.12c shows the associated turbulent temperature flux (see below for its definition and discussion).

Within the CZ, we find that $\bar{N}^2$ is closer to 0 (and correspondingly that $\bar{\Theta}$ follows Θ_{ad} more closely) for larger Ra_o. This is to be expected since a more turbulent convection zone is more efficient in driving the mean temperature toward an adiabatic state. Meanwhile in the radiative region, we recover the same overall behavior for $\bar{N}^2$, $\bar{\Theta}_{down}$, $\bar{\Theta}_{up}$ and $\bar{\Theta}$ that was already observed in the reference simulation: mixing is not strong enough to cause an extension of the convection zone, but does smooth out the mean stratification down to a depth $\sim \delta_\Theta$ below the base of the CZ. We also see that δ_Θ decreases with increasing Ra_o (and same is true for δ_u), as shown in Table 3.1. This trend mirrors the corresponding decrease in δ_G with increasing Rayleigh number discussed in Section 3.4, which was attributed to the increasing stratification of the RZ. Since δ_Θ continues to be a good proxy for the depth of the partially thermally mixed region (see Figure 3.12b), our findings therefore imply that the latter becomes shallower with increasing Ra_o .

More generally, we have found that δ_u, δ_Θ and δ_G are all very closely related to one another across all of our simulations, and can easily be predicted from the energy-based lengthscale δ_{en} proposed in Section 3.4. Indeed, as shown in Figure 3.13, we find that $\delta_u \simeq \delta_\Theta \simeq 2.9\delta_{en}$. In other words, the energy-based argument proposed in Section 3.4 applies equally well to predict the neutral buoyancy point and the stopping depth of individual (strong) downflows, albeit with a somewhat larger prefactor. This provides a very simple way of estimating the depth of the partially thermally-mixed region below the base of the convection zone simply from knowledge of the model parameters.

A complete model for thermal mixing by convective overshoot requires a quan-

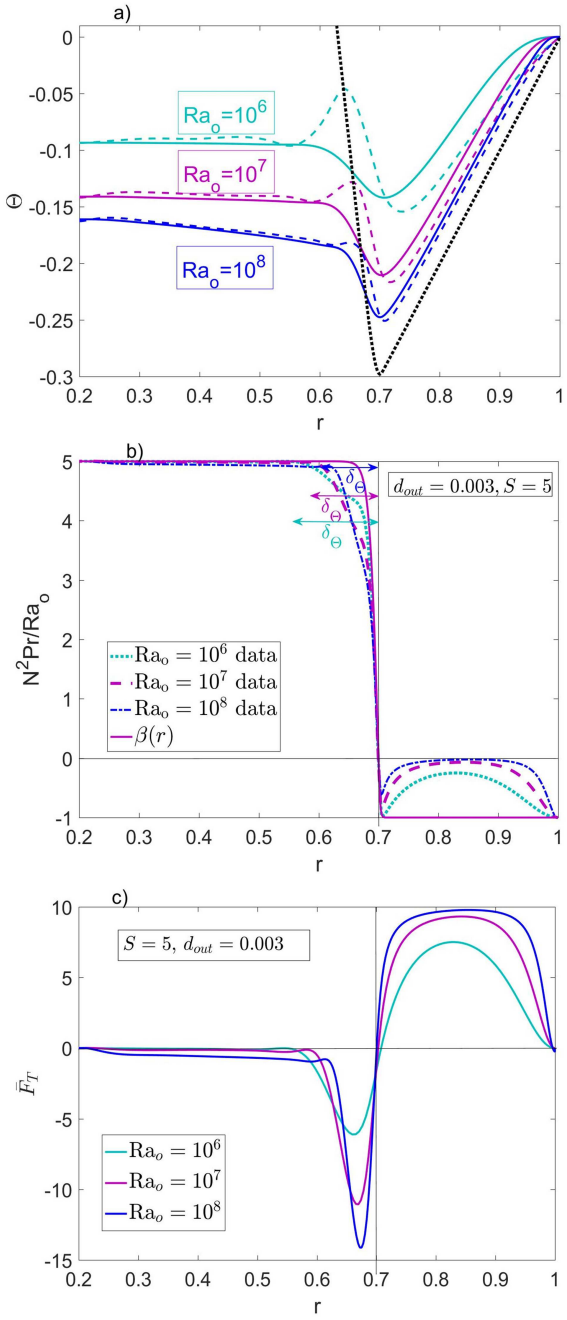

Figure 3.12: a) Plot of the temperature perturbations (where the solid lines correspond to $\bar{\Theta}$ and the dashed lines correspond to $\bar{\Theta}_{down}$ along with the respective adiabatic one (dotted black line), b) plot of $\bar{N}^2(r)\mathrm{Pr}/\mathrm{Ra}_o$ along with the respective $N^2_{\mathrm{rad}}(r)\mathrm{Pr}/\mathrm{Ra}_o$, and c) plot of the fluxes $\bar{F}_T$, for $S = 5$, $d_{out} = 0.003$ and three different Ra_o.

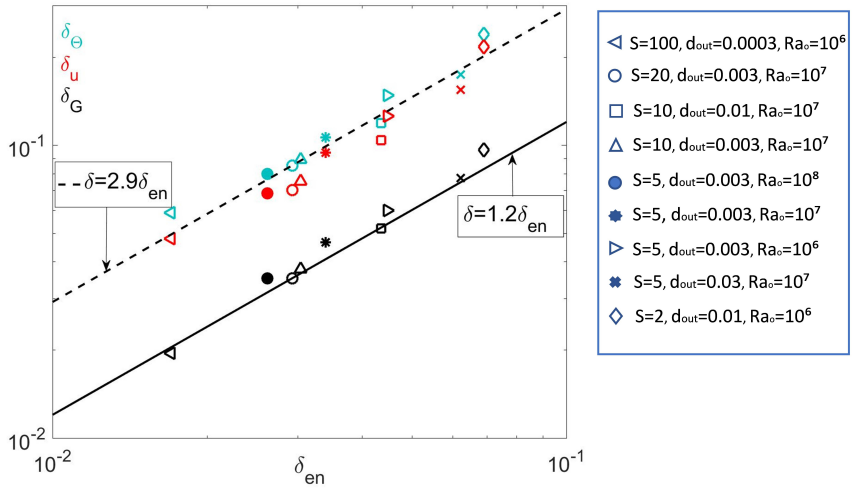

Figure 3.13: Comparison of δ_u, δ_Θ and δ_G against the estimated δ_{en}, for the simulations indicated on the legend. Also shown are the best fit to the data, namely $1.2\delta_{en}$ for δ_G and $2.9\delta_{en}$ for δ_u and δ_Θ.

titative understanding of the strength of such mixing, i.e. of the turbulent heat flux. In this particular model setup, the turbulent heat flux can easily be measured once the system is in a statistically stationary state. Indeed, taking the horizontal average of the thermal energy equation (3.10) in that state, integrating it once and applying the boundary condition at r_i, we find that

$$\bar{F}_T \equiv \overline{u_r \Theta} = \frac{1}{\mathrm{Pr}} \frac{\partial \bar{\Theta}}{\partial r}, \tag{3.34}$$

or in other words, that the sum of the turbulent and diffusive heat fluxes associated with the temperature perturbation $\bar{\Theta}$ must be zero. This is consistent with our assumption that the total flux through the system is fixed. We then have

$$\bar{F}_T = \frac{1}{\mathrm{Pr}} \left(\frac{\bar{N}^2 \mathrm{Pr}}{\mathrm{Ra}_o} - \beta(r) \right), \tag{3.35}$$

so the turbulent temperature flux $\bar{F}_T$ can easily be visualized on Figure 3.12b as the (signed) difference between the dashed line and the solid line (times Pr^{-1}). It

is shown, for better clarity, in Figure 3.12c for the same runs.

As expected, the temperature flux is generally negative in the radiative zone and positive in the convection zone. It almost always changes sign very close to the radius where $\bar{N}^2$ changes sign. In none of the simulations do we see the formation of an *extended* stably stratified region subject to substantial positive non-local convective fluxes of the kind reported by Käpylä et al. (2017) [82], who called such a layer a "Deardorff layer" following Deardorff (1966) [43] and Brandenburg (2016) [14]. This difference between our simulations and theirs is probably due to two complementary effects. Käpylä et al. (2017) [82] ran fully compressible simulations which more realistically capture the asymmetry between weak warm upflows and strong cold downflows than our Boussinesq setup. This asymmetry promotes non-local heat transport by the plumes, allowing the strongest cold downflows to penetrate more coherently and more deeply into the RZ than they would otherwise before warming up. Compressibility is however not a sufficient condition for the formation of a significant Deardorff layer, since none were seen in the compressible simulations of Brummell et al. (2002) [21] or Pratt et al. (2017) [113]. Käpylä et al. (2017) [82] explain this, showing that the Deardorff layer is almost absent if the thermal diffusivity profile (or equivalently, the background radiative temperature profile) is fixed and varies abruptly with depth, which is indeed the case in the simulations of Brummell et al. (2002) [21]. In our numerical setup, which uses the Boussinesq approximation, the asymmetry between upflows and downflows is weak, induced only by the spherical geometry and the boundary conditions. In addition, most of our simulations were run with a transition steepness set by taking $d_{out} = 0.003$, which is very sharp (e.g. see Figure 3.12). We therefore should not expect to see the formation of a Deardorff layer in these cases. We can however detect the existence of one in the largest d_{out} runs (i.e.

when $d_{out} = 0.03$; see Figure 3.14) but it remains very shallow. As such, our simulations cannot really probe the dynamics of the Deardorff layer even though we might expect that one should be present in the Sun.

The magnitude of the turbulent flux below the CZ increases with Ra_o, as seen in Figure 3.12c, even though the depth of the mixed layer concurrently decreases. This is not surprising since the r.m.s. velocity of the downflows increases with Ra_o (see Equation (3.27)). However, the increase of $\bar{F}_T$ with Rayleigh number is not particularly pronounced, perhaps scaling as $\bar{F}_T \sim \mathrm{Ra}_o^{0.18}$. Within the scope of the simulations shown here, we see that increasing Ra_o by a factor of 100 only increases the peak value of $|\bar{F}_T|$ by a factor of about 2.2 in the RZ. This shows that the turbulent flux itself does not scale as steeply as the r.m.s. velocity (which would lead to $\bar{F}_T \sim \mathrm{Ra}_o^{0.36}$), implying in turn that the amplitude of the temperature fluctuations must decrease with increasing Ra_o. This can in fact easily be verified in Figure 3.12a, which shows that the profiles of $\bar{\Theta}$, $\bar{\Theta}_{down}$ and $\bar{\Theta}_{up}$ are much closer to one another at $\mathrm{Ra}_o = 10^8$ than at $\mathrm{Ra}_o = 10^6$. This result can be explained by noting that turbulence plays an increasingly dominant role at larger Rayleigh number, and has a tendency to homogenize the temperature between upflows and downflows. Given the weak dependence on Ra_o, the range of available simulations is unfortunately not large enough to extract a reliable scaling law between $\bar{F}_T$ and Ra_o – the latter could be a power law (in which case the power would be of the order of 0.18, as mentioned earlier), but could just as well be logarithmic, or take some other form. As a result, we defer any prediction on the scaling of $\bar{F}_T$ with Ra_o to future work. Nevertheless, our results point to the crucial importance of accounting for the turbulent mixing between upflows and downflows when modeling mixing by overshooting convection, something that had rarely been taken into account in previous plume models of overshoot [127, 124]

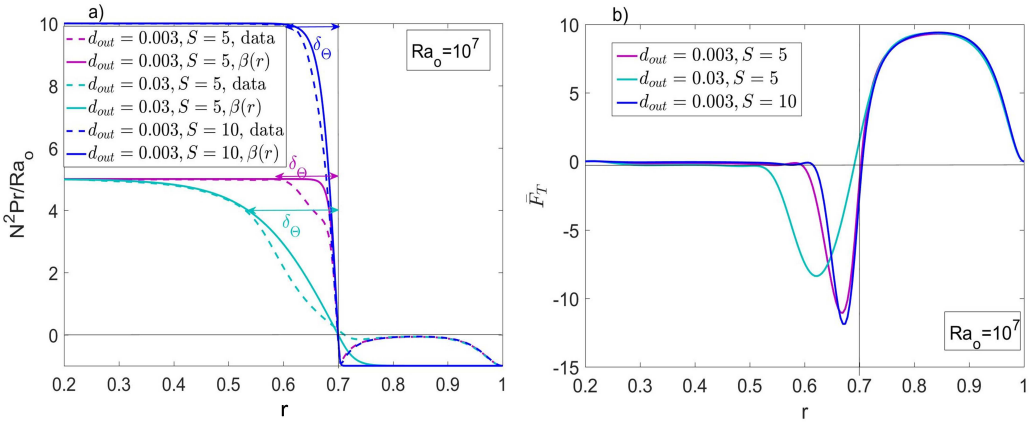

Figure 3.14: a) Comparison of $\bar{N}^2(r)\mathrm{Pr}/\mathrm{Ra}_o$ with the corresponding background, $\beta(r)$, for simulations with $\mathrm{Ra}_o = 10^7$, two different values of S (5 and 10), and two different values of d_{out} (0.003 and 0.03). b) Corresponding turbulent temperature fluxes for the same simulations.

until the work of Rempel (2004) [115].

Finally, we explore the dependence of thermal mixing on S and d_{out} in Figure 3.14a, which shows $\bar{N}^2(r)\mathrm{Pr}/\mathrm{Ra}_o$ and $N^2_{\mathrm{rad}}(r)\mathrm{Pr}/\mathrm{Ra}_o = \beta(r)$ for our typical simulation of $S = 5$, $d_{out} = 0.003$ and $\mathrm{Ra}_o = 10^7$ (Case 11, Table 3.1) along with one from a simulation with the same $S = 5$ and Ra_o but a larger $d_{out} = 0.03$ (shallower transition) (Case 16, Table 3.1), and one with the same $d_{out} = 0.003$ and Ra_o, but a larger $S = 10$ (stiffer case) (Case 12, Table 3.1). Figure 3.14b shows the corresponding turbulent fluxes for the same simulations. We see that increasing S at fixed d_{out} varies δ_Θ a little (so the partially mixed layer below the CZ is somewhat shallower), but the magnitude of the turbulent flux is hardly affected. Increasing d_{out} at fixed S on the other hand has a much larger effect on δ_Θ (which increases significantly), and on the fluxes (which decrease by about 25 percent). This shows the importance of smooth versus abrupt transitions in $\beta(r)$, but we have not yet been able to construct a quantitative model to explain these results.

3.6 Summary and discussion

3.6.1 Summary

In this chapter, we have presented a series of numerical experiments designed to quantify the interaction between a convective zone and an underlying stably stratified zone, in a spherical geometry and within the context of the Boussinesq approximation. In order to mimic the stellar case, we have used a fixed-flux inner boundary condition at a radius located somewhat above the nuclear burning region, and a fixed-temperature outer boundary condition. For simplicity, all the diffusivities as well as gravity are held constant in the domain, and so is the adiabatic temperature gradient. As a result, a heating source must be invoked in the vicinity of the radiative-convective interface to ensure that the lower part of the domain is indeed stably stratified, while the upper part of the domain is convectively unstable. The selected radial distribution and amplitude of the heating source sets the radiative temperature gradients in the radiative and convective zones respectively, and can be adjusted to create stable and unstable regions with varying relative stability (quantified through the non-dimensional stiffness parameter S), as well as steeper or shallower transitions between the two (quantified through the non-dimensional transition width d_{out}): see Section 3.2. For simplicity, the overall geometry of the system was fixed to mimic the solar case (with the radiative–convective interface located at $r_t = 0.7r_o$), and we also fixed the Prandtl number $\mathrm{Pr} = \nu/\kappa = 0.1$ in all of our simulations. The parameters varied were S and d_{out}, as well as the global Rayleigh number Ra_o (defined in Equation (3.11)). Increasing Ra_o is therefore equivalent to reducing the viscosity and thermal diffusivity concurrently. We explored simulations with Ra_o ranging from 10^6 to 10^8. Note for comparison that $\mathrm{Pr} \sim 10^{-6}$ and $\mathrm{Ra}_o \gg 10^{20}$ in the Sun, so none

of the simulations should be used to *directly* infer properties of the overshooting convective motions. Instead, we merely seek to understand how the properties of the radiative–convective interface *scale* with input parameters, to later attempt an extrapolation of the results to the solar case (while always maintaining some degree of healthy skepticism).

Our simulations all share the same characteristics. We found as in [84] that the mean kinetic energy in the CZ, called E_{CZ}, scales as $\mathrm{Ra}_b^{0.72}$ (see Equation (3.27)), where Ra_b is the volume-averaged Rayleigh number within the CZ (see Equation (3.26)), which in this work is quite close to Ra_o. The total kinetic energy of fluid motions decays below the radiative–convective interface as a Gaussian function of the distance to r_t (see Equation (3.23)) whose width δ_G can be predicted from first principles using a simple energy argument (aside from a constant of order unity). Indeed, assuming that an average downflow travels a distance δ_{en} adiabatically from the base of the convection zone until its potential energy equals its estimated initial kinetic energy E_{CZ}, we can compute δ_{en} by solving Equation (3.29). We then showed that, for all available simulations, $\delta_G \simeq 1.2\delta_{en}$. Through this equation, we can then quantify how δ_G varies with both the stiffness and steepness of the background stratification profile as well as with the input Rayleigh number.

We also looked more specifically at how far the *strongest* downflows penetrate into RZ, by computing the correlation function $C(\delta)$ between the radial velocity at r_t and a distance δ away from it. We found that these strong downflows stop at a distance $\delta_u \simeq 2.9\delta_{en}$ from the base of the convection zone, for any S, d_{out} and Ra_o. This distance δ_u, computed as the first zero of $C(\delta)$, also turns out to correspond to the level of neutral buoyancy for the downflows δ_Θ. The strict correlation discovered between δ_u, δ_G and δ_{en} therefore strongly suggests that the simple energetic argument put forward is sufficient to characterize the dynamics

of the overshooting plumes.

We found that the region between $r_t - \delta_u$ and r_t is partially thermally mixed (at these values of the Rayleigh number), resulting in an adjusted buoyancy frequency profile substantially smoother than that of the imposed background. However, we did not see any actual penetration in the traditional definition of the extension of the CZ into the RZ (e.g. [160, 78]). This is because the turbulent temperature flux $\bar{F}_T$ induced by overshooting motions in the RZ remains moderate in all the simulations. We found that it is independent of S, and only scales weakly with Rayleigh number (increasing by a factor of about 2 when Ra_o increases by a factor of 100), suggesting either a very weak power law ($\bar{F}_T \propto \mathrm{Ra}_o^{0.18}$) or a logarithmic dependence on Ra_o.

Finally, below $r_t - \delta_u$ the nature of the system dynamics clearly change. The turbulent temperature flux becomes negligible, and the kinetic energy profile is no longer Gaussian, but appears closer to exponential. While weak fluid motions are present, they appear to be more related to the "damped tail" of linearly unstable convective modes (in the sense described by, for instance, [52]) rather than to internal gravity waves.

3.6.2 Comparison with previous numerical experiments

As discussed in Section 3.1, there have been quite a few numerical investigations of the dynamics of overshooting and penetrative convection to date. In what follows, we focus on the ones that address the question of overshoot under a convective zone (sometimes referred to as "undershoot", although we prefer not to use that terminology), rather than above it. These include (among others) the 2D fully compressible simulations of Hurlburt et al. [77], [78], Freytag et al. (1996) [52] and Pratt et al. (2017) [113], the 3D fully compressible simulations of

Brummell et al. (2002) [21], Singh et al. (1995) [130] (see also [131, 123, 82]), the 2D anelastic simulations of Rogers & Glatzmaier (2005) [120] (see also [121]), and the 3D ones of Brun et al. (2017) [24].

Several general conclusions can be drawn from comparing the outcome of these simulations to one another, and to ours. First and foremost is that penetrative convection in the strict definition of the term (i.e. the extension of the convection zone substantially beyond the threshold for linear instability) had so far not been observed in fully turbulent 3D simulations [21, 82, 24], and this continues to be the case here. As reviewed in Section 3.1, the fact that penetration is seen in 2D at sufficiently low values of S (e.g. [120]) and in very laminar 3D simulations (e.g. [123]) can be attributed to the artificially large geometric filling factor of 2D plumes vs. 3D plumes [21, 115]. However, none of the existing 3D simulations (including ours) reach particularly high values of the Rayleigh number. Hence, whether this result will continue to hold when progress in supercomputing allows us to simulate convection at much higher Rayleigh numbers remains to be determined (see below for more on this point).

A second common point between (almost) all simulations is that the kinetic energy of vertical motions within the downflows drops substantially within the CZ as they approach the RZ from above, owing to their lateral deflection, even in low stiffness cases. As a result, the dominant contribution to the total kinetic energy within the RZ is from horizontal flows. While this may superficially seem at odds with the standard mental picture one may have of overshooting plumes, note that most of the vertical transport is still carried out by the strongest, most-concentrated downflowing motions, as was described in other simulations, e.g. [21, 113], but the content of these strongest plumes (heat, chemical species) is then advected (and mixed) laterally by turbulent horizontal flows. Precisely how

strong these concentrated downflows can get (for given Rayleigh and Prandtl numbers in the CZ) depends on the dimensionality of the simulations and on the compressibility of the fluid (Boussinesq vs. anelastic vs. fully compressible). Since the strength and depth of the downflows control other RZ processes, such as the generation of gravity waves or the formation of a Deardorff layer for instance, it is not surprising to see that the latter are strongly model-dependent, present in some simulations, absent in others.

A third common point between all simulations is that the depth of the turbulent overshooting layer (as measured by looking at either the kinetic energy profile or the kinetic energy flux below the base of the CZ) does seem to decrease with increasing stiffness S, which is an intuitive result. What differs however is the measured scaling law relating this depth to S. Hurlburt et al. (1994)[78] and Brummell et al. (2002) [21] both ran direct numerical simulations of overshooting convection in 2D and 3D respectively, where the radiative–convective transition is caused by a sudden change in the thermal conductivity. They both state that their results are consistent with estimates based on a variant of Zahn's theory [160], which predicts that the overshooting depth should scale as $\sim S^{-1/4}$ when the total flux through the system is fixed. Rogers & Glatzmaier (2005) [120] presented 2D anelastic simulations with fixed temperature boundary conditions, where the radiative–convective transition is also caused by a sudden change in the thermal conductivity, and found a much shallower scaling law $\sim S^{-0.04}$. Meanwhile, in our Boussinesq 3D fixed flux direct numerical simulations, where the transition is driven by the existence of a heating source around r_t, we find somewhat steeper scaling laws, with $\sim S^{-1/3}$ or $\sim S^{-1/2}$ depending on whether the background radiative temperature gradient is shallower or steeper, respectively. We believe that the observed difference in the scaling laws reported in these various papers

is more likely to be due to the differences in boundary conditions or model setup used rather than compressibility, but this should be verified in future work. It would be interesting for instance to run a comparative study of overshooting and penetrative convection in various systems that all have the same background profile of N^2, but that are driven in different ways (i.e. by varying the diffusivities, or the equation of state, or using a heating function, for instance).

In any case, gaining a better understanding of the scaling of the overshoot depth with S is arguably less important than constraining its scaling with the Rayleigh number, since S is not expected to be too large in stars. Ra_o on the other hand needs to be increased by more than 10 orders of magnitude to reach the stellar regime. Not many studies have systematically looked into this problem. The work of Brummell et al. (2002) [21] seems to suggest (see their Section 3.7) the approximate scaling $\delta \sim \mathrm{Ra}^{-0.25}$. In Rogers & Glatzmaier (2005) [120], the situation is complicated by the fact that the measured scalings with Rayleigh number appear to depend sensitively on S: in the less stiff cases, the overshooting layer depth increases with Rayleigh number, but the opposite is true for stiffer cases. The simplicity of our simulations however, easily allows us to vary Ra_o independently of all other parameters, and we find that $\delta_G \sim \mathrm{Ra}_o^{-0.09}$ in the case where the transition is steep, and $\delta_G \sim \mathrm{Ra}_o^{-0.14}$ when it is shallow. In both cases the overshoot depth therefore decreases with Ra_o at fixed S as discussed in Section 3.4 (see Equations (3.31) and (3.33), using $E_{\mathrm{CZ}} \sim \mathrm{Ra}_o^{0.72}$), although the actual power law is quite shallow.

Finally, we note that very few studies, to our knowledge, really looked into the actual spatial variation of the kinetic energy profile with depth (which is a good proxy for the variation of the mixing coefficient with depth, see below). Freytag et al. (1996) [52] were the first to clearly state that their simulations show an

exponential decay of the r.m.s velocities with depth below the convection zone. They showed that this profile is consistent with these velocities being the stable exponentially-decaying tail of the linearly unstable convective modes. Unfortunately, this also demonstrates that their simulations cannot be in the turbulent regime, a notion that is consistent with a simple visual inspection of their Figures 2-5. By contrast, our simulations are quite turbulent down to about $r_t - \delta_u$. We find that the kinetic energy profile is Gaussian instead of exponential in that region, and only becomes exponential once the fluid motions are sufficiently slow for all nonlinearities to be negligible.

3.6.3 A prescription for mixing by overshoot

Our numerical results have led us to suggest a very simple Gaussian model for the kinetic energy profile below the base of the convection zone, given by

$$E(r) = E_{\rm CZ} \exp\left(-\frac{(r-r_t)^2}{2\delta_G^2}\right), \tag{3.36}$$

where $E_{\rm CZ}$ is the typical kinetic energy of fluid motions within the convection zone (i.e. somewhere within the bulk of the zone). This quantity can for instance be determined from mixing length theory in a stellar evolution code, or from Equation (3.27) in more idealized Boussinesq setups (recalling that the prefactor could depend on the Prandtl number and on the aspect ratio of the convective region). The lengthscale δ_G on the other hand can be estimated by using the energy-based lengthscale δ_{en} discussed in Section 3.4 (see Equation (3.28)), with $\delta_G \simeq \delta_{en}$. A factor of unity relating the two is left here unspecified, and may weakly depend on the Prandtl number and on compressibility. Dimensionally

speaking, the lengthscale δ_{en} can be found by solving the equation

$$\frac{1}{2}v_{\rm CZ}^2 = -\delta_{en}\int_{r_t-\delta_{en}}^{r_t}\frac{\bar{g}}{H_p}\left(\nabla-\nabla_{\rm ad}\right)dr, \tag{3.37}$$

where $v_{\rm CZ}$ is the convective velocity in the bulk of the convection zone, $\bar{g}$ is the local gravity, and H_p is the pressure scaleheight. With this formula, the computation of the depth δ_G only depends on the local temperature gradient as well as standard variables returned by stellar evolution codes, rather than the manner in which this temperature gradient (and the CZ-RZ transition) is actually generated. Note that this energy-based argument for estimating the overshoot depth is ultimately quite standard; it recovers, for instance, that of Christensen-Dalsgaard et al. (2011) [39] (see their equation 18) if $\nabla-\nabla_{\rm ad}$ is taken to be approximately constant below the base of the convection zone, in which case δ_{en} satisfies

$$\frac{\delta_{en}}{H_p} = \left(\frac{v_{\rm CZ}^2}{2\bar{g}H_p|\nabla-\nabla_{\rm ad}|}\right)^{1/2}. \tag{3.38}$$

If, on the other hand, $\nabla-\nabla_{\rm ad}$ is assumed to vary linearly with depth below the CZ, with $\nabla-\nabla_{\rm ad}\simeq\eta(r-r_t)$, then

$$\frac{\delta_{en}}{H_p} = \left(\frac{v_{\rm CZ}^2}{\bar{g}H_p^2\eta}\right)^{1/3}. \tag{3.39}$$

From the kinetic energy profile (3.36), we can then form a diffusion coefficient to model compositional mixing by overshooting motions

$$D_{ov}(r) = D_{\rm CZ}\exp\left(-\frac{(r-r_t)^2}{2\delta_G^2}\right), \tag{3.40}$$

assuming that $D_{ov}\propto v_{\rm CZ}^2\tau_{\rm CZ}$ as in [52], where $\tau_{\rm CZ}$ is some convective turnover timescale just above the base of the convection zone.

In order to apply Equation (3.39) to the Sun, we extract all the relevant quantities from the interface between the interior radiation zone and convective envelope of a 1 solar mass Main-Sequence model computed with MESA[1] [110, 111]. We find that $v_{\rm CZ} \simeq 6,000{\rm cm/s}$ in the bulk of the convection zone, and $g \simeq 50,000{\rm cm/s^2}$, $H_p \simeq 5\times10^9{\rm cm}$, and $\eta \simeq \times10^{-10}{\rm cm^{-1}}$ near the interface, leading to $\delta_{en}/H_p \simeq 0.006$. Similar calculations made at the interface between the interior convective zone and radiative envelope of a 2 solar mass Main-Sequence model yield $v_{\rm CZ} \simeq 7,000{\rm cm/s}$, $g \simeq 200,000{\rm cm/s^2}$, $H_p \simeq 5\times10^9{\rm cm}$, and $\eta \simeq \times10^{-11}{\rm cm^{-1}}$, leading to $\delta_{en}/H_p \simeq 0.01$. In both cases, δ_{en} (and by definition δ_G) is quite a small fraction of a pressure scaleheight, and would result in much shallower predictions for the depth of the overshoot-mixed layer than what is commonly assumed in stellar evolution models (e.g. from the model of Herwig (2000) [74] with $f \simeq 0.1H_p$). Even shallower predictions would be obtained using values of $v_{\rm CZ}$ taken closer to the edge of the convective region. Whether overshoot is in fact as shallow as predicted in real stars remains to be determined. As discussed in Section 3.1, it is not unlikely that moving beyond the Boussinesq approximation could result in a somewhat larger overshoot depth than what we currently see in the simulations, simply because of the pressure-induced enhancement of the asymmetry between narrow downflows and broad upflows. In addition, since δ_{en} depends sensitively on $v_{\rm CZ}$, the reliability of our model predictions effectively depends on the reliability of mixing-length theory [11, 42] in estimating the typical velocities of convective motions deep within a star. Asteroseismology will hopefully help constrain the latter in the coming years. Nevertheless, it is difficult to see how the overshoot depth could vary substantially away from δ_{en} predicted using a simple energy balance argument. It is worth remembering at this point that Zahn's original models [160, 78] also predict a very shallow overshoot layer (in the strict definition

[1]Version 6794.

of the term) – but that layer only starts beyond a thermally-mixed penetration layer which can be much larger (at least for the smaller values of S). As such, our findings (in terms of strict overshoot) are not inconsistent with observations of substantial mixing beyond the edge of a convective region [88, 45], as long as these observations are interpreted as evidence for penetration (rather than overshoot).

As discussed in Section 3.5, estimating the amount of *thermal* mixing below the CZ (and therefore quantifying penetration) is much more complicated, as this requires knowledge not only of the velocities, but also of the typical temperature fluctuations associated with upflows and downflows relative to the background profile, which in turn depend on the relative importance of both small-scale horizontal turbulent mixing and thermal diffusion, as well as the global thermal equilibrium. This cannot be done using simple local energetic/thermal balance arguments, and it seems that the only way forward is to analyze the results of numerical simulations to create an empirical model for the heat flux. The problem with this approach, however, is that it is very sensitive to the model setup used (i.e. compressible vs. anelastic vs. Boussinesq, 2D vs. 3D, boundary conditions, method for generating the CZ-RZ transition), as noted by the rather vast discrepancies in results obtained in the numerical experiments discussed in Section 3.1. Further work will be required to better understand the causes of this sensitivity, and to determine what results can and cannot be carried over (qualitatively and quantitatively) from idealized models to more realistic stellar environments.

Within the scope of numerical simulations run in the same setup as ours, we could tentatively extrapolate our results to estimate the magnitude of the turbulent temperature flux $\bar{F}_T$ induced below r_t by the convective motions. However, we found that the latter only varies very weakly with Rayleigh number, to the extent that we are unable to propose any definite model for the former. If a power

law is assumed, then our results suggest that $\bar{F}_T \propto \mathrm{Ra}_o^{0.18}$. If that scaling holds, we predict that it may be possible to see convective penetration in Boussinesq convection at higher Rayleigh numbers (holding the Prandtl number constant). Indeed, taking our reference simulation ($\mathrm{Pr} = 0.1$, $S = 5$, $d_{out} = 0.003$, $\mathrm{Ra}_o = 10^7$) for instance, we see that the turbulent flux would have to be about 5 times larger than it is to drive the profile of $\bar{N}^2$ towards an adiabat below the base of the CZ, which would require an input Rayleigh number (defined as in Equation (3.11)) of the order of about 10^{11}. This is quite large, but may actually be achievable in the not-too-distant future[2] (especially if one were to use a reduced computational domain consisting of a wedge, rather than a full sphere).

[2]Recall that Ra_o is based on the lengthscale r_o rather than the width of the CZ, so the effective Rayleigh number of our simulations is smaller than Ra_o.

Table 3.1: Columns 1-7: Summary of all input parameters and resolution of our simulations. Column 8 reports on the lengthscale δ_G discussed in Section 3.3. Column 9 reports on the lengthscale δ_{en} discussed in Section 3.4. Column 10 reports on the lengthscale δ_Θ discussed in Section 3.3, and column 11 reports on δ_u discussed in Section 3.3.

Case #	S	d_{out}	d_{in}	Ra_o	Pr	$N_r \times N_\theta \times N_\phi$	δ_G	δ_{en}	δ_Θ	δ_u
1	100	0.0003	0.03	10^6	0.1	350×192×192	0.020	0.017	0.059	0.048
2	5	0.003	0.015	10^6	0.1	300×192×192	0.060	0.045	0.150	0.130
3	10	0.003	0.03	10^6	0.1	300×192×192	0.049	0.039	0.130	0.100
4	20	0.003	0.06	10^6	0.1	300×192×192	0.044	0.037	0.110	0.092
5	2	0.01	0.02	10^6	0.1	300×192×192	0.096	0.069	0.240	0.220
6	5	0.01	0.05	10^6	0.1	300×192×192	0.071	0.057	0.170	0.150
7	10	0.01	0.1	10^6	0.1	300×192×192	0.064	0.054	0.150	0.130
8	5	0.03	0.15	10^6	0.1	300×192×192	0.091	0.078	0.220	0.190
9	10	0.03	0.3	10^6	0.1	300×192×192	0.089	0.077	0.210	0.190
10	5	0.05	0.25	10^6	0.1	300×192×192	0.104	0.091	0.260	0.230
11	5	0.003	0.015	10^7	0.1	400×288×320	0.047	0.034	0.110	0.094
12	10	0.003	0.03	10^7	0.1	400×288×320	0.038	0.030	0.090	0.075
13	20	0.003	0.06	10^7	0.1	400×288×320	0.035	0.029	0.085	0.070
14	5	0.01	0.05	10^7	0.1	400×288×320	0.057	0.045	0.140	0.120
15	10	0.01	0.1	10^7	0.1	400×288×320	0.052	0.043	0.120	0.104
16	5	0.03	0.15	10^7	0.1	400×288×320	0.077	0.062	0.170	0.150
17	10	0.03	0.3	10^7	0.1	400×288×320	0.075	0.062	0.170	0.150
18	5	0.05	0.25	10^7	0.1	400×288×320	0.090	0.073	0.200	0.180
19	5	0.003	0.015	10^8	0.1	585×516×640	0.035	0.026	0.080	0.069
20	10	0.003	0.03	10^8	0.1	585×516×640	0.030	0.024	0.068	0.058
21	20	0.003	0.06	10^8	0.1	585×516×640	0.028	0.024	0.063	0.054
22	5	0.01	0.05	10^8	0.1	585×516×640	0.045	0.036	0.097	0.089
23	10	0.01	0.1	10^8	0.1	585×516×640	0.043	0.035	0.094	0.085
24	5	0.03	0.15	10^8	0.1	585×516×640	0.063	0.050	0.140	0.120
25	10	0.03	0.3	10^8	0.1	585×516×640	0.062	0.050	0.130	0.120

Chapter 4

On the dynamics of the interaction of convective motions with a dipolar primordial magnetic field

4.1 Introduction

In Chapter 2, we studied stellar convective dynamics in a Boussinesq spherical shell, by accounting for a non-zero adiabatic temperature gradient and using fixed flux inner boundary condition, in the low-Prandtl number regime. Then, in Chapter 3, we extended the problem to include a stably stratified radiative zone below the unstable convection zone and focused on the study of overshooting convection. In this chapter, we are interested in exploring how these turbulent motions interact with a primordial dipole magnetic field initially contained in the radiative zone, and whether they can confine the magnetic field in the stable region.

As explained in Chapter 2, the existence of a primordial field within the radiative zone appears to be the only way to explain why the latter is in uniform rotation. Furthermore, its confinement strictly below the base of the differentially rotating convection zone is crucial to avoid the propagation of the latitudinal shear inward through the Ferraro's law of isorotation ([49, 89]). The GM98 model claims to explain the field confinement by having self-consistently generated meridional flows in the CZ whose advection balances the outward diffusion of the field.

There have been many attempts to reproduce the GM98 model dynamics numerically, starting from Garaud (2002) [54] who studied the problem assuming a steady-state, axisymmetry and no stratification, and she found that uniform rotation was possible for a small range of magnetic field strengths. Later, Brun & Zahn (2006) [25] ran 3D, global anelastic simulations where they only modeled the radiative zone including a poloidal field. The RZ started in uniform rotation but a differentially rotating upper boundary condition was applied. Their initially confined field eventually diffused upward, becoming "unconfined". Later, Strugarek et al. (2011) [139], added the missing convection zone to their model but they still did not observe any long-term confinement of the magnetic field. As in Brun & Zahn (2006) [25], the field diffused outward into the convection zone, leading to the propagation of the differential rotation in the stable radiative zone. Also, Rogers (2011) [119] ran axisymmetric simulations and found a similar result.

As argued by Acevedo-Arreguin et al. (2013) [1], all the above numerical investigations failed to reproduce the GM98 model because they were run in the wrong parameter regime. Earlier, Garaud & Garaud (2008) [55] had shown that given the correct parameter space, the meridional flows should be able to confine the primordial field. However they performed 2.5D, quasi-steady state simulations of the radiative zone only. Acevedo-Arreguin et al. (2013) [1] ran 2.5D steady-state

axisymmetric MHD simulations including a simple model for the convective region and they found that in the parameter regime used by Strugarek et al. (2011) [139], the magnetic confinement is impossible, and that the differential rotation propagates into the RZ, while the angular momentum balance is between the viscous stresses and the Lorentz force. This should not be the case since viscous effects should be negligible in the Sun. Acevedo-Arreguin et al. (2013) demonstrated that operating in the right parameter regime, where viscosity is unimportant, leads to a confined magnetic field and a uniform angular velocity in the RZ. More recently, Wood & Brummell (2018) [157] performed 3D compressible MHD simulations in a Cartesian domain which included both the primordial magnetic field in the RZ and the meridional circulation generated via forced differential rotation in the CZ. They showed that the field can indeed be confined in the RZ by the mean meridional flows, while the uniform rotation is maintained in the RZ. They also found that turbulent convection had little effect on the mean field which was controlled by the meridional flows. They showed that a self-consistently thin tachocline formed, which in the absence of the magnetic field would have thickened and eventually extended deeper in the radiative zone. However, the study was done in an artificial geometry of a Cartesian box (local model) and with an artificially forced differential rotation in the CZ, hence the need for global simulations in 3D spherical geometries where the differential rotation is self-consistently generated still remains.

In all of these previous models, the CZ was assumed to rotate differentially, since these studies were explicitly trying to model the GM98 dynamics in which the meridional circulation plays a crucial role in the magnetic field confinement. A big question is what is the role of non-rotating effects on the confinement of the field. Could for instance convective turbulence help or actually hinder

this process? Thus, in this chapter, we focus on the possible confinement of the dipole field solely by the overshooting motions without including any angular momentum transport associated with rotation. Garaud and Rogers (2007) [56] ran 2D simulations of this process in a spherical geometry and found that the large-scale dipolar field could be partially confined by the turbulent motions in the CZ while the magnetic energy was transferred to small-scales in the CZ. Kitchatinov & Rüdiger (2008) [83] studied the problem of a large-scale field confinement using a simple diamagnetic pumping prescription. The latter is associated with the transport of magnetic field down a gradient of turbulent intensity, i.e. in the direction of decreasing turbulence, which can be enforced through an enhanced turbulent diffusion in one region (within the CZ) and a smaller diffusivity in the other (within the RZ). They found that the magnetic field could be confined for sufficiently strong pumping.

Another interesting idea on the interaction between a magnetic field and convection which could lead to the confinement of the field was given by Weiss (1966) [156], who showed that magnetic flux gets expelled from regions that are more turbulent and becomes concentrated at the edges of the convective eddies, a phenomenon often called "magnetic flux expulsion". This is a special case of turbulent diffusion for regions with circular streamlines which acts in the middle of the cell leading to an accumulation of the magnetic field at the edges. Finally, another mechanism that could also help with the magnetic field confinement is "topological pumping" (e.g. [143, 144]), whereby there is advective mean transport of the field due to asymmetries in the upflows and the downflows that stem from compressibilty or geometrical effects, for instance. Thus, a magnetic field in the RZ that diffuses upwards into the CZ and interacts with the convective motions could be pumped back into the stable region by the turbulent overshooting motions.

We are interested in exploring these dynamics as well.

This chapter is organized as follows: In Section 4.2 we present the model setup along with the initial and boundary conditions. In Section 4.3, we concentrate on the simulations for which were not dynamos, and we demonstrate that the magnetic field cannot be confined by the overshooting motions. In Section 4.4, we focus on the numerical experiments for which a dynamo field was generated and we study the dynamics associated with the overshooting motions and the dynamo field. Finally, in Section 4.5, we conclude with a summary of the results of this chapter.

4.2 Model Setup

The model configuration in this chapter is similar to the one we used in Chapter 3 except that we now include magnetic fields. They are evolved in time using the induction equation and act on the fluid through the Lorentz force in the momentum equation. We use the same two-layered system that consists of a convectively stable region for $r \in [0.2r_o, 0.7r_o)$ and an unstable one for $r \in [0.7r_o, r_o]$. Restarting from the end of one of the thermally equilibrated purely hydrodynamic simulations presented in Chapter 3, we now initialize it with a poloidal magnetic field

$$\boldsymbol{B}_p = B_0 \nabla \times \nabla \times ((\sin(cr)/(cr)^2) - \cos(cr)/(cr))\sqrt{3}\cos\theta r \mathbf{e}_r) \qquad (4.1)$$

confined in the stable zone, where B_0 sets the amplitude of the initial magnetic field and c is a constant equal to $c \approx 6.91$. From here on, we solve the MHD Navier-Stokes equations under the Boussinesq approximation where we continue to assume constant thermal expansion coefficient α, viscosity ν, thermal diffusivity κ, adiabatic temperature gradient $dT_{\rm ad}/dr$, gravity g, as before

and also assume a constant magnetic diffusivity η. As before, we let $T(r,\theta,\phi,t) = T_{\rm rad}(r) + \Theta(r,\theta,\phi,t)$ where $T_{\rm rad}$ is the temperature profile our system would have under pure radiative equilibrium, and where Θ describes temperature fluctuations away from it. Due to the Boussinesq approximation, there is a linear relationship between the temperature and density perturbations such that $\rho/\rho_m = -\alpha\Theta$, where ρ_m is the mean density of the background fluid. Then, the MHD governing Boussinesq equations are:

$$\nabla \cdot \boldsymbol{u} = 0, \tag{4.2}$$

$$\frac{\partial \boldsymbol{u}}{\partial t} + \boldsymbol{u}\cdot\nabla\boldsymbol{u} = -\frac{1}{\rho_m}\nabla p + \alpha\Theta g\boldsymbol{e_r} + \frac{1}{\rho_m}\mathbf{j}\times\boldsymbol{B} + \nu\nabla^2\boldsymbol{u}, \tag{4.3}$$

$$\nabla \cdot \boldsymbol{B} = 0, \tag{4.4}$$

$$\frac{\partial \boldsymbol{B}}{\partial t} - \nabla\times(\boldsymbol{u}\times\boldsymbol{B}) = \eta\nabla^2\boldsymbol{B}, \tag{4.5}$$

and

$$\frac{\partial \Theta}{\partial t} + \boldsymbol{u}\cdot\nabla\Theta + u_r\left(\frac{dT_{\rm rad}}{dr} - \frac{dT_{\rm ad}}{dr}\right) = \kappa\nabla^2\Theta, \tag{4.6}$$

where $\boldsymbol{u} = (u_r, u_\theta, u_\phi)$ is the velocity field, $\boldsymbol{B} = (B_r, B_\theta, B_\phi)$ is the magnetic field, $\mathbf{j} = \dfrac{1}{\mu_0}\nabla\times\boldsymbol{B}$ is the current density, μ_0 is the vacuum permeability, and p is the pressure perturbation away from hydrostatic equilibrium.

We non-dimensionalize the problem by using $[l] = r_o$, $[t] = r_o^2/\nu$, $[u] = \nu/r_o$, $[B] = B_0$ and $[T] = |dT_o/dr - dT_{\rm ad}/dr|r_o$ as the unit length, time, velocity, magnetic field and temperature respectively, where $dT_o/dr \equiv dT_{\rm rad}/dr|_{r=r_o}$ is the radiative temperature gradient at the outer boundary. Then, we can write the non-dimensional equations as:

$$\nabla \cdot \boldsymbol{u} = 0, \tag{4.7}$$

$$\frac{\partial \boldsymbol{u}}{\partial t} + \boldsymbol{u}\cdot\nabla\boldsymbol{u} = -\nabla p + \frac{\mathrm{Ra}_o}{\mathrm{Pr}}\Theta\boldsymbol{e_r} + Q(\nabla\times\boldsymbol{B}\times\boldsymbol{B}) + \nabla^2\boldsymbol{u}, \tag{4.8}$$

$$\nabla \cdot \boldsymbol{B} = 0, \tag{4.9}$$

$$\frac{\partial \boldsymbol{B}}{\partial t} - \nabla \times (\boldsymbol{u} \times \boldsymbol{B}) = \frac{1}{\mathrm{P}_m} \nabla^2 \boldsymbol{B}, \tag{4.10}$$

$$\frac{\partial \Theta}{\partial t} + \boldsymbol{u} \cdot \nabla \Theta + \beta(r) u_r = \frac{1}{\mathrm{Pr}} \nabla^2 \Theta. \tag{4.11}$$

In all that follows, all the variables and parameters are implicitly non-dimensional. The Prandtl number Pr and the global Rayleigh Ra_o are defined as in Equation (3.11) and the function $\beta(r)$ is given by Equation (3.13). The addition of the magnetic field introduces the Chandrasekhar number that characterizes the relative importance of the Lorentz force to the viscous force and is given by

$$Q = \frac{B_0^2 r_o^2}{\mu_0 \rho_m \nu^2}. \tag{4.12}$$

It also introduces the magnetic Prandtl number

$$\mathrm{P}_m = \frac{\nu}{\eta}. \tag{4.13}$$

The boundary conditions for the temperature and the velocity fields are the same as the ones used in Chapters 2 and 3, i.e. fixed flux at the inner boundary and fixed temperature at the outer boundary while for the velocity field we employ stress-free boundary conditions. For the magnetic field, we assume a conducting inner core and an electrically insulating outer boundary.

Our simulations are performed for a stiffness parameter $S = 5$, a transition width $d_{out} = 0.003$ and for a fixed Pr= 0.1. Also, in all of our simulations, we take the Chandrasekhar number to be equal to $Q = 0.01$, since we are interested first in establishing how the overshooting turbulent motions can affect a weak magnetic field. However, we consider two different magnetic Prandtl numbers P_m (namely $\mathrm{P}_m = 0.1$ and $\mathrm{P}_m = 1$), and four different Ra_o ($\mathrm{Ra}_o = 10^6$, 10^7, 10^8, and

$\mathrm{Ra}_o = 10^9$). These values are much larger (for P_m) and smaller (for Ra_o) than the corresponding solar values, owing to the computational limitations placed by the required spatial and temporal resolution of the simulations.

4.3 Non-Dynamo simulations

In this section, we first look at the simulations with $\mathrm{P}_m = 0.1$ for $S = 5$, $d_{out} = 0.003$ and Pr= 0.1. We focus on understanding the interaction of the initially contained poloidal dipolar magnetic field in the RZ with the turbulent motions in the overshoot region and the CZ. The main question we want to answer is whether the dipole field can remain confined solely by these 3D turbulent motions, as suggested might be possible by previous models (e.g. [144, 56]).

Figure 4.1 qualitatively illustrates how the initial dipole field behaves with time. Contours of the dipole poloidal field lines are plotted along with the axisymmetric B_ϕ for a typical simulation of $\mathrm{Ra}_o = 10^7$ at different representative times to show the evolution of the field. At $t \approx 0.0002$, the field has diffused outward somewhat to come into contact with the overshooting convection and by the time $t \approx 0.014$, the field lines have opened up in the whole CZ leading to the appearance of an unconfined configuration. By "unconfined" here, we mean "open field lines" or lack of closed loop field lines as in the initial configuration, i.e. a state which is a long way away from the initial one and has a significant signature in the CZ. Associated with the evolving geometry of the poloidal field, we also see that the overall amplitude of the field is decaying rapidly with time. Indeed, at $t \approx 0.0002$, B_ϕ is of order unity, but decreases by five orders of magnitude by time $t \approx 0.054$.

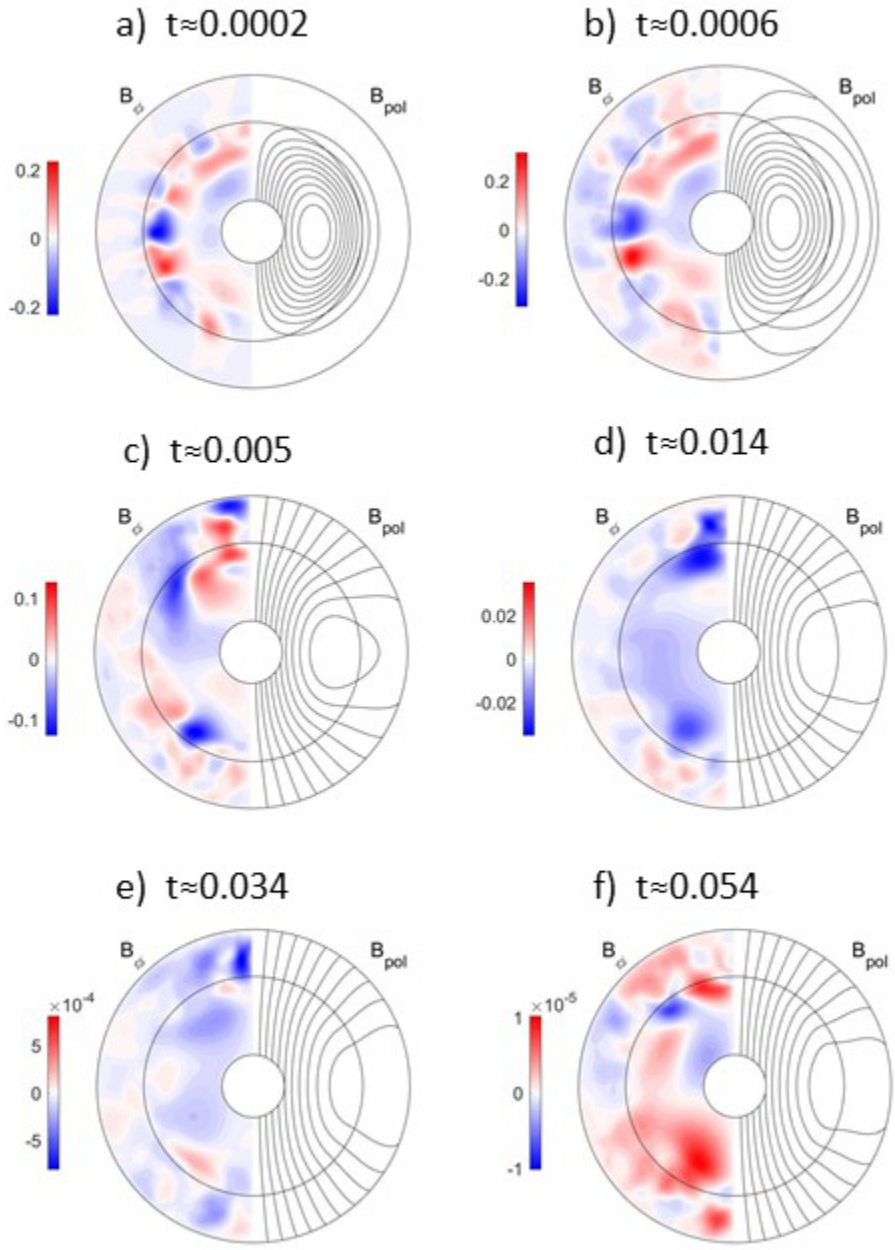

Figure 4.1: Contours of B_ϕ and the dipole B_{pol} in six different times for the run with $\mathrm{Ra}_o = 10^7$.

These results are contrary to the results of Garaud & Rogers (2007) [56] who found that the magnetic field could be confined by the turbulent motions in their

axisymmetric spherical simulations. The reason behind this discrepancy is that in 2D, the convective motions in the CZ are less turbulent than in 3D, and are characterized by large-scale axisymmetric rolls. Such laminar large-scale eddies have large (axisymmetric) regions of strong downflows, as compared to the smaller filling factor of 3D plumes, and therefore can topologically pump field more easily. To visualize this in a better way, in Figure 4.2, we present snapshots of 3D meridional slices for both the magnetic field and the velocity field at time $t \approx 0.033$ for the $\mathrm{Ra}_o = 10^7$ case, in order to show the more detailed features of the full fields (and not just the axisymmetric component). We clearly see that the convection zone in our 3D calculation is characterized by a wider range of eddy-scale sizes, unlike the large-scale rolls typical in 2D calculations. This more chaotic nature of the convective region found in the more realistic 3D simulations does not help but actually hinders the confinement of the magnetic field, although it worked in 3D Cartesian simulations of Tobias et al. [143, 144].

Finally note that the convection in these simulations remains essentially unaffected by the field, since the latter is initially small, and generally decays with time.

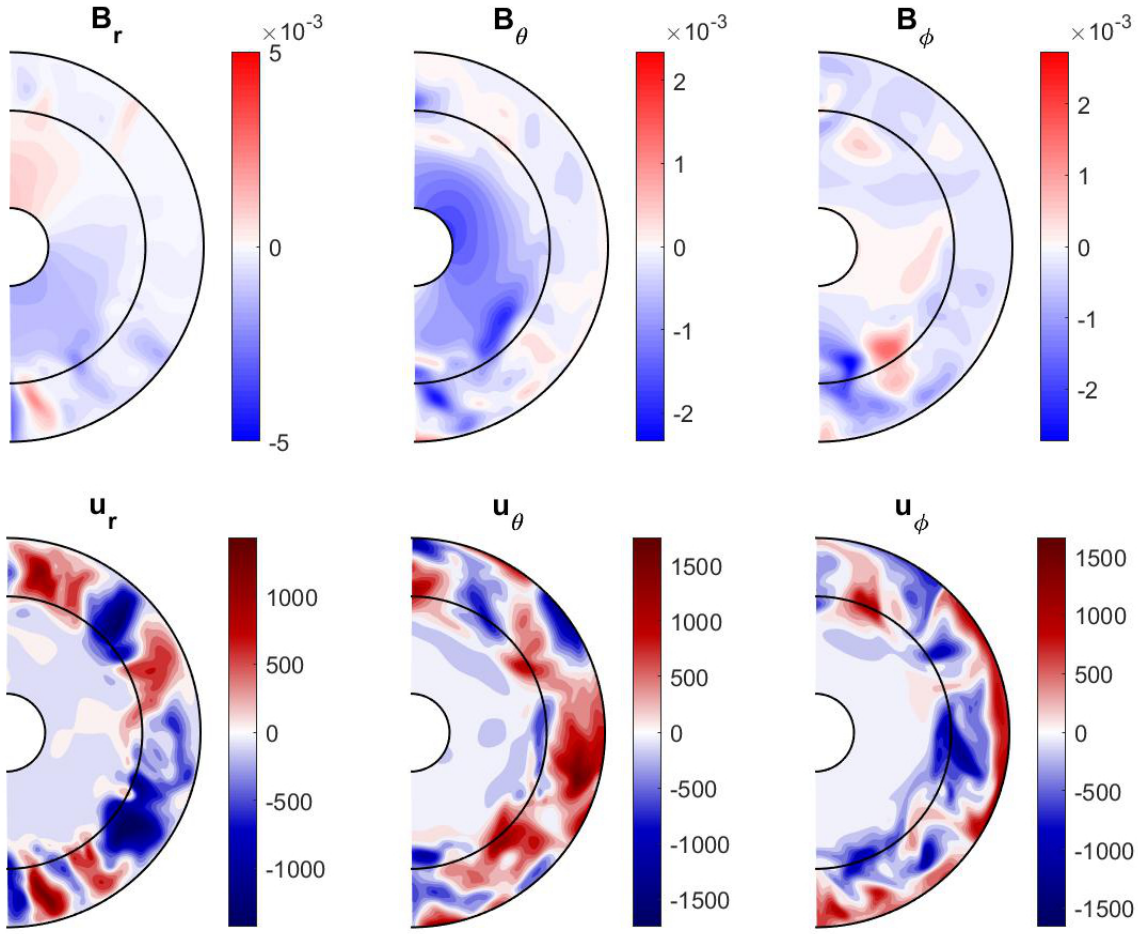

Figure 4.2: Snapshots of meridional slices of the magnetic fled components B_r, B_θ, and B_ϕ and the velocity fled components u_r, u_θ, and u_ϕ at $t = 0.033$ for the run with $\mathrm{Ra}_o = 10^7$.

We now focus on more quantitative characteristics. In all that follows, we define the spherical average of a quantity q as

$$\bar{q}(r) = \frac{1}{4\pi} \int_0^{2\pi} \int_0^{\pi} q(r, \theta, \phi) \sin\theta d\theta d\phi. \tag{4.14}$$

We also define the non-dimensional magnetic energy as $E_m = (Q/2)(B_r^2 + B_\theta^2 + B_\phi^2)$.

We first compare the evolution of the initial dipole field to what one would expect if there was no convection zone in the system, in order to examine the

effect of the convection. In the absence of any fluid motion, the initial magnetic field would simply diffuse out with time according to

$$\frac{\partial \boldsymbol{B}}{\partial t} = \eta \nabla^2 \boldsymbol{B}, \tag{4.15}$$

since η is constant. This equation can be solved semi-analytically (see Appendix). In Fig. 4.3, we compare the radial variation of the magnetic energy of the purely diffusive case to the non-dimensional magnetic energy in the dipole component of the magnetic field in the fully nonlinear simulation $\bar{E}_{dip}(r)$, in order to identify how the dipolar field is affected by its interaction with the turbulent motions. These energies are plotted versus r at the same six different times shown in Fig. 4.1. We see that initially the energies coincide in the RZ, but at later times, $\bar{E}_{dip}(r)$ has decreased much faster than the purely diffusive case at all radii, especially after $t \approx 0.014$.

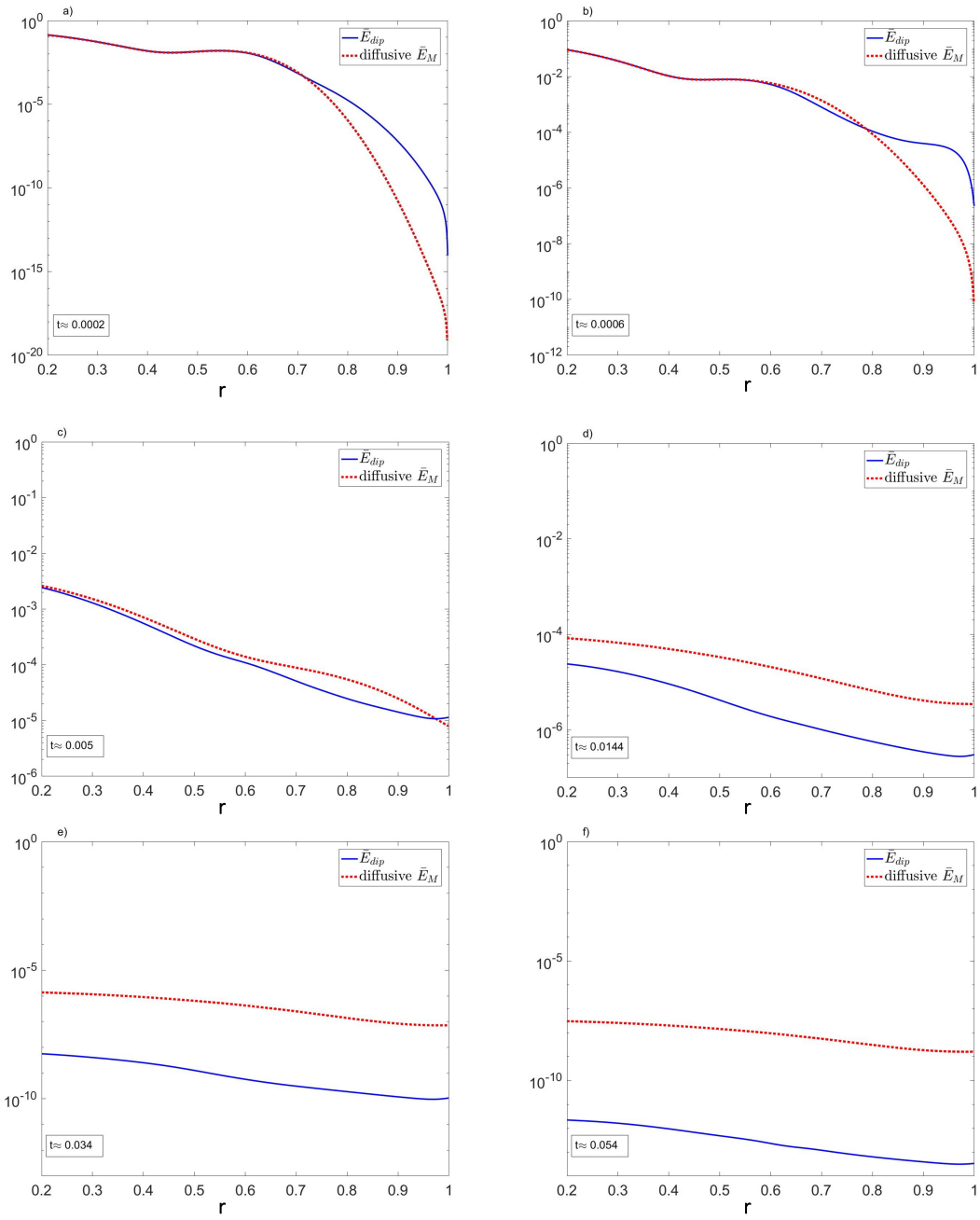

Figure 4.3: Non-dimensional magnetic energy of the dipole $\bar{E}_{dip}(r)$ plotted along with the magnetic energy of the purely diffusive case against the radius r for the case of $\mathrm{Ra}_o = 10^7$ at time a) $t \approx 0.0002$, b) $t \approx 0.0006$, c) $t \approx 0.005$, d) $t \approx 0.014$, e) $t \approx 0.034$, and f) $t \approx 0.054$.

This significant and rapid loss of energy in the dipole (compared to the purely diffusive case) could potentially be attributed to Tayler instabilities (e.g. [93, 159, 136, 13]) but it turns out that this is not the case here. It has been found that a purely poloidal field with closed field lines within a stable radiative zone is unstable to non-axisymmetric perturbations, and these MHD instabilities can lead to a substantial reduction of the magnetic flux. However, we did not observe any such instability due to the fact that our initial field is too weak. The Alfvénic timescale at which the instability occurs is $t_A = r_o^2/\sqrt{\nu Q} = 1/\sqrt{0.01} = 10$ which is longer than both the magnetic diffusion timescale and the thermal diffusion timescale in our system given by $t_\eta = r_o^2/\eta = 0.1$, and $t_\kappa = r_o^2/\kappa = 0.1$, respectively. We therefore instead attribute the loss of the dipole magnetic energy to the enhanced turbulent diffusivity from the turbulent motions.

In an attempt to quantify the effect of turbulent diffusion on the dipole energy, we numerically solve the diffusion equation

$$\frac{\partial \boldsymbol{B}}{\partial t} = \nabla \times (\eta \nabla \times \boldsymbol{B}), \tag{4.16}$$

for a varying magnetic diffusivity profile $\eta(r)$ given by:

$$\eta(r) = 10 + 0.5\eta_T(\tanh((r - 0.7)/\delta) + 1), \tag{4.17}$$

where we use $\delta = 0.1$, which is approximately equal to the depth down to which the strongest of the downflows overshoot, as calculated for this simulation in Chapter 3 (see Fig. 4.4).

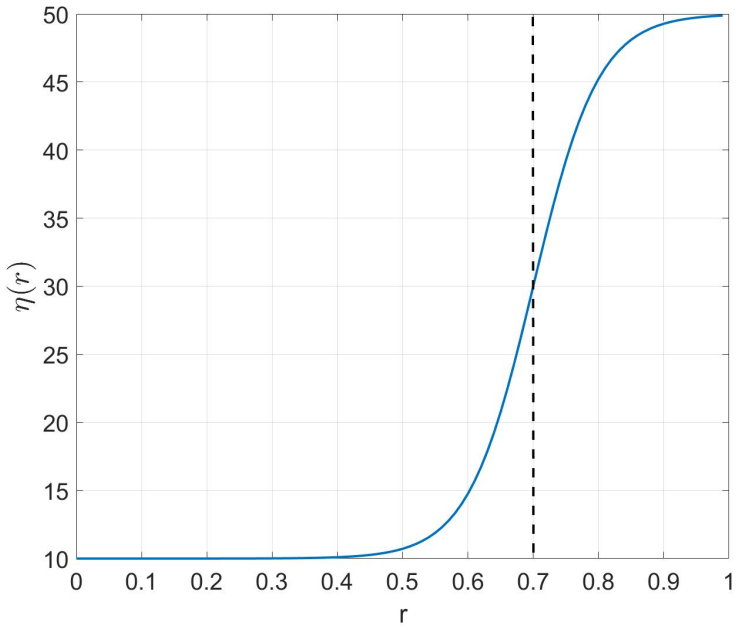

Figure 4.4: Profile of $\eta(r)$ versus r as given in Eq. (4.17), for $\delta = 0.1$ and $\eta_T = 40$.

We then vary η_T until we find a reasonable match to the numerical solution for the non-dimensional dipole magnetic energy for the simulation with $\mathrm{Ra}_o = 10^7$. We find that this happens when $\eta_T \approx 40$, i.e. when the magnetic turbulent diffusivity η is approximately 5 times larger in the CZ than in the RZ (see Figure 4.5). That demonstrates that the results achieved in the simulation can be adequately interpreted as an increased (turbulent) diffusivity in the CZ and the overshoot zone.

Unfortunately, it is difficult at this point to compare the simulations of the different Rayleigh numbers to one another and obtain the desirable dependence of the turbulent diffusivity η_T on Ra_o. That is due to the fact that the two higher Rayleigh number cases of $\mathrm{Ra}_o = 10^8$ and $\mathrm{Ra}_o = 10^9$ have not evolved long in time (compared to $\mathrm{Ra}_o = 10^7$).

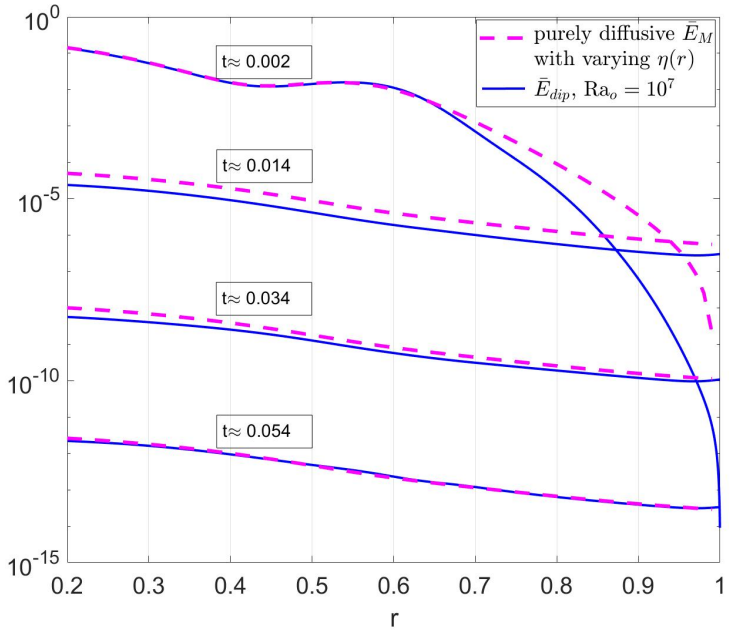

Figure 4.5: Plot of $\bar{E}_{dip}(r)$ for the $\mathrm{Ra}_o = 10^7$ case along with the purely diffusive solution with a varying $\eta(r)$ profile given by Eq. (4.17) for $\eta_T = 40$ and $\delta = 0.1$.

Another way of establishing that the convection acts as a turbulent diffusivity for the magnetic field at these parameters is to look at the radial distribution of the dipole field between the CZ and the RZ for the different Ra_o cases and the purely diffusive ones. In Figure 4.6, we plot the fractional magnetic energy of the dipole in the RZ, E_{dip-RZ} and in the CZ, E_{dip-CZ} (where the dipole energy in each zone has been normalized by the total dipole energy over both zones) versus time, for the runs with $\mathrm{Ra}_o = 10^7$ and $\mathrm{Ra}_o = 10^8$. We define E_{dip-RZ} and E_{dip-CZ} as

$$E_{dip-RZ} = \frac{\int_{r_i}^{r_t} (\bar{E}_{dip} r^2 dr)}{\int_{r_i}^{r_o} (\bar{E}_{dip} r^2 dr)}, \tag{4.18}$$

and

$$E_{dip-CZ} = \frac{\int_{r_t}^{r_o} (\bar{E}_{dip} r^2 dr)}{\int_{r_i}^{r_o} (\bar{E}_{dip} r^2 dr)}, \tag{4.19}$$

respectively. We also plot the respective fractional dipole energies for the purely diffusive case with a constant $\eta = 10$ given by Eq. (4.15), as well as the ones of the purely diffusive case with the varying $\eta(r)$ given by Eq. (4.16) We first notice that E_{dip-RZ} initially decreases and at the same time E_{dip-CZ} starts increasing, which corresponds to the initial stages of the simulation where the internal dipole field begins to diffuse into the convection zone. Interestingly however, around $t = 0.01$, E_{dip-RZ} and E_{dip-CZ} asymptote to two constants where $E_{dip-RZ} > E_{dip-CZ}$, suggesting that the system has adjusted to a new radial eigenmode, one consistent with having a larger magnetic diffusivity in the CZ than in the RZ. Indeed, we can compare these results with the corresponding E_{dip-RZ} of the purely diffusive case with the varying $\eta(r)$ profile, and see that they coincide. Hence, indeed a larger magnetic turbulent diffusivity in the CZ can have a similar effect as the turbulent diffusion by the convective motions on the magnetic energy of the dipole field. We notice that E_{dip-RZ} is much larger for $\mathrm{Ra}_o = 10^7$ and $\mathrm{Ra}_o = 10^8$ than the purely diffusive case with a constant $\eta = 10$. Moreover, although the $\mathrm{Ra}_o = 10^8$ case has not run long enough to give a definite result, it looks like the relative amount of energy in the CZ is much smaller than in the $\mathrm{Ra}_o = 10^7$ case, which is consistent with the notion that the turbulent diffusion might be higher for higher Ra_o.

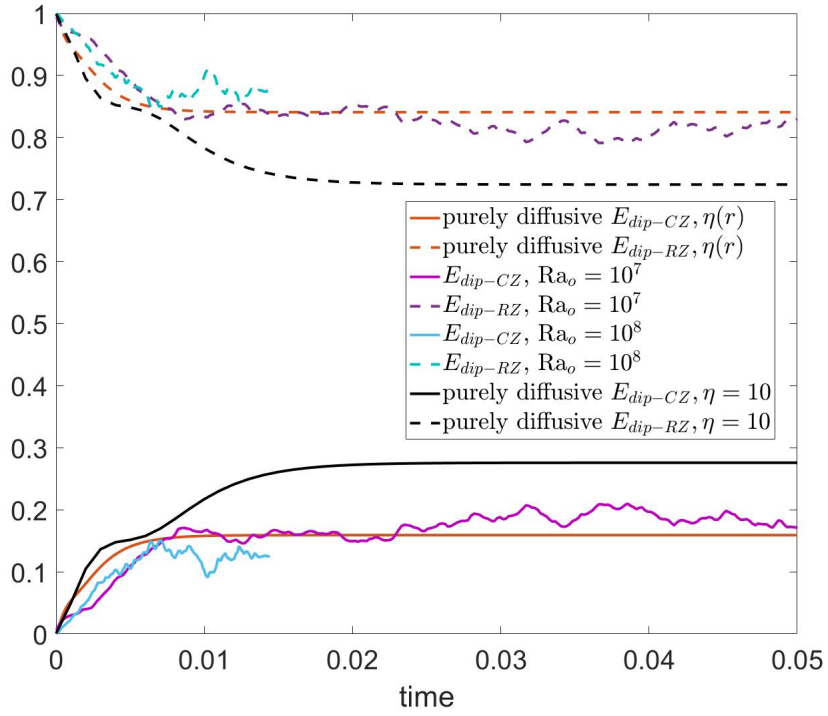

Figure 4.6: Plot of E_{dip-RZ} and E_{dip-CZ} for the runs with $\mathrm{Ra}_o = 10^7$ and $\mathrm{Ra}_o = 10^8$ along with the purely diffusive ones of both the constant $\eta = 10$ case and the varying $\eta(r)$ case.

Beyond promoting the decay of the original primordial dipolar field, the convection zone also acts to generate smaller-scale magnetic fields in both poloidal and toroidal direction. This can be seen in Figure 4.7 where we plot the total non-dimensional magnetic energy $E_M(t) = \dfrac{Q}{2V}\int_V (B_r^2 + B_\theta^2 + B_\phi^2)dV$ (where V is the volume of the spherical shell) along with the poloidal and the toroidal magnetic energy, $E_p(t) = \dfrac{Q}{2V}\int_V (B_r^2 + B_\theta^2)dV$ and $E_t(t) = \dfrac{Q}{2V}\int_V (B_\phi^2)dV$, respectively as well as the poloidal and toroidal axisymmetric magnetic energy $E_{pa}(t)$ and $E_{ta}(t)$, respectively, for the case with $\mathrm{Ra}_o = 10^7$ (Fig.4.7 (a)) and $\mathrm{Ra}_o = 10^8$ (Fig.4.7 (b)). We notice that the energy in the non-axisymmetric modes very rapidly increases as the field starts diffusing into the convection zone. This initially leads to an increase in the total energy $E_M(t)$ compared with the pure dipolar solution (i.e.

between $t \approx 0.0001$ and $t \approx 0.01$), and most of the energy is now in the non-dipole and non-axisymmetric modes. However, the inductive action of the flow is not strong enough to overcome diffusion and the field decays. Indeed, we see that $E_M(t)$ decreases rapidly on a timescale approximately equal to 0.005 which is approximately 2 times faster than the purely diffusive case, and which corresponds to the timescale obtained earlier assuming that η jumps to a turbulent value of 50 in the CZ. For the more turbulent case of $\mathrm{Ra}_o = 10^8$ (Fig.4.7 (b)), the transient amplification rate of the field in the CZ is more pronounced than the $\mathrm{Ra}_o = 10^7$ case. However, this system is not a dynamo since the magnetic field, although transiently amplified in the CZ and overshoot region, is not maintained against diffusion and decays. It is perhaps interesting to cast this system in the stoked dynamo framework of Byington et al. (2014) [27]. Since the regions of magnetic field and fluid motions are initially separated, if one considers the convective part alone, it would be classified as a stoked non-dynamo, since field is leaked (or stoked) into the convective part of the system. That is, despite the initial amplification of the stoked field when it interacts with the turbulent motions, that CZ does not operate as a dynamo.

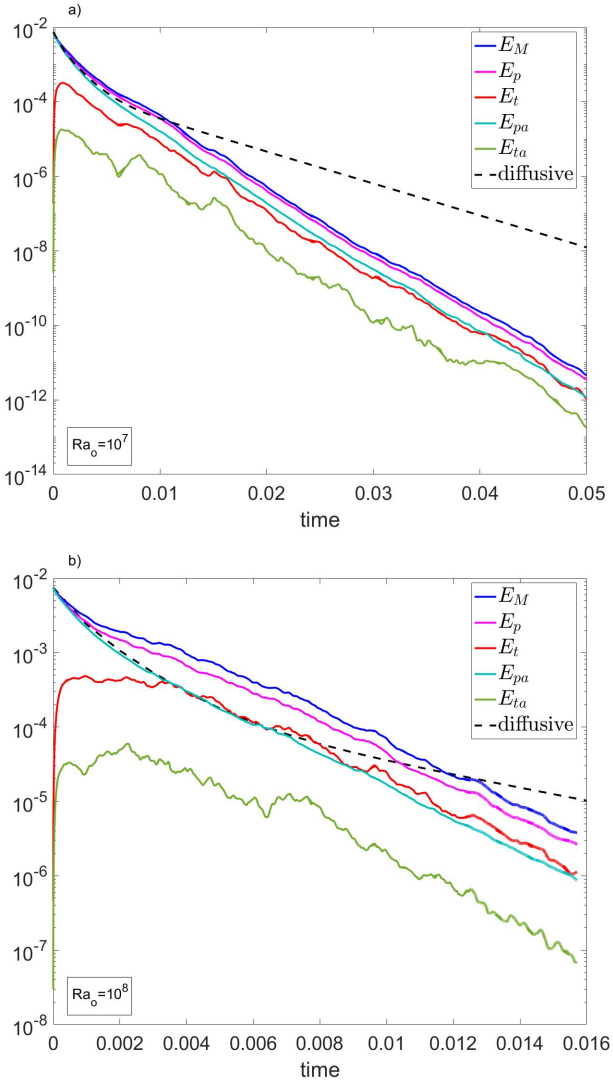

Figure 4.7: Magnetic energy profiles versus time for $\mathrm{P}_m = 0.1$ and a) $\mathrm{Ra}_o = 10^7$, and b) $\mathrm{Ra}_o = 10^8$.

4.4 Dynamo simulations

We will investigate now the higher P_m cases where the dynamics are substantially different. In this section we focus on the results of two simulations in which the convection zone was found to operate as a small-scale essentially kinematic dynamo. These simulations have parameters $\mathrm{P}_m = 1$, and $\mathrm{Ra}_o = 10^7$ and $\mathrm{Ra}_o = 10^8$

respectively (for $S = 5$, $d_{out} = 0.003$ and Pr= 0.1). We also ran a simulation at the same Pr, P_m, S and d_{out}, but with a smaller value of $\mathrm{Ra}_o = 10^6$, and found that it is not a dynamo. That implies that for a magnetic $\mathrm{P}_m = 1$ (along with the other parameters used in this setup), the critical Rayleigh number for the dynamo action to occur is some value between $\mathrm{Ra}_o = 10^6$ and $\mathrm{Ra}_o = 10^7$.

In Figure 4.8, we present contours of the axisymmetric poloidal field B_{pol} at a given time along with the axisymmetric B_ϕ, as well as u_{pol} along with the axisymmetric u_ϕ (similarly to Fig. 4.1). The snapshots are taken early in the calculation at $t \approx 0$ and then later in time at $t \approx 0.002$, $t \approx 0.006$ and $t \approx 0.0135$, for both $\mathrm{Ra}_o = 10^7$ (Fig. 4.8 (a)-(d)) and $\mathrm{Ra}_o = 10^8$ (Fig. 4.8 (e)-(h)). We observe that as the magnetic field starts diffusing upward into the unstable CZ, the turbulent motions interact with the field and amplify it. Simultaneously, the amplitude of the field decays substantially deep within the RZ. Comparing the snapshots of u_ϕ and B_ϕ, we clearly see that the characteristic lengthscale of the magnetic field in the CZ is significantly smaller than that of the dominant turbulent eddies, and decreases as Ra_o increases. This can be more clearly seen in Fig. 4.9, where we present snapshots of 3D meridional slices of the velocity components and the magnetic field components (instead of the axisymmetric components). Figures 4.8 and 4.9 show quite different dynamics than Fig. 4.1 and 4.2, due to the amplification of the small-scale magnetic field in these cases compared to the turbulent diffusion of the field (perhaps after some transient amplification) in the previous cases.

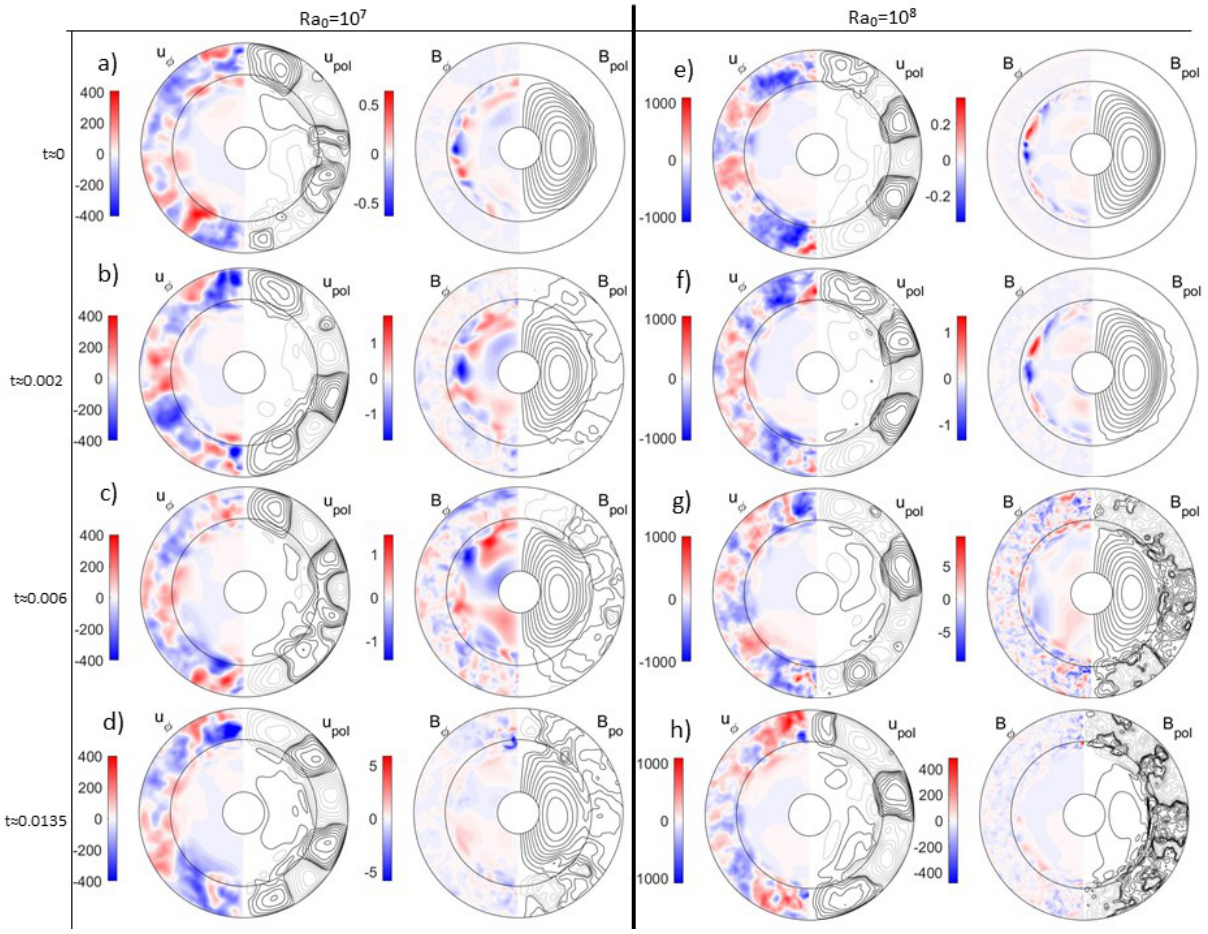

Figure 4.8: Snapshots of contours of u_ϕ, u_{pol} (on the left part), and B_ϕ, B_{pol} (on the right part) in an increasing time order for four typical times for $\mathrm{Ra}_o = 10^7$ ((a)-(d)) and for $\mathrm{Ra}_o = 10^8$ ((e)-(h)).

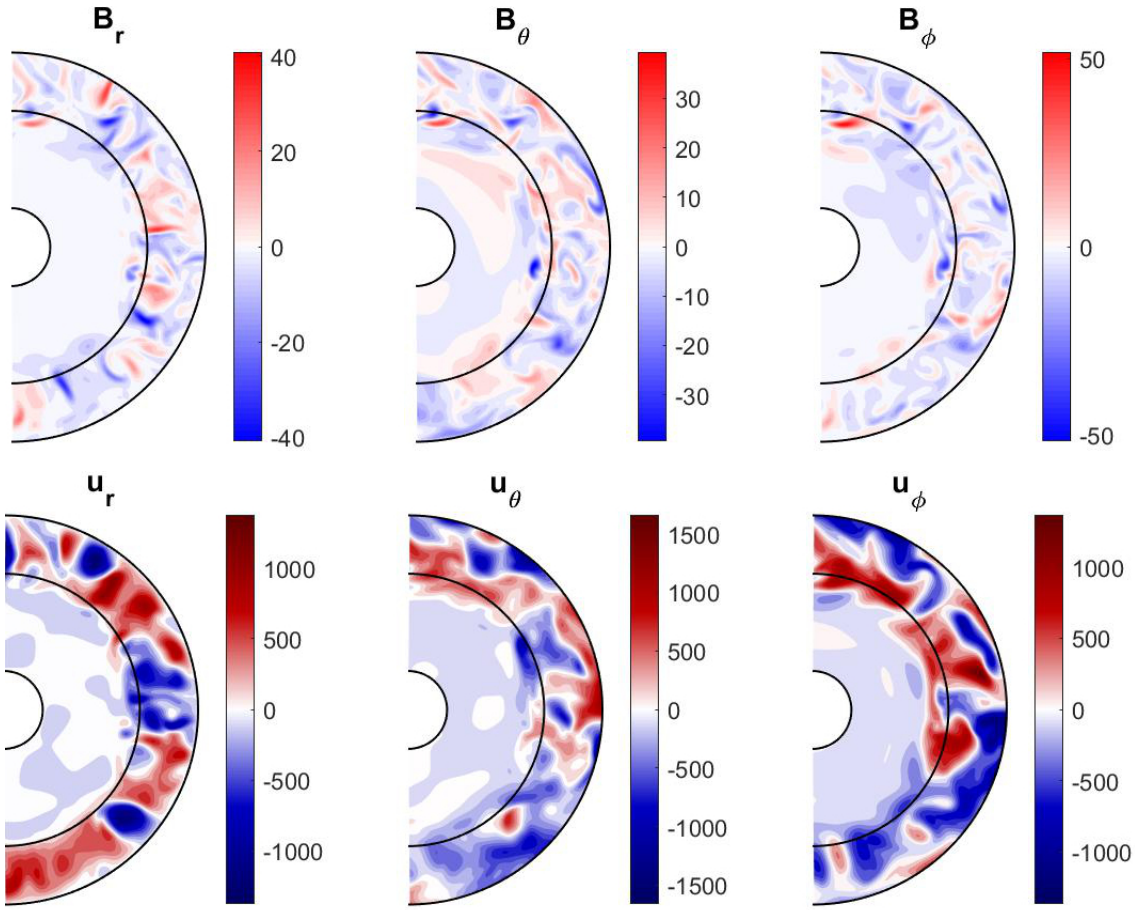

Figure 4.9: Snapshots of 3D meridional slice of the magnetic field and the velocity field at $t = 0.13$ for the $\mathrm{Ra}_o = 10^7$ case.

To demonstrate more quantitatively that these simulations are dynamos, in Figure 4.10, we show the total magnetic energy per unit volume E_M against time t for the run with $\mathrm{P}_m = 1$ and $\mathrm{Ra}_o = 10^7$ as well as the more turbulent case of $\mathrm{Ra}_o = 10^8$ and the more laminar non-dynamo case for $\mathrm{Ra}_o = 10^6$. We notice that E_M grows exponentially in the two dynamo cases, although with some significant fluctuations. When $\mathrm{Ra}_o = 10^7$, the average growth rate is $\lambda \approx 26$ leading to a corresponding growth timescale for the magnetic field equal to approximately $2/26 \approx 0.077$. We can compare that growth timescale to the typical convective turnover timescale for this simulation which is approximately equal to $L/u_{rms} \approx$

$0.3/500 = 0.0006$, where L is a typical eddy-scale size and $u_{rms} \sim \sqrt{E_K}$ (where $E_K = (1/(2V)) \int_V (u_r^2 + u_\theta^2 + u_\phi^2) dV$ is the total kinetic energy per unit volume V). We see that the convective turnover timescale is two orders of magnitude faster than the dynamo growth timescale, suggesting that the dynamo field in this run might be a marginal dynamo. Indeed, one might expect that the growth rate of the field in a standard kinematic dynamo should be comparable to the convective turnover frequency. For the higher $\mathrm{Ra}_o = 10^8$ case, using the same methodology, we find that the magnetic field growth timescale is 0.0048 while the convective turnover timescale is equal to 0.0002.

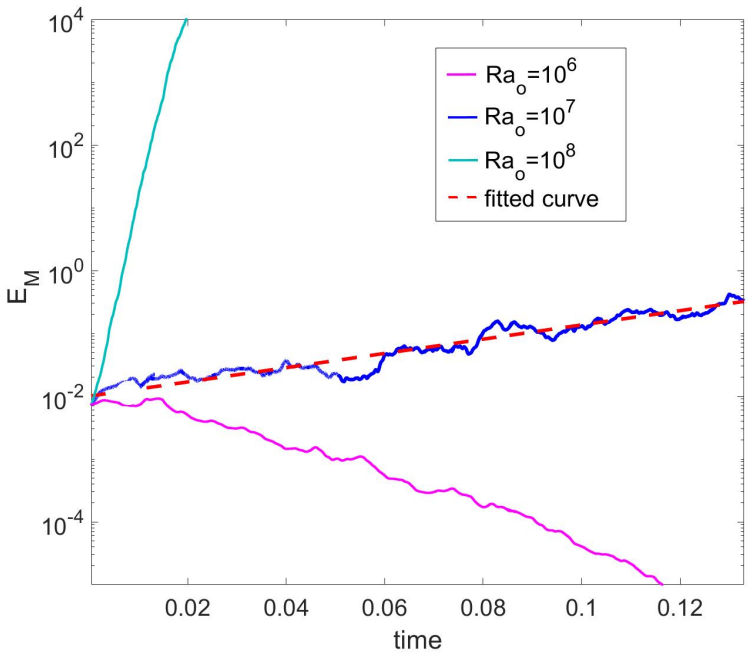

Figure 4.10: Total magnetic energy versus time for $\mathrm{P}_m = 1$, and $\mathrm{Ra}_o = 10^6$ (non-dynamo), $\mathrm{Ra}_o = 10^7$(dynamo), and $\mathrm{Ra}_o = 10^8$(dynamo) along with the fitted exponential curve for the case of $\mathrm{Ra}_o = 10^7$.

Both of these dynamos are essentially kinematic dynamos for the duration of the existing simulation since the nonlinear Lorentz force is very small ($Q = 0.01$), therefore the total magnetic energy remains much smaller than the total kinetic

energy. This can be confirmed in Figure 4.11 which shows radial profiles of the spherically averaged magnetic and kinetic energies at $t \approx 0.13$ (for $\mathrm{Ra}_o = 10^7$) and $t \approx 0.02$ (for $\mathrm{Ra}_o = 10^8$). A further confirmation that the flow has not been affected by the magnetic field yet is that the kinetic energy of the equivalent purely hydrodynamic simulation coincides more or less with $\bar{E}_K$ of the respective MHD case. The fact that the magnetic energy remains small is a result of the choice of our initial field which is very weak ($Q = 0.01$) combined with the limited amount of time for which the simulations were integrated. We expect that the magnetic energies will ultimately saturate to a statistically steady state, when some fraction of equipartition is achieved i.e. when the Lorentz force becomes comparable to the inertial forces in our system. This should happen when $B_{rms}^2/(8\pi) \sim \rho u_{rms}^2/2 \Rightarrow B_{rms} \sim \sqrt{4\pi\rho} u_{rms}$, in dimensional units or non-dimensionally when $E_M \sim E_K \Rightarrow B^2 \sim 2E_K/Q$. We notice that the magnetic energy is much closer to the kinetic energy for the higher Ra_o case than for the low Ra_o case despite being taken at a much earlier time, and is not far from reaching equipartition.

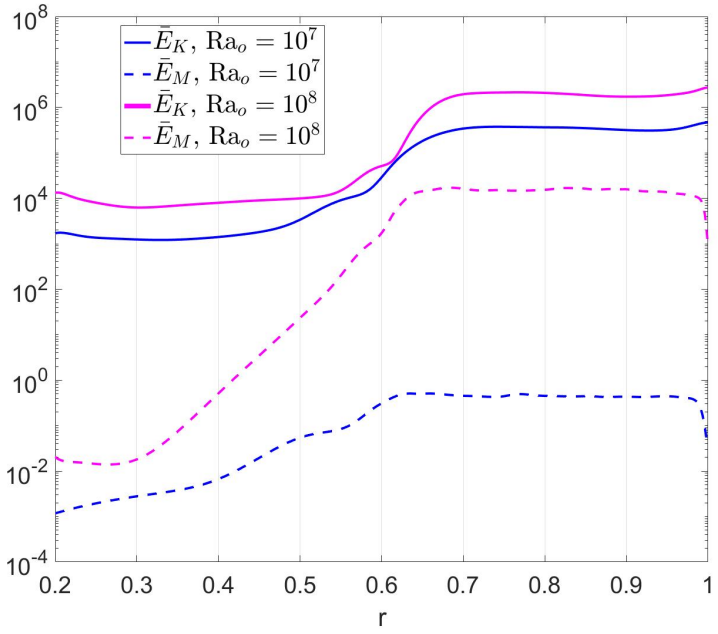

Figure 4.11: Plot of $\bar{E}_M(r)$ and $\bar{E}_K(r)$ against r for Ra$_o = 10^7$ at $t \approx 0.13$ and for Ra$_o = 10^8$ at $t \approx 0.02$.

Focusing again in Fig. 4.11 and more specifically at the spatial dependence of $\bar{E}_M(r)$, we see that the magnetic energy is almost constant in the CZ down to $r \sim 0.6$. This shows that the small-scale dynamo is generated within the CZ as well as in the overshoot region by turbulent motions. Below a certain radius, which is at $r \approx 0.62$ for the Ra$_o = 10^7$ case and at $r \approx 0.64$ for the Ra$_o = 10^8$ case, the magnetic energy starts decreasing exponentially inwards. This transition happens within the overshoot region, which was defined in Chapter 3 as the region where the kinetic energy has a Gaussian profile. In fact, we find that the distance of this point to the bottom of the CZ is a fraction of δ_u, i.e. of the lengthscale related to the stopping distance of the strongest of the downflows in the RZ (see Chapter 3). This is quite intuitive, since the dynamo is generated and resides in the regions where the turbulent motions are the strongest. However, as they approach the lower part of the overshoot region, the convective motions become

much weaker, and the dynamo can no longer operate so the field has to decay.

By fitting an exponential to $\bar{E}_M(r)$ below $r = 0.6$ we find that the exponential decay rate is equal to 20 for the case of $\mathrm{Ra}_o = 10^7$ and to 50 for the $\mathrm{Ra}_o = 10^8$ case. This results in a typical decay lengthscale of approximately $2/20 = 0.1$ for the $\mathrm{Ra}_o = 10^7$ case and $2/50 = 0.04$ for the $\mathrm{Ra}_o = 10^8$ case. Looking at the time-averaged magnetic energy spectra profiles in Fig. 4.12 and Fig. 4.13, we see that it peaks at $l = 9$ for the $\mathrm{Ra}_o = 10^7$ run and at $l = 21$ for the more turbulent case of $\mathrm{Ra}_o = 10^8$, corresponding to characteristic lengthscales of $1/9 \approx 0.11$ for the $\mathrm{Ra}_o = 10^7$ run and $1/21 \approx 0.048$ for the $\mathrm{Ra}_o = 10^8$ run. The fact that the radial decay lengthscale of the field in the RZ is approximately equal to the latitudinal lengthscale of the field in the CZ is of course not a coincidence, and comes from the fact that the field in the RZ, to a first approximation, satisfies $\nabla^2 B = 0$.

Furthermore, comparing the kinetic energy spectra $E_K(l)$ to the magnetic energy spectra $E_M(l)$, we see that for both $\mathrm{Ra}_o = 10^7$ and $\mathrm{Ra}_o = 10^8$, the peak of $E_M(l)$ is at higher wavenumbers ($l = 9$, and $l = 21$, respectively) than for $E_K(l)$ (where the maximum is at $l = 4$). Therefore, we verify what we saw in the snapshots of Fig. 4.8, namely that the characteristic lengthscale of the magnetic field is not only substantially smaller than that of the dominant turbulent eddies, but also that it decreases with increasing Ra_o. This shows that the system is indeed what is often known as a "small-scale" dynamo, where field is generated on the velocity scales and smaller. Most sufficiently turbulent flows are likely to be small-scale dynamos with the incorporation of seed magnetic fields. Note that "large-scale" dynamos, where magnetic field is generated at scales larger than the natural velocity scale, are much harder to achieve. We suspect (without being able to prove it) that the emergent scale of the dynamo field in these simulations is the smallest possible scale for which the flow is still locally a dynamo (i.e

where the inductive stretching rate overcomes the diffusion rate). Indeed, since the eddy turnover time in a turbulent cascade decreases with decreasing scale (at least for a purely hydrodynamic Kolmogorov spectrum), magnetic fields will grow more rapidly on the small scales than the large scales, until diffusion becomes important.

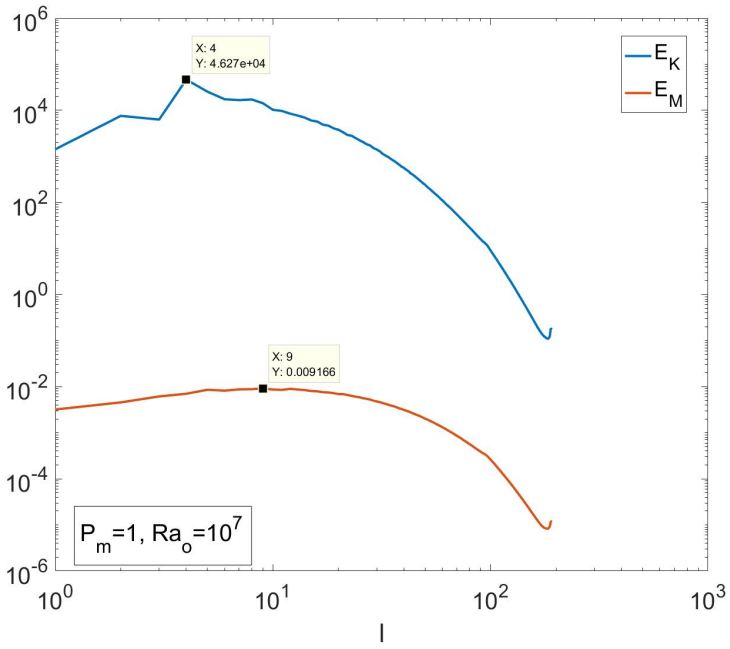

Figure 4.12: Energy spectra versus l for $\mathrm{Ra}_o = 10^7$.

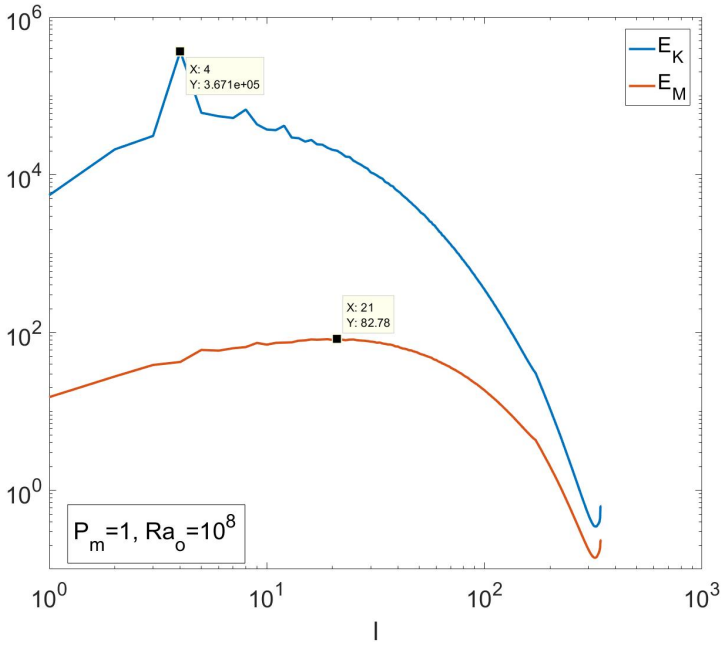

Figure 4.13: Energy spectra versus l for $\mathrm{Ra}_o = 10^8$.

In the previous section, we did not find any evidence that overshooting plumes would halt the diffusion of the magnetic field, and that on the contrary, the turbulent diffusivity of the convection zone promotes the decay of the original dipole field. It is therefore worth investigating whether the presence of a dynamo in the CZ changes this general picture of the evolution of the original dipole.

In Fig. 4.14, we show the temporal evolution of E_M along with the volume average of the energy in the dipole E_{dip} in the simulation plus the evolution of the purely diffusive solution for the run of $\mathrm{Ra}_o = 10^7$. We notice that although the total magnetic energy grows exponentially, E_{dip} initially decreases faster than the purely diffusive case, which is consistent with what we found in the non-dynamo simulations. However, at $t \approx 0.05$, E_{dip} starts increasing exponentially with the same growth rate as the total magnetic energy. This result is surprising at first since this naively looks like evidence for a large-scale dynamo, which, according

to mean field theory, is not to be expected since there is no rotation to provide the broken symmetry required for an $\alpha-$ effect. However, we interpret this to be the result of nonlinear interactions between small-scale modes which drive a weak but non-zero transfer of energy to the largest-scale mode. This would explain why the dipole mode, even though it has a much lower amplitude, still grows at the same rate as the small-scale modes.

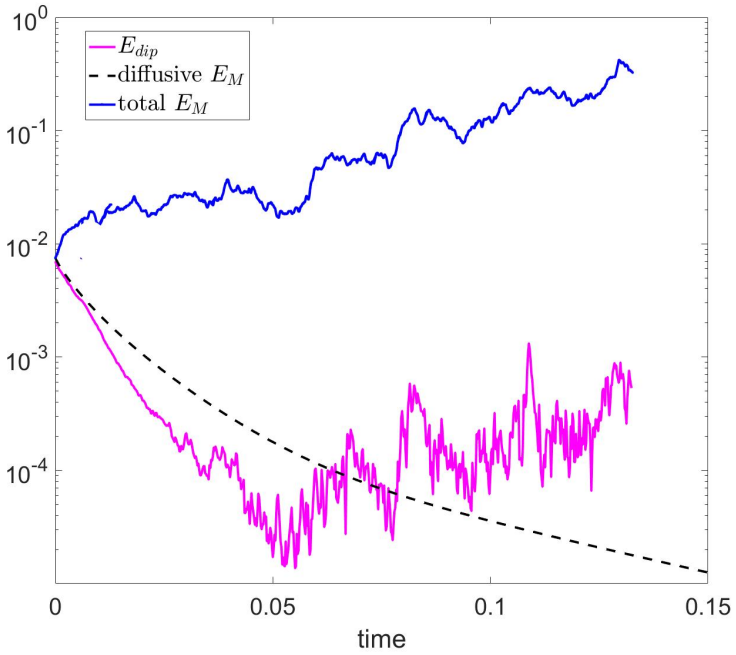

Figure 4.14: Plot of E_M, along with E_{dip} and the magnetic energy in the purely diffusive case versus time for $\mathrm{Ra}_o = 10^7$.

This behavior can also be seen in Fig. 4.15, where we plot $\bar{E}_M(r)$ (solid lines), along with $\bar{E}_{dip}(r)$ (dashed lines) and the purely diffusive one (dotted lines) now against r for an initial time $t \approx 0.001$ up to a later time $t \approx 0.13$. We observe a transition between the centrally-dominated original dipole that gradually diffuses away to a surface-dominated dynamo-driven weak dipole.

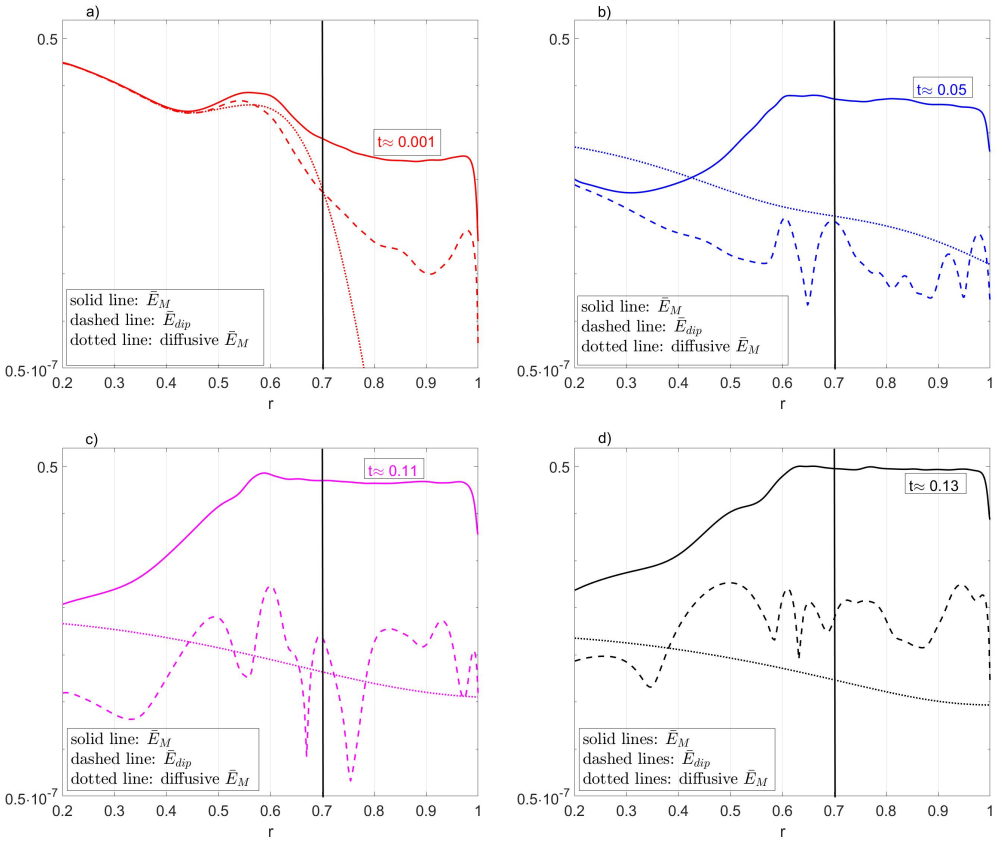

Figure 4.15: Total magnetic energy $\bar{E}_M(r)$ (solid lines) along with the magnetic energy in the dipole $\bar{E}_{dip}(r)$ (dashed lines), and the magnetic energy of the purely diffusive case (dotted lines) at four representative times a) $t \approx 0.001$ (red), b) $t \approx 0.05$ (blue), c) $t \approx 0.11$ (purple) and d) $t \approx 0.13$ (black) for $\mathrm{Ra}_o = 10^7$.

The same trend follows for the more turbulent case of $\mathrm{Ra}_o = 10^8$ shown in Figure 4.16. There, the small-scale dynamo field is stronger than the less turbulent $\mathrm{Ra}_o = 10^7$ case, so E_M has a more rapid exponential growth in time. The dipole field is also amplified in this case at $t \approx 0.01$ which is much earlier than for the $\mathrm{Ra}_o = 10^7$ case, and it grows at the same rate as E_M.

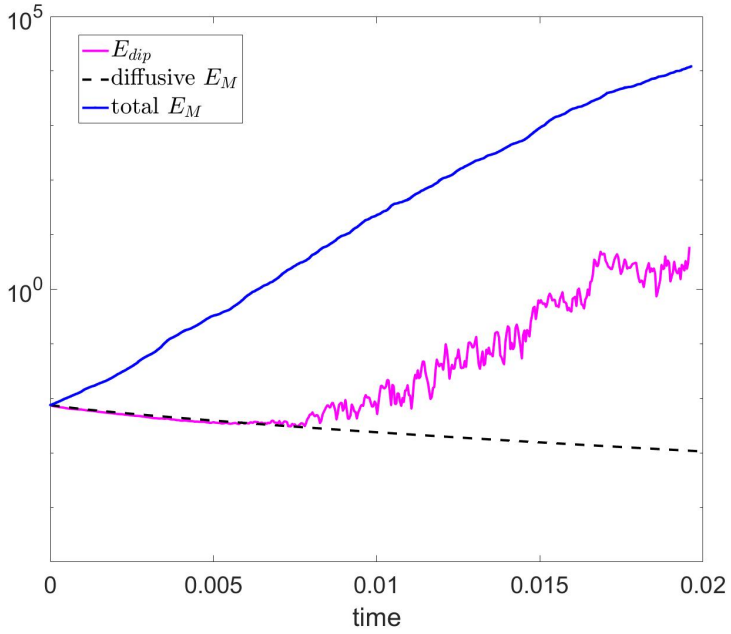

Figure 4.16: Plot of E_M, along with E_{dip} and the magnetic energy in the purely diffusive case versus time for $\mathrm{Ra}_o = 10^8$.

In these dynamo cases, the distribution of dipole energy is very different from the non-dynamo case. The initial dipole is lost, in much the same manner as before, but a CZ element remains, and is amplified, to create a very different profile. Ultimately however, there is certainly no confinement of the dipole energy to the RZ. Therefore, similarly to the results from the previous section, the dipole magnetic field does not remain confined in the RZ by the turbulent motions.

4.5 Summary and Discussion

In this chapter, we extended our study from Chapter 3 to include magnetic fields. Our model configuration was the same as in Chapter 3, where we had a convectively unstable region from $r = 0.7r_o$ to r_o and a stable one from $r = 0.2r_o$ up to $r = 0.7r_o$. We restarted one of our thermally equilibrated hydrodynamic

simulations from Chapter 3 and initialized it with a weak poloidal dipole magnetic field contained in the RZ. A main question that we wanted to address is whether the dipole field could stay confined in the RZ, as is required in certain theories of the solar interior. Much work has been done in the past on this problem, however the majority of studies incorporated rotation and focused on laminar processes to explain the confinement of the magnetic field (e.g. [25, 139, 55, 1]). In this work, we investigated the possibility of magnetic confinement solely by the magnetic field's interaction with the turbulent motions of the CZ and overshoot region in the absence of rotation. We examined two cases: one with a magnetic Prandtl number $\mathrm{P}_m = 0.1$ and one with $\mathrm{P}_m = 1$ for different values of Ra_o, at fixed $S = 5$, $d_{out} = 0.003$ and Pr= 0.1. Although the values of Ra_o and Pr used in our calculations are far from the solar ones (see below), the magnetic Prandtl numbers are not that different from the actual solar value which is approximately equal to $\mathrm{P}_m \sim 10^{-2}$ at the bottom of the CZ.

We found that the runs with $\mathrm{P}_m = 0.1$ did not exhibit significant dynamo action and the total magnetic energy decayed. The dipole field diffused outward where it interacted with the turbulent motions in the CZ. That resulted in a transient amplification of the magnetic energy which was dominated by the non-dipole modes. However, the diffusion of the field was much faster than the input rate of energy in the CZ and the resultant energy amplification, leading to the exponential decay of the energy in the system. Interestingly, we found that the dipole energy diffused much faster than the energy in the purely diffusive case due to the enhanced turbulent diffusion from its interaction with the turbulent motions. These non-dynamo cases showed that the dipole field cannot stay confined in the RZ by the turbulent motions.

For the higher $\mathrm{P}_m = 1$ cases, we found that the convection zone (and part of the

overshoot region) operated as a small-scale essentially kinematic dynamo for the sufficiently turbulent cases of $\mathrm{Ra}_o = 10^7$, and $\mathrm{Ra}_o = 10^8$. The magnetic energy in both of these simulations is growing exponentially and has not reached a saturated state yet. We might expect that to happen when a fraction of equipartition is achieved. Such small-scale dynamos generate and sustain magnetic fields at scales which are equal to or smaller than that of the energy-carrying eddies. Indeed, we found that the characteristic lengthscale of the dynamo field in the CZ was significantly smaller than that of the turbulent eddies, and that it also decreases with increasing Ra_o. Moreover, in Figure 4.11, we observed that $E_M(r)$ was somewhat constant down to $r \approx 0.6$ and after that point it decayed exponentially. We discussed that this is due to the fact that the small-scale field is generated in the CZ and the overshoot region where the turbulent motions are strong. However, it is also possible that most of the small-scale dynamo was generated in the CZ and only in a very small part of the overshoot region where the turbulent motions are still quite significant. Then, the small-scale field seen down to point $r \approx 0.6$ might have just been advected there from the upper part of the overshoot region by the turbulent overshoot motions. This needs further investigation in order to obtain more conclusive results.

In any case, there is small-scale dynamo field within the overshoot region. If we assume that the solar overshoot depth is a tiny fraction of a pressure scale-height as predicted in Chapter 3, then the solar dynamo should stop more or less at the base of the CZ. However, the field extends further down due to diffusion as seen by the exponential tail in the magnetic energy below $r \approx 0.6$. In future work, we will attempt to identify what effect this would have on the solar dynamics by also predicting the lengthscale associated with this exponential decay, in order to gain a better understanding of the implications of these processes in the solar interior.

While the two systems found for these two different P_m when considered in their entirety can clearly be defined as dynamos or non-dynamos, it is interesting to also consider them in the context of stoked dynamos, as raised in Byingtonet al. (2014) [27], since that framework was designed to address this issue. In that context, considering the CZ alone, it is "stoked" in the sense that magnetic field is gradually added to the originally field-free turbulent system. The CZ in the case of $P_m = 0.1$ could then be considered as a "stoked non-dynamo", since even with the magnetic energy input, it does not succeed to maintain magnetic energy. The CZ in the $P_m = 1$, $Ra_o \geq 10^7$ case however are "stoked dynamos", since they maintain (indeed, amplify) magnetic energy at least for the duration simulated.

Finally, we did not observe any magnetic pumping in either the non-dynamo or the dynamo simulations the way it was described in the 3D local MHD Cartesian simulations of Tobias et al. [143, 144]. Indeed, Tobias et al. (2001) [144] for instance, ran simulations of penetrative convection with an initial horizontal field located either in the CZ or the RZ and they found that the turbulent motions could pump the field down and store it in the stable region. More importantly, they observed two distinct phases in their simulations: the pumping phase, in which most of the magnetic flux was driven out of the unstable region and down to the stable one, and the diffusive phase, where the magnetic field diffused in the RZ. In our simulations, the dipole field had a diffusive behavior everywhere across the shell for the non-dynamo cases while it was amplified in the CZ and the overshoot region for the dynamo cases. It is possible that our global simulations were not turbulent enough nor asymmetric enough for efficient pumping. Our simulations are only at moderate Ra_o due to their numerical expense and Boussinesq, therefore, the only asymmetry in our system came from the sphericity of our shell and the boundary conditions, which might not be sufficient for the pumping

mechanism to succeed. In future work, it might be interesting to confirm this idea by examining the transport of a magnetic layer from within the CZ (much as [144]), and looking at the effects of enhanced asymmetry.

Case	P_m	Ra_o	N_r	N_θ	N_ϕ	Dynamo
1	0.1	10^7	400	288	320	$\times$
2	0.1	10^8	585	516	640	$\times$
3	0.1	10^9	585	516	640	$\times$
4	1	10^6	300	192	192	$\times$
5	1	10^7	400	288	320	$\surd$
6	1	10^8	585	516	640	$\surd$

Table 4.1: Table with all the different input parameters for $S = 5$, $d_{out} = 0.003$, and Pr= 0.1.

Chapter 5

Conclusion

This doctoral thesis is motivated by the dynamics associated with the convective-radiative interface region of the Sun and solar-type stars. These dynamics are known to play a fundamental role in processes such as transport of chemical species and magnetic fields, and yet they are still poorly understood. In this work, in order to shed some new light on this complicated topic, we studied convective processes by considering stellar-like conditions such as a non-zero adiabatic temperature gradient, fixed flux inner boundary condition, and a spherical shell geometry.

In Chapter 2, we initially focused on weakly non-Boussinesq convection. We presented the results of 3D simulations, for three different model setups, which all shared the same salient characteristics. A subadiabatic layer emerged in the convective region for sufficiently turbulent flows, a phenomenon which was enhanced for a larger superadiabaticty contrast across the shell. However, convection remained vigorous everywhere, thus indicating that it is a highly non-local process. We found that the subadiabatic layer appeared as a result of the asymmetry stemming from both the sphericity and the boundary conditions for the temperature. We have to note however, that the spherical convective shell modeled had a fixed

aspect ratio and we used a fixed Prandtl number in all of our runs. Therefore a wider range of parameters for different Prandlt numbers and shell thicknesses should be considered in future work to test under which conditions the subadiabatic layer can still appear. By increasing the thickness of the shell for instance, the superadiabaticity contrast becomes larger, hence a layer could emerge for lower values of Ra_o and also have different characteristics. Moreover, since we have stellar objects in mind, it is important to add rotational effects to the problem and study if the same dynamics will persist. It is possible that rotation will hinder the emergence of the subadiabatic layer, especially for rapidly rotating systems.

In Chapter 3, we extended the problem studied in Chapter 2 to include a stable region below the convection zone and we focused on the dynamics of overshooting/penetrative convection for a wide range of parameters. The setup in this case was different since we accounted for a heat source located close to the CZ-RZ interface so that we can have a superadiabaticity profile which would be almost constant within each region and varying across a thin transition region between the two. We showed that the overshooting motions depended on three parameters: the relative stability of the RZ, the transition width between the CZ and the RZ and the Rayleigh number. We also found that the kinetic energy profile below the bottom of the CZ can be modeled by a Gaussian profile for which we presented a model that accounts for both the Gaussian amplitude and its width which we estimated by a simple energetic argument. The overshooting motions managed to change the thermal stratification in the overshoot region however this effect was not so strong as to actually lead to an adiabatic fully thermally mixed region there. It would be very useful to study this problem for higher Rayleigh numbers and/or lower Prandtl numbers, since the values used in this chapter are far from the actual stellar ones. That would certainly give better estimates regarding the

overshoot depth in the Sun and solar-type stars, and it could potentially answer the long-standing question of whether there is actual penetration in real stars. Finally, a next step towards a better understanding of stellar overshooting processes is to add rotation and study how this affects the dynamics. This has been studied in detail in the 3D Cartesian compressible simulations of Brummell et al. (2002) [21] who found that rotation leads to smaller overshooting depths which also depend on the different latitudes. Thus, rotating overshooting convection in global simulations of spherical geometries should be investigated for a wide range of parameters, as well.

In Chapter 4, we added an initially contained dipole poloidal field in the stable region and we focused on its interaction with the turbulent motions. The main question we wanted to address was whether the field could be confined in the RZ by these motions as previously suggested by the work from e.g. Tobias et al. (2001) and Garaud & Rogers (2007) [144, 56]. Our numerical results were categorized into non-dynamo and dynamo cases. In the non-dynamo cases, we found that the field diffused outward and its field lines opened up and penetrated in the CZ leading to an unconfined configuration. Hence, the field could not remain confined in the RZ by the turbulent motions and in fact the energy in the dipole decreased much faster than the purely diffusive one due to the enhanced turbulent diffusivity by the convective motions. A next step towards a better understanding of the possible field confinement by the turbulent motions is to test whether there is any clear evidence of magnetic pumping, by adding a magnetic layer within the CZ this time (as for instance done by Tobias et al. (2001) [144]). Then, we could study if magnetic pumping is possible at the same Rayleigh numbers used here, or even use higher Ra_o values for which pumping would be more efficient. We note that we considered a Boussinesq spherical shell where any asymmetry is a result

of the sphericity and the thermal boundary conditions, but these might not be sufficient for the pumping mechanism to work. A possible avenue is to test the same problem using an anelastic or even fully compressible formulation that will definitely provide more asymmetry to the existing setup. Furthermore, we can look at this problem from a different angle, by adding rotation and investigating if the meridional flows generated in the CZ by differential rotation can help in the confinement of the dipole field as envisaged by GM98 ([67]). This has been previously studied in 3D spherical shells (e.g. [25, 139]), however the simulations were performed in the wrong parameter regime. We intend to study this problem by ensuring that we are in the right parameter regime where viscous forces are negligible.

We also observed that for the higher $\mathrm{P}_m = 1$ case and for sufficiently turbulent flows, the CZ and part of the overshoot region operated as a small-scale dynamo. At some point in the RZ, the turbulent motions were not strong enough to sustain the dynamo and its energy decayed exponentially. It would be quite interesting to be able to estimate what would happen in the Sun by predicting how far down in the overshoot region, the solar small-scale dynamo field could be generated. If the small-scale field was found to exist within the tachocline zone, that would have severe implications on the GM98 model which assumes a magnetic-free tachocline. Moreover, we found that the nonlinear interactions of the small-scale modes lead to a transfer of energy to the large-scale mode, such that the dipole energy is growing exponentially at the same rate as the total magnetic energy. Then, if there is a substantially strong dipole field in the solar RZ, it would possibly interact with the primordial field in a way that the magnetic field lines from the interior would connect to the CZ and the differential rotation would propagate in the RZ. Thus, in order for the GM98 model to work, the primordial field should remain entirely

confined in the RZ, and any dynamo field should be above the tachocline region, to ensure that the tachocline is indeed field-free. In future work, we intend to investigate these ideas even further.

Finally, in this chapter, we only accounted for a weak magnetic field with $Q = 0.01$, since we initially wanted to understand the effect of the turbulent motions on the field. In future work, we aim to study the effect of the magnetic field on the overshooting motions as well, by running numerical experiments with larger values of $Q >> 1$ that correspond to stronger initial fields.

Chapter 6

Appendix

Calculation of the diffusive solution of the dipolar poloidal magnetic field

Here, we provide the analytic solution of the induction equation under the assumption that there is no fluid motion. Therefore, we focus on the diffusion equation for the poloidal axisymmetric magnetic field $\mathbf{B} = \boldsymbol{B}_p$ given by:

$$\frac{\partial \boldsymbol{B}_p}{\partial t} = \nabla \times (\eta \nabla \times \boldsymbol{B}_p), \tag{6.1}$$

noting that η could be a function of r. The solution follows the work of Garaud (1999) [53], up to a point. We can express $\boldsymbol{B}_p$ in terms of the potential $P(r, \theta, t)$ (e.g. as in [30]) such that

$$\boldsymbol{B}_p = \nabla \times (r \sin\theta P \hat{\mathbf{e}}_\phi). \tag{6.2}$$

By substituting Eq. (6.2) into Eq. (6.1), we get

$$\frac{\partial^2 P}{\partial r^2} + \frac{4}{r}\frac{\partial P}{\partial r} + \frac{(1-\mu^2)}{r^2}\frac{\partial^2 P}{\partial \mu^2} - \frac{4\mu}{r^2}\frac{\partial P}{\partial \mu} = \frac{1}{\eta}\frac{\partial P}{\partial t}, \tag{6.3}$$

where $\mu = \cos\theta$. Then, we can write $P(r, \mu, t) = R(r, t)G(\mu)$ so the components of the magnetic field $\boldsymbol{B}_p = (B_r, B_\theta)$ can be expressed in terms of R and G such that:

$$B_r = -R(r,t)\frac{\partial}{\partial \mu}((1-\mu^2)G(\mu)), \tag{6.4}$$

and

$$B_\theta = -G(\mu)\sqrt{1-\mu^2}\frac{1}{r}\frac{\partial}{\partial r}(r^2 R(r,t)). \tag{6.5}$$

Now, we can rewrite Eq. (6.3) by separating it into equations for $R(r, t)$ and $G(\mu)$:

$$\frac{\partial^2 R}{\partial r^2} + \frac{4}{r}\frac{\partial R}{\partial r} - \frac{1}{\eta}\frac{\partial R}{\partial t} = \frac{\lambda^2}{r^2}R, \tag{6.6}$$

and

$$(1-\mu^2)\frac{\partial^2 G}{\partial \mu^2} - 4\mu\frac{\partial G}{\partial \mu} = -\lambda^2 G. \tag{6.7}$$

Equation (6.7) is the eigenvalue equation of the Gegenbauer polynomial $G_k^\alpha(\mu)$, with eigenvalues given by $\lambda^2 = k(k + 2\alpha)$. Here, $\alpha = 3/2$, so the solution of Eq. (6.7) is $G_k^{3/2}(\mu)$.

Hence, the full solution is given by (see [53]):

$$P(r, \mu, t) = \sum_{k=0}^{\infty} A_k R_k(r, t) G_k^{3/2}(\mu). \tag{6.8}$$

Since we have a dipole configuration and from Eq. (6.5), it follows that the only coefficient A_k that is non-zero is for $k = 0$. The corresponding polynomial is simply $G_0^{3/2}(\mu) = 1$, with $\lambda_0 = 0$. Thus, the problem is now simplified and we

only need to solve the equation for $R(r,t)$ (Eq. (6.6)):

$$\frac{\partial^2 R}{\partial r^2} + \frac{4}{r}\frac{\partial R}{\partial r} - \frac{1}{\eta}\frac{\partial R}{\partial t} = 0. \tag{6.9}$$

The boundary conditions require that R and $\partial R/\partial r$ are continuous at $r = 1$, and that there is no singularity at the origin $r = 0$, i.e. $R(0,t)$ =finite.

The solution for $P(r,\theta,t)$ is then given by:

$$P(r,\theta,t) = \sum_{n=1}^{\infty} A_n r^{-3/2} J_{3/2}(n\pi r)\exp(-\eta n^2\pi^2 t), \tag{6.10}$$

where $J_{3/2}$ is the Bessel function of order 3/2, and where the coefficient A_n is given by:

$$A_n = \frac{\int_0^1 P(r,\theta,0) r^{-3/2} J_{3/2}(n\pi r) r^4 dr}{\int_0^1 (r^{-3/2} J_{3/2}(n\pi r))^2 r^4 dr}. \tag{6.11}$$

Then, the field components can be written in terms of P (see Eq. (6.10)):

$$B_r = 2\cos\theta P + \sin\theta\frac{\partial P}{\partial\theta}, \quad B_\theta = -2\sin\theta P - r\sin\theta\frac{\partial P}{\partial r}. \tag{6.12}$$

Bibliography

[1] L. A. Acevedo-Arreguin, P. Garaud, and T. S. Wood. Dynamics of the solar tachocline - III. Numerical solutions of the Gough and McIntyre model. *Monthly Notices of the Royal Astronomical Society*, 434:720–741, September 2013.

[2] G. Ahlers, S. Grossmann, and D. Lohse. Heat transfer and large scale dynamics in turbulent Rayleigh-Bénard convection. *Reviews of Modern Physics*, 81:503–537, April 2009.

[3] B. Ahrens, M. Stix, and M. Thorn. On the depletion of lithium in the sun. *Astronomy and Astrophysics*, 264:673–678, October 1992.

[4] J. Aubert, J. Aurnou, and J. Wicht. The magnetic structure of convection-driven numerical dynamos. *Geophysical Journal International*, 172:945–956, March 2008.

[5] K. C. Augustson, B. P. Brown, A. S. Brun, M. S. Miesch, and J. Toomre. Convection and Differential Rotation in F-type Stars. *Astrophysical Journal*, 756:169, September 2012.

[6] J. Aurnou, M. Heimpel, and J. Wicht. The effects of vigorous mixing in a convective model of zonal flow on the ice giants. *Icarus*, 190:110–126, September 2007.

[7] I. Baraffe, J. Pratt, T. Goffrey, T. Constantino, D. Folini, M. V. Popov, R. Walder, and M. Viallet. Lithium Depletion in Solar-like Stars: Effect of Overshooting Based on Realistic Multi-dimensional Simulations. *Astrophysical Journal Letters*, 845:L6, August 2017.

[8] G. K. Batchelor. The conditions for dynamical similarity of motions of a frictionless perfect-gas atmosphere. *Quarterly Journal of the Royal Meteorological Society*, 79:224–235, April 1953.

[9] D. Bercovici, G. Schubert, and G. A. Glatzmaier. Three-dimensional spherical models of convection in the earth's mantle. *Science*, 244:950–955, May 1989.

[10] D. Bercovici, G. Schubert, G. A. Glatzmaier, and A. Zebib. Three-dimensional thermal convection in a spherical shell. *Journal of Fluid Mechanics*, 206:75–104, September 1989.

[11] E. Böhm-Vitense. Über die Wasserstoffkonvektionszone in Sternen verschiedener Effektivtemperaturen und Leuchtkräfte. Mit 5 Textabbildungen. *Z. Astrophys.*, 46:108, 1958.

[12] J. Boussinesq. *Theorie Analytique de la Chaleur*, volume 2. Gauthier Villars, Paris, 1903.

[13] J. Braithwaite. Axisymmetric magnetic fields in stars: relative strengths of poloidal and toroidal components. *Monthly Notices of the Royal Astronomical Society*, 397:763–774, August 2009.

[14] A. Brandenburg. Stellar Mixing Length Theory with Entropy Rain. *Astrophysical Journal*, 832:6, November 2016.

[15] D. Breuer, B. Futterer, A. Plesa, A. Krebs, F. Zaussinger, and C. Egbers. Sheet-like and plume-like thermal flow in a spherical convection experiment performed under microgravity. *AGU Fall Meeting Abstracts*, 2013.

[16] B. P. Brown, M. K. Browning, A. S. Brun, M. S. Miesch, and J. Toomre. Rapidly Rotating Suns and Active Nests of Convection. *Astrophysical Journal*, 689:1354–1372, December 2008.

[17] B. P. Brown, G. M. Vasil, and E. G. Zweibel. Energy Conservation and Gravity Waves in Sound-proof Treatments of Stellar Interiors. Part I. Anelastic Approximations. *Astrophysical Journal*, 756:109, September 2012.

[18] M. K. Browning, A. S. Brun, M. S. Miesch, and J. Toomre. Dynamo action in simulations of penetrative solar convection with an imposed tachocline. *Astronomische Nachrichten*, 328:1100, December 2007.

[19] M. K. Browning, A. S. Brun, and J. Toomre. Simulations of Core Convection in Rotating A-Type Stars: Differential Rotation and Overshooting. *Astrophysical Journal*, 601:512–529, January 2004.

[20] M. K. Browning, M. S. Miesch, A. S. Brun, and J. Toomre. Dynamo Action in the Solar Convection Zone and Tachocline: Pumping and Organization of Toroidal Fields. *Astrophysical Journal Letters*, 648:L157–L160, September 2006.

[21] N. H. Brummell, T. L. Clune, and J. Toomre. Penetration and Overshooting in Turbulent Compressible Convection. *Astrophysical Journal*, 570:825–854, May 2002.

[22] A. S. Brun, M. K. Browning, and J. Toomre. Simulations of Core Convection in Rotating A-Type Stars: Magnetic Dynamo Action. *Astrophysical Journal*, 629:461–481, August 2005.

[23] A. S. Brun, M. S. Miesch, and J. Toomre. Modeling the Dynamical Coupling of Solar Convection with the Radiative Interior. *Astrophysical Journal*, 742:79, December 2011.

[24] A. S. Brun, A. Strugarek, J. Varela, S. P. Matt, K. C. Augustson, C. Emeriau, O. L. DoCao, B. Brown, and J. Toomre. On Differential Rotation and Overshooting in Solar-like Stars. *Astrophysical Journal*, 836:192, February 2017.

[25] A. S. Brun and J.-P. Zahn. Magnetic confinement of the solar tachocline. *Astronomy and Astrophysics*, 457:665–674, October 2006.

[26] F. H. Busse. Patterns of convection in spherical shells. *Journal of Fluid Mechanics*, 72:67–85, November 1975.

[27] B. M. Byington, N. H. Brummell, J. M. Stone, and D. O. Gough. Stoked nondynamos: sustaining field in magnetically non-closed systems. *New Journal of Physics*, 16(8):083002, August 2014.

[28] F. Cattaneo, T. Emonet, and N. Weiss. On the Interaction between Convection and Magnetic Fields. *Astrophysical Journal*, 588:1183–1198, May 2003.

[29] K. L. Chan and D. Gigas. Downflows and entropy gradient reversal in deep convection. *Astrophys. J. Letters*, 389:L87–L90, April 1992.

[30] S. Chandrasekhar. Effect of Internal Motions on the Decay of a Magnetic Field in a Fluid Conductor. *Astrophysical Journal*, 124:244, July 1956.

[31] S. Chandrasekhar. *Hydrodynamic and Hydromagnetic Stability*. Oxford University Press, 1961.

[32] P. Charbonneau, J. Christensen-Dalsgaard, R. Henning, R. M. Larsen, J. Schou, M. J. Thompson, and S. Tomczyk. Helioseismic Constraints on the Structure of the Solar Tachocline. *Astrophysical Journal*, 527:445–460, December 1999.

[33] P. Charbonneau and K. B. MacGregor. Solar Interface Dynamos. II. Linear, Kinematic Models in Spherical Geometry. *Astrophysical Journal*, 486:502–520, September 1997.

[34] G. Choblet. On the scaling of heat transfer for mixed heating convection in a spherical shell. *Physics of the Earth and Planetary Interiors*, 206:31–42, September 2012.

[35] U. R. Christensen. Zonal flow driven by strongly supercritical convection in rotating spherical shells. *Journal of Fluid Mechanics*, 470:115–133, November 2002.

[36] J. Christensen-Dalsgaard, W. Dappen, S. V. Ajukov, E. R. Anderson, H. M. Antia, S. Basu, V. A. Baturin, G. Berthomieu, B. Chaboyer, S. M. Chitre, A. N. Cox, P. Demarque, J. Donatowicz, W. A. Dziembowski, M. Gabriel, D. O. Gough, D. B. Guenther, J. A. Guzik, J. W. Harvey, F. Hill, G. Houdek, C. A. Iglesias, A. G. Kosovichev, J. W. Leibacher, P. Morel, C. R. Proffitt, J. Provost, J. Reiter, E. J. Rhodes, Jr., F. J. Rogers, I. W. Roxburgh, M. J. Thompson, and R. K. Ulrich. The Current State of Solar Modeling. *Science*, 272:1286–1292, May 1996.

[37] J. Christensen-Dalsgaard, D. O. Gough, and E. Knudstrup. On the hydrostatic stratification of the solar tachocline. *Monthly Notices of the Royal Astronomical Society*, 477:3845–3852, July 2018.

[38] J. Christensen-Dalsgaard, D. O. Gough, and M. J. Thompson. The depth of the solar convection zone. *Astrophysical Journal*, 378:413–437, September 1991.

[39] J. Christensen-Dalsgaard, M. J. P. F. G. Monteiro, M. Rempel, and M. J. Thompson. A more realistic representation of overshoot at the base of the solar convective envelope as seen by helioseismology. *Monthly Notices of the Royal Astronomical Society*, 414:1158–1174, June 2011.

[40] B. C. Cogan. Convective Overshooting in Main-Sequence Models. *Astrophysical Journal*, 201:637–640, November 1975.

[41] L.-A. Couston, D. Lecoanet, B. Favier, and M. Le Bars. Dynamics of mixed convective-stably-stratified fluids. *Physical Review Fluids*, 2(9):094804, September 2017.

[42] J. P. Cox and R. T. Giuli. *Principles of stellar structure* . 1968.

[43] J. W. Deardorff. The Counter-Gradient Heat Flux in the Lower Atmosphere and in the Laboratory. *Journal of Atmospheric Sciences*, 23:503–506, September 1966.

[44] J. W. Deardorff, G. E. Willis, and D. K. Lilly. Laboratory investigation of non-steady penetrative convection. *Journal of Fluid Mechanics*, 35:7–31, 1969.

[45] S. Deheuvels, I. Brandão, V. Silva Aguirre, J. Ballot, E. Michel, M. S. Cunha, Y. Lebreton, and T. Appourchaux. Measuring the extent of convective cores in low-mass stars using Kepler data: toward a calibration of core overshooting. *Astronomy and Astrophysics*, 589:A93, May 2016.

[46] E. Dormy, P. Cardin, and D. Jault. MHD flow in a slightly differentially rotating spherical shell, with conducting inner core, in a dipolar magnetic field. *Earth and Planetary Science Letters*, 160:15–30, July 1998.

[47] E. Dormy, A. M. Soward, C. A. Jones, D. Jault, and P. Cardin. The onset of thermal convection in rotating spherical shells. *Journal of Fluid Mechanics*, 501:43–70, February 2004.

[48] Kerry A Emanuel. *Atmospheric convection*. Oxford University Press, 1994.

[49] V. C. A. Ferraro. The non-uniform rotation of the Sun and its magnetic field. *Monthly Notices of the Royal Astronomical Society*, 97:458, April 1937.

[50] F. Feudel, K. Bergemann, L. S. Tuckerman, C. Egbers, B. Futterer, M. Gellert, and R. Hollerbach. Convection patterns in a spherical fluid shell. *Physical Review E*, 83(4):046304, April 2011.

[51] E. Forgács-Dajka and K. Petrovay. Tachocline Confinement by an Oscillatory Magnetic Field. *Solar Physics*, 203:195–210, November 2001.

[52] B. Freytag, H.-G. Ludwig, and M. Steffen. Hydrodynamical models of stellar convection. The role of overshoot in DA white dwarfs, A-type stars, and the Sun. *Astronomy and Astrophysics*, 313:497–516, September 1996.

[53] P. Garaud. Propagation of a dynamo field in the radiative interior of the Sun. *Monthly Notices of the Royal Astronomical Society*, 304:583–588, April 1999.

[54] P. Garaud. Dynamics of the solar tachocline - I. An incompressible study. *Monthly Notices of the Royal Astronomical Society*, 329:1–17, January 2002.

[55] P. Garaud and J.-D. Garaud. Dynamics of the solar tachocline - II. The stratified case. *Monthly Notices of the Royal Astronomical Society*, 391:1239–1258, December 2008.

[56] P. Garaud and T. Rogers. Solar Rotation. In R. J. Stancliffe, G. Houdek, R. G. Martin, and C. A. Tout, editors, *Unsolved Problems in Stellar Physics: A Conference in Honor of Douglas Gough*, volume 948 of *American Institute of Physics Conference Series*, pages 237–248, November 2007.

[57] T. Gastine, J. Wicht, and J. Aubert. Scaling regimes in spherical shell rotating convection. *Journal of Fluid Mechanics*, 808:690–732, December 2016.

[58] T. Gastine, J. Wicht, and J. M. Aurnou. Turbulent Rayleigh-Bénard convection in spherical shells. *Journal of Fluid Mechanics*, 778:721–764, September 2015.

[59] M. Ghizaru, P. Charbonneau, and P. K. Smolarkiewicz. Magnetic Cycles in Global Large-eddy Simulations of Solar Convection. *Astrophysical Journal Letters*, 715:L133–L137, June 2010.

[60] P. A. Gilman. Theory of Convection in a Deep Rotating Spherical Shell, and its Application to the Sun. In V. Bumba and J. Kleczek, editors, *Basic Mechanisms of Solar Activity*, volume 71 of *IAU Symposium*, page 207, 1976.

[61] P. A. Gilman. Nonlinear Dynamics of Boussinesq Convection in a Deep Rotating Spherical Shell. I. *Geophysical and Astrophysical Fluid Dynamics*, 8:93–135, 1977.

[62] P. A. Gilman. Nonlinear Dynamics of Boussinesq Convection in a Deep Rotating Spherical Shell. II. Effects of Temperature Boundary Conditions. *Geophysical and Astrophysical Fluid Dynamics*, 11:157–179, 1978.

[63] P. A. Gilman and G. A. Glatzmaier. Compressible convection in a rotating spherical shell. I - Anelastic equations. II - A linear anelastic model. III - Analytic model for compressible vorticity waves. *Astrophysical Journal Supplement Series*, 45:335–388, February 1981.

[64] G. A. Glatzmaier and G. Schubert. Three-dimensional spherical models of layered and whole mantle convection. *Journal of Geophysical Research*, 98:21969–21976, December 1993.

[65] D. O. Gough. The Anelastic Approximation for Thermal Convection. *Journal of Atmospheric Sciences*, 26:448–456, May 1969.

[66] D. O. Gough, A. G. Kosovichev, J. Toomre, E. Anderson, H. M. Antia, S. Basu, B. Chaboyer, S. M. Chitre, J. Christensen-Dalsgaard, W. A. Dziembowski, A. Eff-Darwich, J. R. Elliott, P. M. Giles, P. R. Goode, J. A. Guzik, J. W. Harvey, F. Hill, J. W. Leibacher, M. J. P. F. G. Monteiro, O. Richard, T. Sekii, H. Shibahashi, M. Takata, M. J. Thompson, S. Vauclair, and S. V. Vorontsov. The Seismic Structure of the Sun. *Science*, 272:1296–1300, May 1996.

[67] D. O. Gough and M. E. McIntyre. Inevitability of a magnetic field in the Sun's radiative interior. *Nature*, 394:755–757, August 1998.

[68] D. O. Gough, E. A. Spiegel, and J. Toomre. Modal equations for cellular convection. *Journal of Fluid Mechanics*, 68:695–719, April 1975.

[69] S. Grossmann and D. Lohse. Scaling in thermal convection: a unifying theory. *Journal of Fluid Mechanics*, 407:27–56, March 2000.

[70] C. Guervilly, D. W. Hughes, and C. A. Jones. Large-scale vortices in rapidly rotating Rayleigh-Bénard convection. *Journal of Fluid Mechanics*, 758:407–435, November 2014.

[71] M. Heimpel and J. Aurnou. Turbulent convection in rapidly rotating spherical shells: A model for equatorial and high latitude jets on Jupiter and Saturn. *Icarus*, 187:540–557, April 2007.

[72] M. Heimpel, J. Aurnou, and J. Wicht. Simulation of equatorial and high-latitude jets on Jupiter in a deep convection model. *Nature*, 438:193–196, November 2005.

[73] J. R. Herring. Investigation of Problems in Thermal Convection. *Journal of Atmospheric Sciences*, 20:325–338, July 1963.

[74] F. Herwig. The evolution of AGB stars with convective overshoot. *Astronomy and Astrophysics*, 360:952–968, August 2000.

[75] F. Herwig, B. Freytag, R. M. Hueckstaedt, and F. X. Timmes. Hydrodynamic Simulations of He Shell Flash Convection. *Astrophysical Journal*, 642:1057–1074, May 2006.

[76] R. Howe, J. Christensen-Dalsgaard, F. Hill, R. W. Komm, R. M. Larsen, J. Schou, M. J. Thompson, and J. Toomre. Dynamic Variations at the Base of the Solar Convection Zone. *Science*, 287:2456–2460, March 2000.

[77] N. E. Hurlburt, J. Toomre, and J. M. Massaguer. Nonlinear compressible convection penetrating into stable layers and producing internal gravity waves. *Astrophysical Journal*, 311:563–577, December 1986.

[78] N. E. Hurlburt, J. Toomre, J. M. Massaguer, and J.-P. Zahn. Penetration below a convective zone. *Astrophysical Journal*, 421:245–260, January 1994.

[79] G. T. Jarvis, G. A. Glatzmaier, and V. I. Vangelov. Effects of curvature, aspect ratio and plan form in two- and three-dimensional spherical models of thermal convection. *Geophysical and Astrophysical Fluid Dynamics*, 79:147–171, 1995.

[80] H. Johnston and C. R. Doering. Comparison of Turbulent Thermal Convection between Conditions of Constant Temperature and Constant Flux. *Physical Review Letters*, 102(6):064501, February 2009.

[81] K. Julien, S. Legg, J. McWilliams, and J. Werne. Rapidly rotating turbulent Rayleigh-Benard convection. *Journal of Fluid Mechanics*, 322:243–273, 1996.

[82] P. J. Käpylä, M. Rheinhardt, A. Brandenburg, R. Arlt, M. J. Käpylä, A. Lagg, N. Olspert, and J. Warnecke. Extended Subadiabatic Layer in Simulations of Overshooting Convection. *Astrophysical Journal Letters*, 845:L23, August 2017.

[83] L. L. Kitchatinov and G. Rüdiger. Diamagnetic pumping near the base of a stellar convection zone. *Astronomische Nachrichten*, 329:372, May 2008.

[84] L. Korre, N. Brummell, and P. Garaud. Weakly non-Boussinesq convection in a gaseous spherical shell. *Physical Review E*, 96(3):033104, September 2017.

[85] J. Latour, E. A. Spiegel, J. Toomre, and J.-P. Zahn. Stellar convection theory. I - The anelastic modal equations. *Astrophysical Journal*, 207:233–243, July 1976.

[86] J. Latour, E. A. Spiegel, J. Toomre, and J.-P. Zahn. Stellar convection theory. I - The anelastic modal equations. *Astrophysical Journal*, 207:233–243, July 1976.

[87] J. Latour, J. Toomre, and J.-P. Zahn. Stellar convection theory. III - Dynamical coupling of the two convection zones in A-type stars by penetrative motions. *Astrophysical Journal*, 248:1081–1098, September 1981.

[88] Z. Liu, W. Yang, S. Bi, Z. Tian, K. Liu, Z. Ge, J. Yu, T. Li, X. Tan, X. He, Y. Wu, and P. Chintarungruangchai. Asteroseismic Analysis of the CoRoT Target HD 49933. *Astrophysical Journal*, 780:152, January 2014.

[89] K. B. MacGregor and P. Charbonneau. Angular Momentum Transport in Magnetized Stellar Radiative Zones. IV. Ferraro's Theorem and the Solar Tachocline. *Astrophysical Journal*, 519:911–917, July 1999.

[90] P. Machetel, M. Rabinowicz, and P. Bernardet. Three-dimensional convection in spherical shells. *Geophysical and Astrophysical Fluid Dynamics*, 37:57–84, 1986.

[91] A. Maeder. Stellar evolution. III - The overshooting from convective cores. *Astronomy and Astrophysics*, 40:303–310, May 1975.

[92] W. V. R. Malkus. *Aerodynamic Phenomena in Stellar Atmospheres, IAU Symp. 12, Bologna, Italy*, 1960.

[93] P. Markey and R. J. Tayler. The adiabatic stability of stars containing magnetic fields. II. Poloidal fields. *Monthly Notices of the Royal Astronomical Society*, 163:77–91, March 1973.

[94] J. Marshall and F. Schott. Open-ocean convection: Observations, theory, and models. *Reviews of Geophysics*, 37:1–64, February 1999.

[95] J. M. Massaguer, J. Latour, J. Toomre, and J.-P. Zahn. Penetrative cellular convection in a stratified atmosphere. *Astronomy and Astrophysics*, 140:1–16, November 1984.

[96] M. S. Miesch. Numerical Modeling of the Solar Tachocline. I. Freely Evolving Stratified Turbulence in a Thin Rotating Spherical Shell. *Astrophysical Journal*, 562:1058–1075, December 2001.

[97] M. S. Miesch. Large-Scale Dynamics of the Convection Zone and Tachocline. *Living Reviews in Solar Physics*, 2:1, December 2005.

[98] M. S. Miesch, A. S. Brun, and J. Toomre. Solar Differential Rotation Influenced by Latitudinal Entropy Variations in the Tachocline. *Astrophysical Journal*, 641:618–625, April 2006.

[99] M. Mocák, E. Müller, A. Weiss, and K. Kifonidis. The core helium flash revisited. II. Two and three-dimensional hydrodynamic simulations. *Astronomy & Astrophysics*, 501:659–677, July 2009.

[100] M. J. P. F. G. Monteiro, J. Christensen-Dalsgaard, and M. J. Thompson. Seismic study of overshoot at the base of the solar convective envelope. *Astronomy and Astrophysics*, 283:247–262, March 1994.

[101] M. J. P. F. G. Monteiro and M. J. Thompson. Looking for Variations with Latitude of the Base of the Solar Convection Zone. In S. Korzennik, editor, *Structure and Dynamics of the Interior of the Sun and Sun-like Stars*, volume 418 of *ESA Special Publication*, page 819, 1998.

[102] D. R. Moore and N. O. Weiss. Nonlinear penetrative convection. *Journal of Fluid Mechanics*, 61:553–581, 1973.

[103] B. R. Morton, G. Taylor, and J. S. Turner. Turbulent Gravitational Convection from Maintained and Instantaneous Sources. *Proceedings of the Royal Society of London Series A*, 234:1–23, January 1956.

[104] S. Musman. Penetrative convection. *Journal of Fluid Mechanics*, 31:343–360, 1968.

[105] H. J. Muthsam, W. Goeb, F. Kupka, W. Liebich, and J. Zoechling. A numerical study of compressible convection. *Astronomy and Astrophysics*, 293:127–141, January 1995.

[106] A. Oberbeck. Ueber die Wärmeleitung der Flüssigkeiten bei Berücksichtigung der Strömungen infolge von Temperaturdifferenzen. *Annalen der Physik*, 243:271–292, 1879.

[107] Y. Ogura and N. A. Phillips. Scale Analysis of Deep and Shallow Convection in the Atmosphere. *Journal of Atmospheric Sciences*, 19:173–179, March 1962.

[108] J. Otero, R. W. Wittenberg, R. A. Worthing, and C. R. Doering. Bounds on Rayleigh Bénard convection with an imposed heat flux. *Journal of Fluid Mechanics*, 473:191–199, December 2002.

[109] E. N. Parker. A solar dynamo surface wave at the interface between convection and nonuniform rotation. *Astrophysical Journal*, 408:707–719, May 1993.

[110] B. Paxton, L. Bildsten, A. Dotter, F. Herwig, P. Lesaffre, and F. Timmes. Modules for Experiments in Stellar Astrophysics (MESA). *Astrophysical Journal S*, 192:3, January 2011.

[111] B. Paxton, M. Cantiello, P. Arras, L. Bildsten, E. F. Brown, A. Dotter, C. Mankovich, M. H. Montgomery, D. Stello, F. X. Timmes, and R. Townsend. Modules for Experiments in Stellar Astrophysics (MESA): Planets, Oscillations, Rotation, and Massive Stars. *Astrophysical Journal S*, 208:4, September 2013.

[112] M. Pinsonneault. Mixing in Stars. *Annu. Rev. Astron. Astrophys*, 35:557–605, 1997.

[113] J. Pratt, I. Baraffe, T. Goffrey, T. Constantino, M. Viallet, M. V. Popov, R. Walder, and D. Folini. Extreme value statistics for two-dimensional convective penetration in a pre-main sequence star. *Astronomy and Astrophysics*, 604:A125, August 2017.

[114] É. Racine, P. Charbonneau, M. Ghizaru, A. Bouchat, and P. K. Smolarkiewicz. On the Mode of Dynamo Action in a Global Large-eddy Simulation of Solar Convection. *Astrophysical Journal*, 735:46, July 2011.

[115] M. Rempel. Overshoot at the Base of the Solar Convection Zone: A Semianalytical Approach. *Astrophysical Journal*, 607:1046–1064, June 2004.

[116] A. Renzini. Some embarrassments in current treatments of convective overshooting. *Astronomy and Astrophysics*, 188:49–54, December 1987.

[117] M. Rieutord and F. Rincon. The Sun's Supergranulation. *Living Reviews in Solar Physics*, 7:2, December 2010.

[118] P. H. Roberts. On Non-Linear BÉNARD Convection (with AN Appendix by K. Stewartson). In R. J. Donnelly, R. Herman, and I. Prigogine, editors, *Non-Equilibrium Thermodynamics, Variational Techniques, and Stability*, page 125, 1966.

[119] T. M. Rogers. On Limiting the Thickness of the Solar Tachocline. *Astrophysical Journal*, 733:12, May 2011.

[120] T. M. Rogers and G. A. Glatzmaier. Penetrative Convection within the Anelastic Approximation. *Astrophysical Journal*, 620:432–441, February 2005.

[121] T. M. Rogers, G. A. Glatzmaier, and C. A. Jones. Numerical Simulations of Penetration and Overshoot in the Sun. *Astrophysical Journal*, 653:765–773, December 2006.

[122] G. Rudiger and L. L. Kitchatinov. The slender solar tachocline: a magnetic model. *Astronomische Nachrichten*, 318:273, August 1997.

[123] E. Saikia, H. P. Singh, K. L. Chan, I. W. Roxburgh, and M. P. Srivastava. Examination of Scaling Relationships Involving Penetration Distance at the Bottom of a Stellar Convective Envelope. *Astrophysical Journal*, 529:402–413, January 2000.

[124] J. H. M. M. Schmitt, R. Rosner, and H. U. Bohn. The overshoot region at the bottom of the solar convection zone. *Astrophysical Journal*, 282:316–329, July 1984.

[125] G. Schubert. Numerical models of mantle convection. *Annual Review of Fluid Mechanics*, 24:359–394, 1992.

[126] G. Schubert and A. Zebib. Thermal convection of an internally heated infinite Prandtl number fluid in a spherical shell. *Geophysical and Astrophysical Fluid Dynamics*, 15:65–90, 1980.

[127] G. Shaviv and E. E. Salpeter. Convective Overshooting in Stellar Interior Models. *Astrophysical Journal*, 184:191–200, August 1973.

[128] B. I. Shraiman and E. D. Siggia. Heat transport in high-Rayleigh-number convection. *Physical Review A*, 42:3650–3653, September 1990.

[129] V. Silva Aguirre, J. Ballot, A. M. Serenelli, and A. Weiss. Constraining mixing processes in stellar cores using asteroseismology. Impact of semi-convection in low-mass stars. *Astronomy and Astrophysics*, 529:A63, May 2011.

[130] H. P. Singh, I. W. Roxburgh, and K. L. Chan. Three-dimensional simulation of penetrative convection: penetration below a convection zone. *Astronomy and Astrophysics*, 295:703, March 1995.

[131] H. P. Singh, I. W. Roxburgh, and K. L. Chan. A study of penetration at the bottom of a stellar convective envelope and its scaling relationships. *Astronomy and Astrophysics*, 340:178–182, December 1998.

[132] E. A. Spiegel. A Generalization of the Mixing-Length Theory of Turbulent Convection. *Astrophysical Journal*, 138:216, July 1963.

[133] E. A. Spiegel and G. Veronis. On the Boussinesq Approximation for a Compressible Fluid. *Astrophysical Journal*, 131:442, March 1960.

[134] E. A. Spiegel and J.-P. Zahn. The solar tachocline. *Astronomy and Astrophysics*, 265:106–114, November 1992.

[135] F. Spite and M. Spite. Abundance of lithium in unevolved halo stars and old disk stars - Interpretation and consequences. *Astronomy and Astrophysics*, 115:357–366, November 1982.

[136] H. C. Spruit. Differential rotation and magnetic fields in stellar interiors. *Astronomy and Astrophysics*, 349:189–202, September 1999.

[137] R. J. A. M. Stevens, D. Lohse, and R. Verzicco. Prandtl and Rayleigh number dependence of heat transport in high Rayleigh number thermal convection. *Journal of Fluid Mechanics*, 688:31–43, December 2011.

[138] J. M. Straus, J. B. Blake, and D. N. Schramm. Effects of convective overshoot on lithium depletion in main-sequence stars. *Astrophysical Journal*, 204:481–487, March 1976.

[139] A. Strugarek, A. S. Brun, and J.-P. Zahn. Magnetic confinement of the solar tachocline: II. Coupling to a convection zone. *Astronomy and Astrophysics*, 532:A34, August 2011.

[140] T. Sukhbold and S. E. Woosley. The Compactness of Presupernova Stellar Cores. *Astrophysical Journal*, 783:10, March 2014.

[141] A. Tilgner. High-Rayleigh-number convection in spherical shells. *Physical Review E*, 53:4847–4851, May 1996.

[142] S. Tobias and N. Weiss. The solar dynamo and the tachocline. In D. W. Hughes, R. Rosner, and N. O. Weiss, editors, *The Solar Tachocline*, page 319, 2007.

[143] S. M. Tobias, N. H. Brummell, T. L. Clune, and J. Toomre. Pumping of Magnetic Fields by Turbulent Penetrative Convection. *Astrophyscial Journal Letters*, 502:L177–L180, August 1998.

[144] S. M. Tobias, N. H. Brummell, T. L. Clune, and J. Toomre. Transport and Storage of Magnetic Field by Overshooting Turbulent Compressible Convection. *Astrophysical Journal*, 549:1183–1203, March 2001.

[145] J. Toomre, D. O. Gough, and E. A. Spiegel. Numerical solutions of single-mode convection equations. *Journal of Fluid Mechanics*, 79:1–31, January 1977.

[146] J. Toomre, D. O. Gough, and E. A. Spiegel. Time-dependent solutions of multimode convection equations. *Journal of Fluid Mechanics*, 125:99–122, December 1982.

[147] J. Toomre, J.-P. Zahn, J. Latour, and E. A. Spiegel. Stellar convection theory. II - Single-mode study of the second convection zone in an A-type star. *Astrophysical Journal*, 207:545–563, July 1976.

[148] A. A. Townsend. Natural convection in water over an ice surface. *Quarterly Journal of the Royal Meteorological Society*, 90:248–259, July 1964.

[149] A. A. van Ballegooijen. The overshoot layer at the base of the solar convective zone and the problem of magnetic flux storage. *Astronomy and Astrophysics*, 113:99–112, September 1982.

[150] V. I. Vangelov and G. T. Jarvis. Geometrical effects of curvature in axisymmetric spherical models of mantle convection. *Journal of Geophysical Research*, 99:9345–9358, May 1994.

[151] G. M. Vasil, D. Lecoanet, B. P. Brown, T. S. Wood, and E. G. Zweibel. Energy Conservation and Gravity Waves in Sound-proof Treatments of Stellar Interiors. II. Lagrangian Constrained Analysis. *Astrophysical Journal*, 773:169, August 2013.

[152] J. Verhoeven, T. Wiesehöfer, and S. Stellmach. Anelastic versus Fully Compressible Turbulent Rayleigh-Bénard Convection. *Astrophysical Journal*, 805:62, May 2015.

[153] G. Veronis. Penetrative Convection. *Astrophysical Journal*, 137:641, February 1963.

[154] G. Veronis. Large-amplitude Benard convection. *Journal of Fluid Mechanics*, 26:49–68, 1966.

[155] R. Verzicco and K. R. Sreenivasan. A comparison of turbulent thermal convection between conditions of constant temperature and constant heat flux. *Journal of Fluid Mechanics*, 595:203–219, 2008.

[156] N. O. Weiss. The Expulsion of Magnetic Flux by Eddies. *Proceedings of the Royal Society of London Series A*, 293:310–328, August 1966.

[157] T. S. Wood and N. H. Brummell. A Self-consistent Model of the Solar Tachocline. *Astrophysical Journal*, 853:97, February 2018.

[158] T. S. Wood and M. E. McIntyre. Polar confinement of the Sun's interior magnetic field by laminar magnetostrophic flow. *Journal of Fluid Mechanics*, 677:445–482, June 2011.

[159] G. A. E. Wright. Pinch instabilities in magnetic stars. *Monthly Notices of the Royal Astronomical Society*, 162:339–358, February 1973.

[160] J.-P. Zahn. Convective penetration in stellar interiors. *Astronomy and Astrophysics*, 252:179–188, December 1991.

[161] J.-P. Zahn, J. Toomre, and J. Latour. Nonlinear modal analysis of penetrative convection. *Geophysical and Astrophysical Fluid Dynamics*, 22:159–193, December 1982.

[162] A. Zebib, A. K. Goyal, and G. Schubert. Convective motions in a spherical shell. *Journal of Fluid Mechanics*, 152:39–48, 1985.

[163] A. Zebib, G. Schubert, and J. M. Straus. Infinite Prandtl number thermal convection in a spherical shell. *Journal of Fluid Mechanics*, 97:257–277, March 1980.